Charles University in Prague
Faculty of Mathematics and Physics

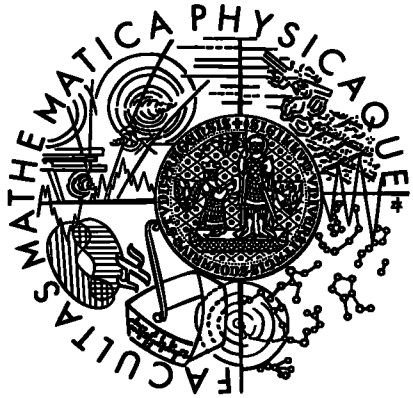

The study of instabilities in solar wind and in magnetosheath and their interaction with the Earth's magnetosphere

Doctoral thesis in branch F-2,
Physics of Plasma and Ionized Media

Kateřina Andréeová

Supervisor: Doc. RNDr. Lubomír Přech, Dr.
Department of Surface and Plasma Science

Prague 2008

Acknowledgments

I would like to thank to my supervisor Doc. RNDr. Lubomír Přech, Dr. for his help during the whole study and for his advices in programming and data processing. I would like to thanks, also to the Department of Surface and Plasma Science, namely Prof. RNDr. Jana Šafránková, DrSc. and Prof. RNDr. Zdeněk Němeček, DrSc.

Prague, July 2nd, 2008 Kateřina Andréeová

Contents

Chapter 1

Introduction

Solar activity and its modifications determine practically all processes in the Earth's magnetosphere. Many of them have immediate impact on human society and its developed technology. On the basis of solar wind monitoring we would like to predict effects at the Earth's magnetosphere. Solar activity is transmitted by solar wind with frozen magnetic field as different structures and instabilities, such as magnetic clouds, coronal mass ejections, interplanetary shocks and other discontinuities. Additional perturbances and instabilities are generated by interactions of the solar wind with the Earth's magnetosphere. The mentioned perturbances and changes in solar activity become starting mechanisms of geomagnetic activities with consequence on the Earth's surface and its surroundings. For predictions of timing and intensities of magnetospheric processes it is important to know properties of propagation and way of interaction of the given perturbances of the solar wind with regions near to the Earth, Earth's magnetosheath as well as outer magnetosphere.

This thesis is ordered as follows. After the introduction, chapter 2 overviews present knowledge about structures in the solar wind. Chapter 3 introduces the aims of the thesis and the chapter 4 presents used data sets. Chapter 5 contains study of the fast forward shocks and their propagation into the Earth's magnetosphere, and comparison of some results with the global MHD simulations. Finally, results and conclusions of the thesis are summarized in the last Chapter 6.

This thesis was prepared under a support by the Research plan MSM 0021620860 that is financed by the Ministry of the Education of the Czech Republic.

Chapter 2

Introduction to the Sun-Earth relations

2.1 Solar Wind

The solar wind (SW) is a flow of almost totally ionized plasma with frozen solar magnetic field which expands almost radially to the interplanetary space, therefore to our Earth. The density of characteristic solar wind plasma in the solar corona is $10^{15}\mathrm{m}^{-3}$. It decreases to $10^{7}\mathrm{m}^{-3}$ in distance of 1 AU, approximately orbit of the Earth (Kivelson and Russell, 1995).

Typical solar wind consists of 95 % protons, 4% α particles a 1 % heavy elements. Solar wind speed varies from 300 $\mathrm{km{\cdot}s^{-1}}$ to 1400$\mathrm{km{\cdot}s^{-1}}$, average value is around 450 $\mathrm{km{\cdot}s^{-1}}$ (Table 2.1). The solar wind is non-uniform. It depends highly on heliolatitude. Figure 2.1 shows the solar wind speed as a function of heliolatitude (McComas et al., 1998b). The solar wind speed data were obtained by the SWOOPS instrument (Solar Wind Observations Over the Poles of the Sun) onboard the Ulysses spacecraft. The bottom panel shows the sunspot number over the period 1992 – 2003. The first orbit occurred through the solar cycle declining phase and minimum, while the second orbit occurred through the solar maximum. The polar regions in the left panel correspond to the high speed solar wind and low density. The equatorial regions are characterized by the slow speed and higher density. The right panel covers to the solar maximum activity and shows more disturbed situation.

In the simplest situation, solar magnetic field is formed into a spiral (Parker, 1958, 1963), like the spiral of Archimedes, caused by the rotation of the Sun. This structure is called the Parker spiral, see Figure 2.2a.

Observations show that solar wind is not stationary. Moreover, the solar wind speed

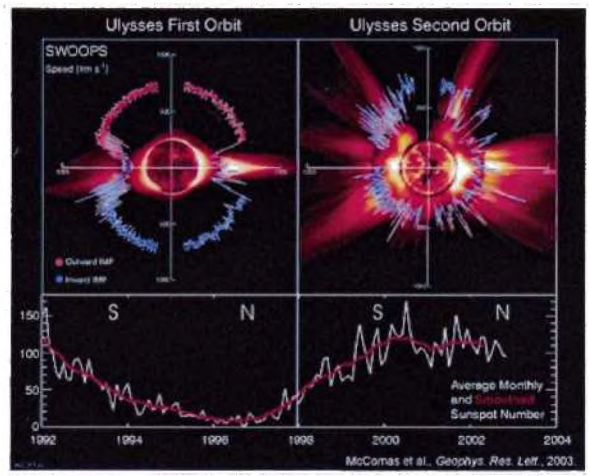

Figure 2.1: The polar plot of the solar wind speed as a function of heliolatitude measured by satellite Ulysses, the first orbit during solar activity minimum and the second orbit during solar maximum activity. Adapted from McComas et al. (1998b).

Proton density	6.6 cm^{-3}
Electron density	7.1 cm^{-3}
He density	0.25 cm^{-3}
Flow speed (nearly radial)	450 $km \cdot s^{-1}$
Magnetic field (induction)	7 nT
Proton temperature	1.2 x 10^5 K
Electron temperature	1.4 x 10^5 K

Table 2.1: Observed properties of the solar wind near the orbit of the Earth (1AU). Kivelson and Russell (1995)

is different in different parts of the interplanetary space, see Figure 2.2b. Faster solar wind in some regions drifts magnetic lines faster than in neighboring regions. Interaction regions (Whang, 1991b) develop near 1AU and they are observed as clearly defined pressure enhancements, and magnetic field strengthening. As a stream moves outward, the pressure fronts begin to be steeper and form the corotating shocks (fast/reverse) at the boundaries of the interaction region. Because of the recurrent nature of the interaction regions, they are called corotating interaction regions (CIR) (Smith and Wolfe, 1976), see Figure 2.3.

Clouds of energetic particles (CME) Figure 2.2c are thrown out from the Sun through slower solar wind (Whang, 1991a). The interaction can produce shocks in the coronal space. The impact of the momentum flux is the driving force for the formation of CME associated shocks. Interplanetary shocks (fast forward shock) are formed in front of the

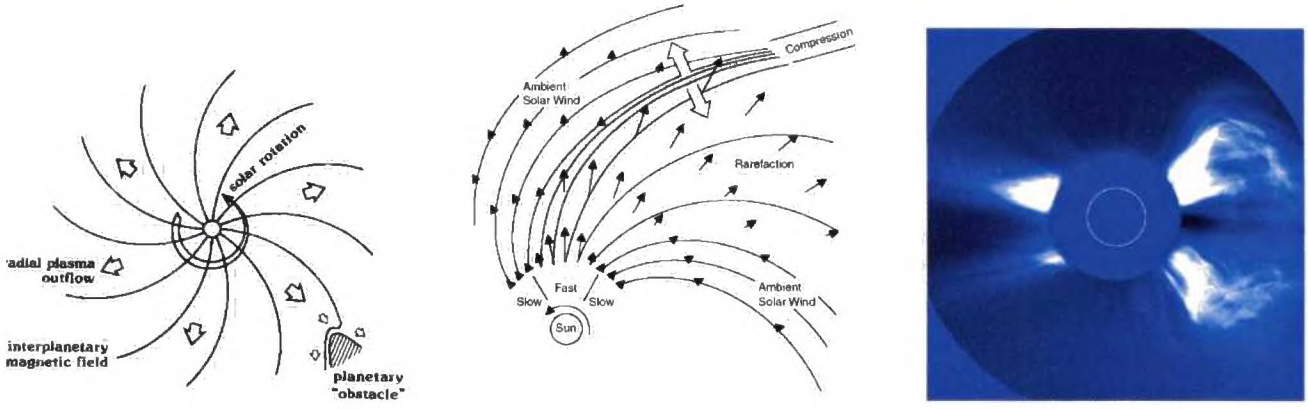

(a) (b) (c)

Figure 2.2: Sources of the shocks in the solar wind: (a) spiral interplanetary magnetic field lines frozen into solar wind, Parker spiral. Solar wind interaction with the planetary magnetosphere and formation of the planetary bow shock, (b) a more realistic schema of magnetic field of the Sun: collisions of faster solar wind with slower solar wind lead to formation of corotating interaction regions as well as interplanetary shocks , and (c) coronal mass ejection (CME) from 6 November 1997 as recorded by the LASCO C2 coronagraph at 12:36 UT. An interplanetary shock forms in front of the CME.

CME.

In the solar wind, we observe a so-called sector structure. It means, that we encounter long intervals with north or south orientations of component B_z during one turn of the Sun, so-called Carrington rotation. B_z is a component of the magnetic field. Solar rotation axis isn't exactly perpendicular to the ecliptic plane ($\sim 7^o$). The simplest case is a two-sector model, which corresponds to a simple solar magnetic dipole in minimum of solar activity. More often observation can be described by a four-sector model, which corresponds to the complicated idea of the solar magnetic field in corona with significant quadrupole component.

Three types of magnetosonic waves propagate in the magnetized solar wind. They are divided by their speeds to fast v_F, intermediate v_I, and slow v_S waves. Fast and slow waves have been described by Burlaga (1971). At fast mode waves, plasma pressure and magnetic field increase, whereas at slow mode waves, plasma pressure increases and magnetic field decreases. Intermediate mode waves bend the flow and magnetic field, but do not compress them. The density changes only in the anisotropic plasma ($T_\perp \neq T_\parallel$).

The wave speeds depend on different parameters: angle θ between the propagation vector of the waves to the magnetic field $\mathbf{B}$, and sound c_S and Alfven v_A speeds:

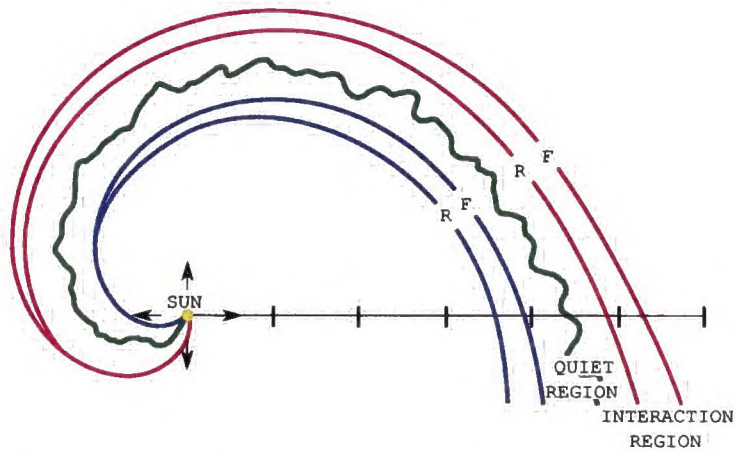

Figure 2.3: Two CIRs and intervening quiet region. F and R indicate forward and reverse shocks. Whang (1991b)

$$v_I = \sqrt{v_A^2 \cos^2\theta} \tag{2.1}$$

$$v_F = \sqrt{\frac{1}{2}[(v_A^2 + c_S^2) + \{(v_A^2 + c_S^2)^2 - 4v_A^2 c_S^2 \cos^2\theta\}^{\frac{1}{2}}]} \tag{2.2}$$

$$v_S = \sqrt{\frac{1}{2}[(v_A^2 + c_S^2) - \{(v_A^2 + c_S^2)^2 - 4v_A^2 c_S^2 \cos^2\theta\}^{\frac{1}{2}}]} \tag{2.3}$$

where

$$c_S = \sqrt{\frac{\gamma p}{\rho}}, v_A = \frac{B}{\sqrt{\mu_0 \rho}} \tag{2.4}$$

p means the plasma pressure, ρ is the mass density, and γ is the ratio of specific heats. $v_F \geq v_I \geq v_S$ for all parameters (θ, c_S, v_A).

The solar wind speed can be described with slow/intermediate/fast Mach numbers. Mach number is ratio of the solar wind speed to the corresponding wave speeds:

$$M_F = \frac{v_{sw}}{v_F}, M_I = \frac{v_{sw}}{v_I}, M_S = \frac{v_{sw}}{v_S} \tag{2.5}$$

Alfven Mach number is given by the ratio:

$$M_A = \frac{v_{sw}}{v_A} \tag{2.6}$$

2.1.1 Rankine-Hugoniot conditions and MHD discontinuities

Typical solar wind is much quicker than the fastest magnetosonic waves in this environment $c\sqrt{(B^2+\gamma p)+\gamma p)/\mu_0 m_i n}$. In front of the Earth's magnetosphere, there is a standing, planetary shock created in the solar wind, which is called the bow shock. The solar wind speed is decelerated here from a supersonic to subsonic state. This bow shock can be presented in the magnetohydrodynamic *(MHD)* approximation as a discontinuity, where the fluxes of mass, momentum and energy are conserved. Conditions of jumps can be derived from MHD equations.

A complete system of these equations (e.g., Szabo (1994)) is given as follows: Equation 2.7 means the equation of continuity, Equation 2.8 expresses the conservation of momentum, Equation 2.9 means the conservation of energy and Equations 2.10 and 2.11 come out from Maxwell equations.

$$\frac{\partial \rho}{\partial t} = -\nabla \cdot \rho \mathbf{u} \tag{2.7}$$

$$\frac{\partial \rho \mathbf{u}}{\partial t} = -\nabla \cdot \left(\rho \mathbf{u}\mathbf{u} + \left(p + \frac{B^2}{2\mu_0} \right) - \frac{1}{\mu_0}\mathbf{B}\mathbf{B} \right) \tag{2.8}$$

$$\frac{\partial w_{tot}}{\partial t} = -\nabla \cdot \left(\left(\frac{1}{2}\rho u^2 + \frac{\gamma p}{\gamma - 1} + \frac{1}{\mu_0} B^2 \right) \mathbf{u} - \frac{\mathbf{u} \cdot \mathbf{B}}{\mu_0}\mathbf{B} - \frac{\eta}{\mu_0}\mathbf{j} \times \mathbf{B} \right) \tag{2.9}$$

$$\frac{\partial \mathbf{B}}{\partial t} = \nabla \times (\mathbf{u} \times \mathbf{B} - \eta \mathbf{j}) = -\nabla \cdot (\mathbf{u}\mathbf{B} - \mathbf{B}\mathbf{u}) - \nabla \times \mu_0 \mathbf{j} \tag{2.10}$$

$$0 = \nabla \cdot \mathbf{B} \tag{2.11}$$

where the total density of energy w_{tot} is

$$w_{tot} = \frac{1}{2}\rho u^2 + \frac{p}{\gamma - 1} + \frac{1}{2\mu_0} B^2 \tag{2.12}$$

ϱ is the mass density, $p = nkT$ is the total scalar isotropic thermal pressure, $\mathbf{u}$ is the plasma bulk velocity, $\mathbf{B}$ is the magnetic field, η is the magnetic resistivity ($\eta = \frac{1}{\mu_0 \sigma}$), γ is the ratio of the specific heats, μ_0 is the permeability of free space, σ is the conductivity, and $\mathbf{j}$ is the current density.

Time derivations are equal to zero in a stationary *(time invariable)* case.

Further, there are supposed an infinitesimal thin layer and a stationary system. It means time independent variables. This assumption of zero thickness corresponds to the assumption of one-dimensional layer. It can be formulated as this: if value f is density, momentum or energy, $\mathbf{u}$ is a drift velocity, it is

$$\frac{\partial f}{\partial t} = -\nabla \cdot f\mathbf{u} \tag{2.13}$$

from where $fu_n = const$, where u_n is a normal component of the drift velocity with respect to the discontinuity. It can be written as the following relation:

$$[fu_n] \equiv f_d u_{nd} - f_u u_{nu} = 0, \tag{2.14}$$

where suffixes d and u in the equation mean downstream and upstream to the discontinuity, in the sense of direction of the flow. In other words, flux f is constant across the thin layer. Rankine-Hugoniot conditions suppose one-dimensional layer with zero thickness and ideal MHD equations, accordingly, we suppose zero magnetic resistance ($\eta = 0$). Square brackets denote differences of values between regions before and after discontinuity:

$$\mathbf{n} \cdot [\rho\mathbf{u}] = 0 \tag{2.15}$$

$$\mathbf{n} \cdot \left[(\rho\mathbf{uu}) + \left(p + \frac{B^2}{2\mu_0}\right) - \frac{1}{\mu_0}\mathbf{n} \cdot \mathbf{BB}\right] = 0 \tag{2.16}$$

$$\mathbf{n} \cdot \left[\left(\frac{1}{2}\rho u^2 + \frac{\gamma p}{\gamma - 1} + \frac{1}{\mu_0}B^2\right)\mathbf{u}\right] - \frac{1}{\mu_0}\mathbf{n} \cdot [(\mathbf{u} \cdot \mathbf{B})\,\mathbf{B}] = 0 \tag{2.17}$$

$$\mathbf{n} \times [\mathbf{u} \times \mathbf{B}] = 0 \tag{2.18}$$

$$\mathbf{n} \cdot [\mathbf{B}] = 0 \tag{2.19}$$

Magnetic field $\mathbf{B}$ can be divided into two components, tangent and normal, where $B^2 = B_n^2 + B_t^2$. The normal component of the magnetic field is written as $\mathbf{n} \cdot \mathbf{B} = B_n$ and the normal component of drift velocity is written as $\mathbf{n} \cdot \mathbf{u} = u_n$, from equation 2.19 it comes out the jump condition across the layer is $[B_n] = 0$. It follows, that B_n is constant. So, the normal component of induction of the magnetic field doesn't change across the layer. From equation 2.15 it follows the relation $[\rho u_n] = 0$. From $\rho u_n \equiv f_n = const.$ we can separate cases, where $[u_n] = 0$ and call them simple MHD discontinuities. Mass flux across their surface is zero. On the other hand, the fluid moves parallel to the surface of these discontinuities. The discontinuities are carried by the solar wind.

The case $[u_n] \neq 0$ corresponds to the shocks. Shocks propagate in the solar wind with a specific speed. The mass flux across the surface is non-zero.

2.2 Discontinuities

There is no change of perpendicular component of the solar wind speed across MHD boundary ($[u_n] = 0$). Three cases can be found:

The first case is a contact discontinuity (CD). It comes out from equations 2.18 and 2.19, which are derived from the Maxwell equations. There are $u_n = 0$ and $B_n \neq 0$. It means that jump in tangent component of the magnetic field is zero $[B_t] = 0$. The jump in tangent component of the velocity is also zero $[u_t] = 0$. $u_n = 0$ and $[p] = 0$. Density and temperature can have any values (they can change across the surface) $[\rho] \neq 0$ and $[T] \neq 0$.

Another type is a tangential discontinuity (TD) – tangent boundary, where velocity and magnetic field are tangential. It means that $u_n = 0$ and $B_n = 0$ here. $[u_t] \neq 0$ and $[B_t] \neq 0$. The density can have any value $[\rho] \neq 0$, but pressure p is related to B_t: $\left[p + \frac{B_t^2}{2\mu_0}\right] = 0$ and it comes out from a substitution of previous two conditions u_n and B_n to Ml$\left[p + \frac{B_t^2}{2\mu_0}\right]$ions, so the sums of dynamic and magnetic pressures are equal before and after the discontinuity.

Rotational discontinuity (RD) is a discontinuity in which the density is continuous. It means that if mass flux is continuous then also normal component of velocity is continuous $u_n = const.$ ($[\rho] = 0$ and $[u_n] = 0$). The normal velocity has value $u_n = \frac{B_n}{\sqrt{\mu_0 \rho}}$.

2.3 Shocks

Here, shocks are structures, where the solar wind velocity in normal direction changes over the front ($[u_n] \neq 0$). There is some dissipation and compression across the shock. There are many possibilities how to classify shocks.

For the case of the planetary bow shock, Figure 2.2a, the shock surface is curved. Hence, shock structures and properties differ according to changes of magnetic field direction to the shock surface. A convenient way to describe this direction is angle θ_{Bn}, the angle between the direction of the shock front normal and the upstream magnetic field.

We classify two main types of shocks, Figure 2.4: strictly perpendicular and strictly parallel. In the case of *parallel shocks*, the vector of the magnetic field is parallel to the normal line of shock. The vector of the magnetic field is not changed across the shock. There is $B_t = 0$. In the case of *perpendicular shocks*, there is $B_n = 0$. Afterwards, there is $\vec{B} \perp \vec{n}$, $\theta_{Bn} = 90^o$. Pressure of the magnetic field increases across the shock.

The terms quasi-parallel and quasi-perpendicular are used to divide the range of possible θ_{Bn} values, where the shocks have similar properties as the above described marginal cases. Also, the term oblique shock is used to describe a shock, which is neither perpendicular

nor parallel.

Properties of a *quasiparallel shock* are similar to the parallel shock. The angle θ_{Bn} is less than 45^o. A *Quasiperpendicular shock* is similar to the perpendicular shock and the angle θ_{Bn} is greater than 45^o.

The importance of the parallel/perpendicular classification is given by particle motion, which is headed away from the shock. The motion has two parts: motion along the magnetic field, and gyration motion. In the case of the parallel shock, particles propagate along the magnetic field lines which are perpendicular to the shock surface. Particles are carried through the shock and some may depart easily upstream. On the other hand, at the perpendicular shock, magnetic field lines are parallel to the shock surface. So, particle motion along the magnetic field does not let them pass away from the shock cavity easily.

For the case of description of interplanetary shocks we can use plasma parameters (Burlaga, 1971). Comparing to the Earth's magnetosphere, the IP shocks are much larger structures, so here, we suppose planar surfaces in the solar wind. According to changes of plasma parameters, such as magnetic field, plasma density, temperature and speed, shocks can be classified as follows fast/slow/intermediate shocks and forward/reverse shocks, see Table 2.3, and Figure 2.5.

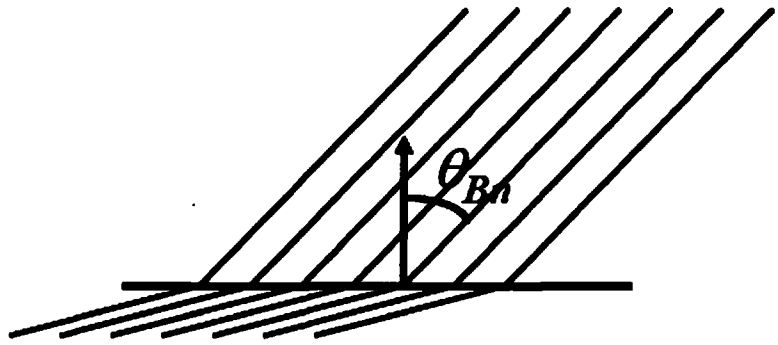

Figure 2.4: Basic figure of the distribution of shock according to the angle θ_{Bn}. At first shock is strictly perpendicular $\theta_{Bn} = 90^o$, than quasiperpendicular $\theta_{Bn} > 45^o$, than quasi-parallel $\theta_{Bn} < 45^o$ and finally, strictly parallel $\theta_{Bn} = 0^o$.

2.3.1 Sudden commencements/sudden impulses

Impulse geomagnetic disturbances (Araki, 1977; Villante et al., 2004; Gonzales et al., 1994; Keika et al., 2008) (*Sudden Storm Commencements (SSC)* or *Sudden Impulses (SI)*) are

Shock	v_{sw}	N_p	V_{th}	B
forward fast shock FFS	increase	increase	increase	increase
reverse fast shock RFS	increase	decrease	decrease	decrease
forward slow shock FSS	increase	increase	increase	decrease
reverse slow shock RSS	increase	decrease	decrease	increase

Table 2.2: Changes of plasma parameters across shocks in the solar wind. N_p means the plasma density, V_{th} the thermal velocity, v_{sw} the solar wind velocity, and B the magnetic field.

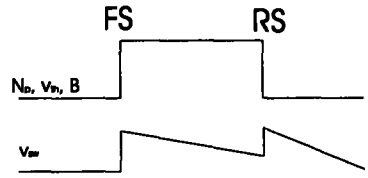

Figure 2.5: Basic picture, which describes progression of parameters of the forward shock *FS* and reverse shock *RS* in CIR. Upper curve describes the plasma density N_p, the thermal velocity v_{th} and the magnetic field B. Bottom curve describes the solar wind speed v_{sw}.

magnetic field phenomena observed on the Earth's surface that are produced by interplanetary forward shocks impinging on the Earth's magnetosphere.

As an example of SI is presented in Figure 2.6. The last panel in Figure 2.6a shows B_z component measured by the Cluster spacecraft. A B_z increase is one of the most suitable factors that indicate magnetospheric compression. The B_z increase coincides with an increase in the total pressure, see Figure 2.6b (last panel).

2.4 Different methods for shock normal determination

For the study of the shock propagation we need to determine some parameters of the shocks, such as shock normals, and shock speeds. There is a variety of approaches using observations at a single spacecraft or simultaneous data from multiple spacecraft. Some methods can provide only the normal of the shock. So, the velocity of the shock is usually derived from the mass flux conservation law:

$$V_s = \frac{\Delta[\rho \mathbf{V}]}{\rho} \cdot \mathbf{n} \tag{2.20}$$

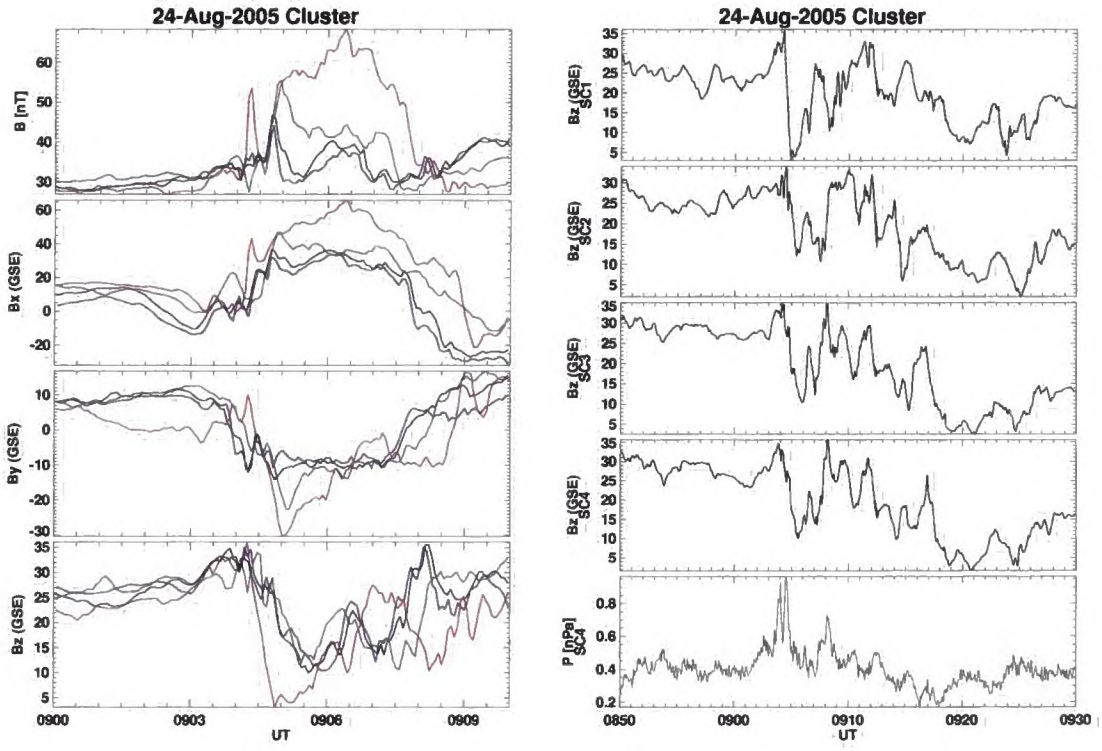

(a) (b)

Figure 2.6: (a) An overview plot of variations of the magnetic field observed by four Cluster spacecraft located in plasma sheet between 0900 and 0910 UT, see Keika et al. (2008), (b) Top four panels show separately B_z observed by the Cluster spacecraft, and the last panel shows total pressure. In the GSE coordinate system.

2.4.1 Minimum variance analysis

Variance analysis (Paschmann et al., 1988) is based on a search for minimum change in one component of the magnetic field from single spacecraft data. A single spacecraft passing through a 1-D surface observes variations in the magnetic field. Since $\nabla \cdot \mathbf{B} = 0$, the normal component of the magnetic field must be constant. So, the minimum variance analysis looks for a unique direction along which the product of $\vec{B} \cdot \vec{n}$ is zero (shows the minimum variance). This direction corresponds to the normal direction.

This method fails for pure MHD shock solutions or if the variance direction is degenerated. In other words, the three eigenvalues of variance matrix are not distinct.

Except minimum variance on the magnetic field, we can apply this method using mass flux MVA ($\rho\mathbf{v}$), or maximum variance on the electric field MVA ($\mathbf{E}$).

2.4.2 Coplanarity theorem

The normal to a planar surface can be determined using coplanarity theorem if the magnetic field on both sides of the shock and shock normal lie in the same plane. The velocity jump across the shock also lies in that plane.

Except magnetic (Lepping and Argentiero, 1971) and velocity (Abraham-Shrauner, 1972) coplanarity conditions:

$$\mathbf{n}_{MC} = \pm \frac{(\mathbf{B_d}) \times \Delta[\mathbf{B}]}{|(\mathbf{B_d}) \times \Delta[\mathbf{B}]|} \tag{2.21}$$

$$\mathbf{n}_{VC} = \pm \frac{\mathbf{V_d} - \mathbf{V_u}}{|\mathbf{V_d} - \mathbf{V_u}|} \tag{2.22}$$

there is a variety of vectors which lie in the shock plane, such as cross-product of the upstream and downstream magnetic field, and the cross-product between the upstream or downstream magnetic field or their difference with the change in bulk flow velocity.

Magnetic coplanarity fails for $\theta_{B_n} = 0^o$ or 90^o. Three mixed methods (Abraham-Shrauner and Yun, 1976) requiring both plasma and magnetic field data are commonly used:

$$\mathbf{n}_{MX1} = \pm \frac{(\mathbf{B_u} \times \Delta\mathbf{V}) \times \Delta\mathbf{B}}{|(\mathbf{B_u} \times \Delta\mathbf{V}) \times \Delta\mathbf{B}|} \tag{2.23}$$

$$\mathbf{n}_{MX2} = \pm \frac{(\mathbf{B_d} \times \Delta\mathbf{V}) \times \Delta\mathbf{B}}{|(\mathbf{B_d} \times \Delta\mathbf{V}) \times \Delta\mathbf{B}|} \tag{2.24}$$

$$\mathbf{n}_{MX3} = \pm \frac{(\Delta\mathbf{B} \times \Delta\mathbf{V}) \times \Delta\mathbf{B}}{|(\Delta\mathbf{B} \times \Delta\mathbf{V}) \times \Delta\mathbf{B}|} \tag{2.25}$$

2.4.3 Rankine–Hugoniot method

Previous methods of shock normal determinations use a small subset of Rankine–Hugoniot (RH) equations, which were described above. More reliable approach is to take more of the RH equations into account in order to establish a full set of upstream and downstream quantities (including the shock normal direction). Since the thermal properties of the shock processes often involve kinetic and anisotropic processes, it's better to avoid those relations that involve plasma pressure.

Lepping and Argentiero (1971) first put such a scheme together, but still it relied on magnetic coplanarity. Viñas and Scudder (1986) overcame this difficulty. They developed

a fast iterative method based on a six equation subset of RH equations. The technique uses the three-dimensional magnetic field and plasma observations. The method is reliable at all θ_{B_n} angles regardless of the shock strength or geometry. Szabo (1994) improved this method by involving the plasma temperature observations through the perpendicular momentum flux and energy density flux conservation equations.

However, this method relies on the selection of the upstream and downstream data intervals. Also the assumption of planarity may be problem in this method.

2.4.4 4 S/C method

If the same planar shock passes several spacecraft (at least 4 spacecraft), their positions and shock observation times can be used to determine the shock normal direction and propagation speed.

$$\mathbf{r}_{\alpha\beta} \cdot \mathbf{n} = V_s \cdot t_{\alpha\beta} \tag{2.26}$$

where $\mathbf{r}_{\alpha\beta}$ is the separation vector between two satellites α and β, and $t_{\alpha\beta}$ is the time difference between observations. V_s is the shock propagation speed.

If the separation vectors are large, the assumption of planarity may fail. This method also fails if the spacecraft are nearly coplanar.

2.4.5 Combined approaches

If there are 4 spacecraft available, it is possible to add to the system Equation 2.26 any or all of the coplanarity theorems to improve the shock parameter determination.

Russell et al. (2000) compared several different methods of shock normal determination and shock speed estimations. They concluded that magnetic coplanarity is most accurate from the single spacecraft methods.

2.5 Structures near to Earth

The Earth's internal magnetic field has an dipole structure in the first approximation. The strength of the magnetic field at the equator on the Earth's surface is about 30 $\times 10^3$ nT, and at 10 Earth radii (1 Earth radius is 6378 km) about 30 nT.

The Earth's magnetic field is an obstacle, see Figure 2.7, to the solar wind plasma. The solar wind flows supersonically with an average speed 450 km·s^{-1}. The plasma wave velocity c_s has a typical value 40 km·s^{-1} here. The plasma wave replaces sonic wave in this

region. The function of this non-linear wave is to slow down the solar wind speed. So, the solar wind can flow around the Earth.

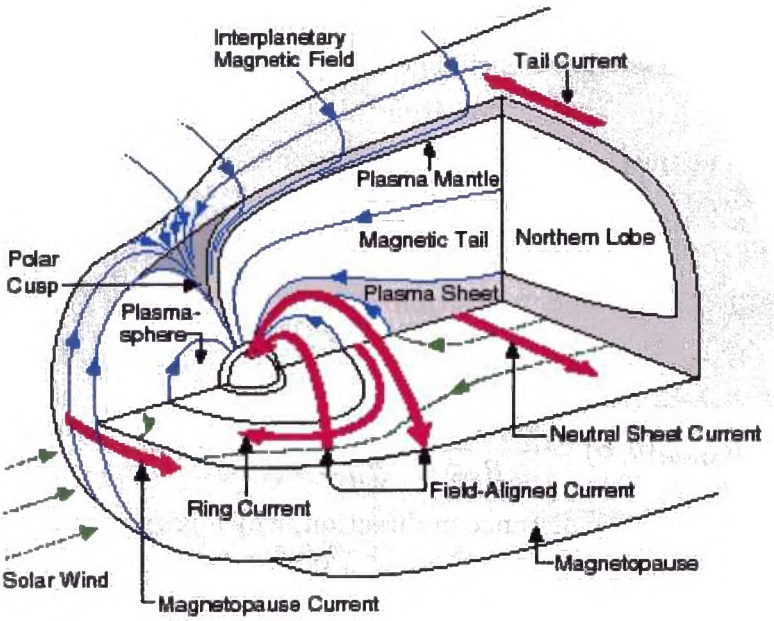

Figure 2.7: Earth as an obstacle for the incoming solar wind has different regions with various plasma parameters and differs with significant processes. Various magnetospheric currents act as sources of the external magnetic field that complements the Earth's internal field.

Bow shock

Bow shock is the first structure that the solar wind encounters in the Earth's surroundings. The solar wind is slowed-down, deflected and its temperature increases here.

The bow shock front moves in time depending on solar wind parameters. The shape, the position, and the motion of the bow shock have been studied for many years. The simplest model of the bow shock is a part of surface of a rotating ellipsoid, which is described by equation in the GSE coordinates:

$$y = \frac{10.4}{\sqrt[6]{nv^2}} \cdot \sqrt{520 - 0.4x^2 - 42x} \tag{2.27}$$

where Y is the distance from the X_{GSE} axis in Earth's radii, X is the position at this axis, $X \in \langle -10\ R_E; 12\ R_E \rangle$, v [km·s^{-1}] is velocity of the solar wind, and n [cm^{-3}] is the

plasma density of the solar wind. This model supposes that the solar wind propagates only along the X_{GSE} axis.

Other models were proposed, e.g., by Formisano (1979), Nemecek and Safrankova (1991), Farris and Russell (1994), Peredo et al. (1995), Merka et al. (2003), Jeřáb et al. (2005) and many others. First simple models include ellipsoids as general surfaces of second-order, in which coefficients change according to various solar wind parameters. It's supposed that the shape and the position of the bow shock is influenced mainly by the dynamic pressure of the solar wind and Mach number.

Formisano(1979) model is a classical model of the bow shock suitable for our studies. Jeřáb et al. (2005) improved the model of Formisano (1979) in order to exclude some overestimation of the bow shock position. The influence of parameters of the solar wind on position of the Earth's bow shock is according to Formisano et al. (1971)

$$R_{Model}(\theta,\phi) = \frac{R_S(\theta,\phi)}{R_{S0}} \cdot \frac{C}{\sqrt[6]{nv^2}} \cdot \left(1 + 1.1\frac{(\gamma-1)M_A^2+2}{(\gamma+1)M_A^2}\right) \tag{2.28}$$

where $R_{Model}(\theta,\phi)$ is the distance in direction, which is given by angles θ and ϕ, $R_S(\theta,\phi)$ is the distance of model surface in direction of the angle, R_{S0} is the distance of the subsolar point, γ is the polytropic index, M_A is the Alfven Mach number and C is constant given by formula

$$C = \sqrt[6]{\frac{f^2 \cdot B_0^2}{2\pi K m}} \sim 9.6 \tag{2.29}$$

where $B_0 = 3.12 * 10^{-5}$ T and it is the intensity of the Earth's dipole magnetic field at equator, m is the average ion mass, K sets dimension of convection of particles of the solar wind to the Earth's magnetosphere and f means the ratio of geomagnetic field on the side of the magnetopause and undisturbed dipole magnetic field in the present position ($f = 1$ for undisturbed field).

The model surface of second-order is described in the GSE coordinates as

$$a_{11}X^2 + a_{22}Y^2 + a_{33}Z^2 + a_{12}XY + a_{14}X + a_{24}Y + a_{44} = 0 \tag{2.30}$$

where coefficients are shown in Table 2.3.

2.5.1 Processes at the bow shock

Passage over the bow shock means change in properties of the solar wind. Its velocity decreases and deflects from the original direction. As shown in Figure 2.8, there are two

coefficient	a_{11}	a_{22}	a_{33}	a_{12}	a_{14}	a_{24}	a_{44}
value	0.45	1	1.11	0.18	46.6	-4.16	-618

Table 2.3: Coefficients of the Formisano model (1979) of the bow shock.

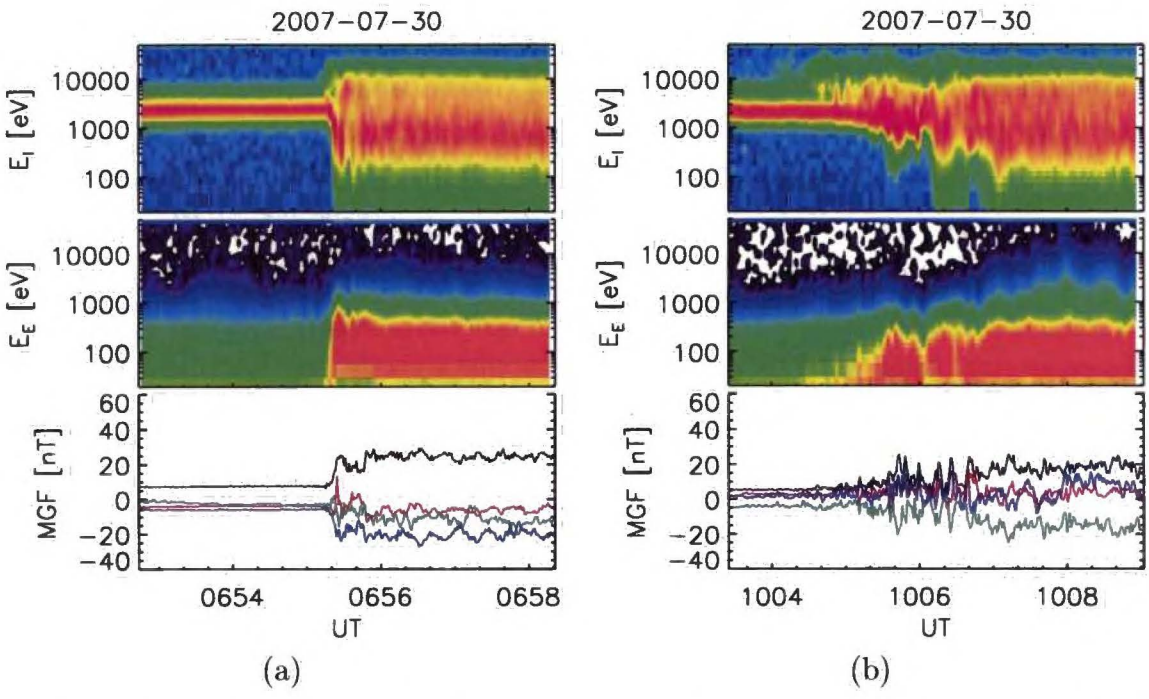

Figure 2.8: Themis observation: (a) Passage across the quasi-perpendicular and (b) quasi-parallel bow shock. The first two panels show energetic spectra of ions and electrons, and the last panel is the magnetic field magnitude and components.

passages across the Earth's bow shock in two different configuration: quasi-parallel and quasi-perpendicular shocks. The quasi-perpendicular bow shock passage is sharp. In the quasi-parallel bow shock, the boundary is not clear caused be processes at the bow shock.

2.5.2 Foreshock

While most of solar wind particles are transmitted across the bow shock, certain amount is reflected back to the solar wind.

If we use classification according to angle θ_{Bn} to describe the situation at the Earth's bow shock, we will get different cases of its configuration. In case of $\theta_{Bn} \in (0, 45^o)$, i.e. in the quasiparallel configuration, some particles reflect from the bow shock into the solar wind by effect of the magnetic mirror. The particle moves back along the magnetic lines, at

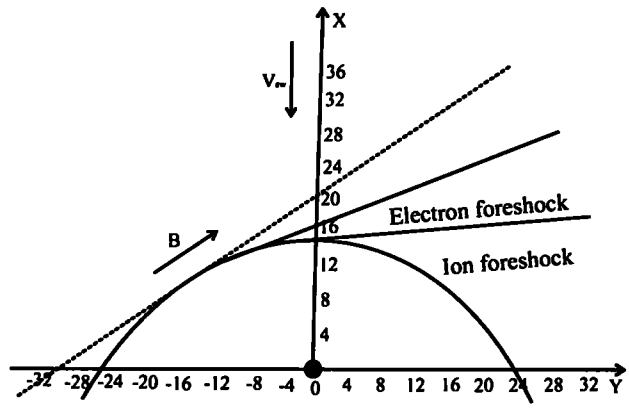

Figure 2.9: Section of the bow shock in GSE coordinates in plane XY, normal lines are parallel with the magnetic field **B**, electron and ion foreshock, solar wind speed v_{sw}.

the same time solar wind electric field has an effect on the particles. In case of $\theta_{Bn} > 45^o$ quasiperpendicular configuration, solar wind particles get to inner bow shock thanks to their gyration motion. There is higher intensity of the magnetic field, so particles decrease their gyration radius, move along the bow shock and get energy from the bow shock electric field (shock drift acceleration). Θ_{Bn} gradually increases along the bow shock. Then, particles are discharged to the solar wind and they fill region called *foreshock* (Kivelson and Russell, 1995), in Figure 2.9.

The region of foreshock is divided into *ion* and *electron* foreshocks. One of the reasons are different velocities of ions and electrons, so certain upstream regions cannot be reached by slower particles. Boundaries of electron and ion foreshocks have different angles with magnetic lines, which are tangent to the bow shock. The foreshock region is characteristic by the presence of strong fluctuations and populations of the energetic particles accelerated by various mechanisms at the shock.

Ion foreshock: There are three populations of energetic ions found in ion foreshock: reflected, diffuse and intermediate. They have comparable densities, but they differ in temperature, in velocity distribution and in interaction with the solar wind. Reflected ions almost don't interact with the solar wind. They move along magnetic lines, with respect to the $E \times B$ drift. Their spectrum of energy is narrow with top energy 10 keV. They are found on magnetic lines which are connected to quasiperpendicular region of the bow shock. Diffuse ions have strong interactions with the solar wind. Their energetic spectrum is wide with top energy near 40 keV. Diffuse ions are found in quasiparallel region.

Electron foreshock: Reflected electrons in foreshock have an origin in quasiperpendicular region being accelerated in a similar way as ions. Energy of accelerated electrons

can be 100 keV and more.

2.5.3 Magnetosheath

Magnetosheath is a middle region between the bow shock and the Earth's magnetosphere, where solar wind plasma flows around the magnetosphere. Particles are more deflected and heated here than in the solar wind. There are characteristic plasma fluctuations and turbulence observed here. The magnetosheath has not finite boundaries. Far away behind the Earth, more than 40 Earth's radii, it is practically impossible to recognize the solar wind and magnetosheath plasma.

2.5.4 Magnetopause

Magnetopause is a boundary, where the solar wind pressure is balanced with the magnetic pressure of the Earth's magnetosphere. Typical shape of the magnetopause is sketched in Figure 2.7.

Equilibrium of pressures can be described as

$$\left(\frac{B^2}{2\mu_0}+p\right)_d = \left(\frac{B^2}{2\mu_0}+p\right)_u \tag{2.31}$$

suffices d and u note downstream in the magnetosphere and upstream in the magnetosheath, B is the magnetic field, p is the plasma pressure, and μ_0 is permeability of vacuum. This equation is often simplified: magnetic pressure $\frac{B^2}{2\mu_0}$ is vanished outside of the magnetopause in direction to the solar wind. The dynamic pressure p is vanished inside of the magnetopause. We get equation

$$(p)_u = \left(\frac{B^2}{2\mu_0}\right)_d. \tag{2.32}$$

Electric currents flow inside the magnetosphere, by its nature magnetopause can be compared to the tangential discontinuity.

2.5.5 Magnetospheric cusp

Static models of the magnetic field around the Earth predict the existence of two neutral points at the magnetopause, as seen in Figure 2.7. These points are connected to the Earth with the magnetic lines, $\pm 78^o MLAT$ (magnetic latitude) and are called cusps.

Equation 2.32 cannot be used in the magnetospheric cusp. The cusp is one of regions, where the solar wind plasma can enter the Earth's magnetosphere.

2.5.6 Reconnection

Reconnection, Figure 2.10 (Kivelson and Russell, 1995), is a significant process of plasma transfer from the solar wind into the Earth's magnetosphere. It is the process whereby the magnetic field lines are effectively broken and reconnected, resulting in a change of magnetic topology, conversion of the magnetic field energy into the bulk kinetic energy and particle heating.

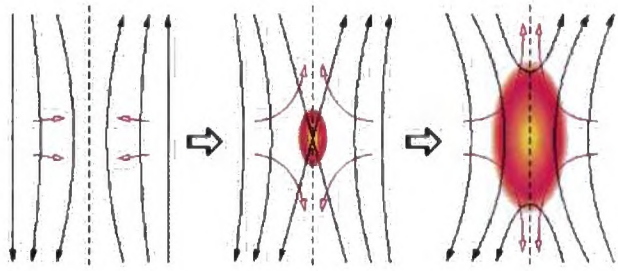

Figure 2.10: Effect of reconnection on the initially antiparallel magnetic-field geometry (left panel) and the resulting flows (right panel).

If the interplanetary magnetic field is southward, the reconnection occurs at the nose of the magnetopause and in the magnetotail at high rate (open magnetosphere). Magnetosheath particles flow along the newly opened field lines into the upper atmosphere, where they can create the polar lights. The plasma reaches the plasma lobes in the nightside, where it induces further reconnection of the magnetic field lines and the creation of plasmoids with frozen magnetic field.

When interplanetary magnetic field is northward, the reconnection between the magnetosheath magnetic field and the terrestrial magnetic field occurs beyond the polar cusp, but in a much smaller rate (closed magnetosphere).

2.5.7 Solar wind contribution to the bow shock motion

The variations in the dynamic pressure and velocity of the solar wind influence the bow shock position. The changes in the velocity makes ± 20 per cents (the left panel of Figure 2.11) in the magnetosphere radius but the change in density makes ± 80 per cents change (the right panel of Figure 2.11).

The dynamic pressure changes over the solar cycle about ±20 per cents (Petrinec et al., 1991). It makes small change of the magnetosphere size (about ±3 per cents). As shown in Figure 2.12, the solar wind proton density and speed are anticorrelated.

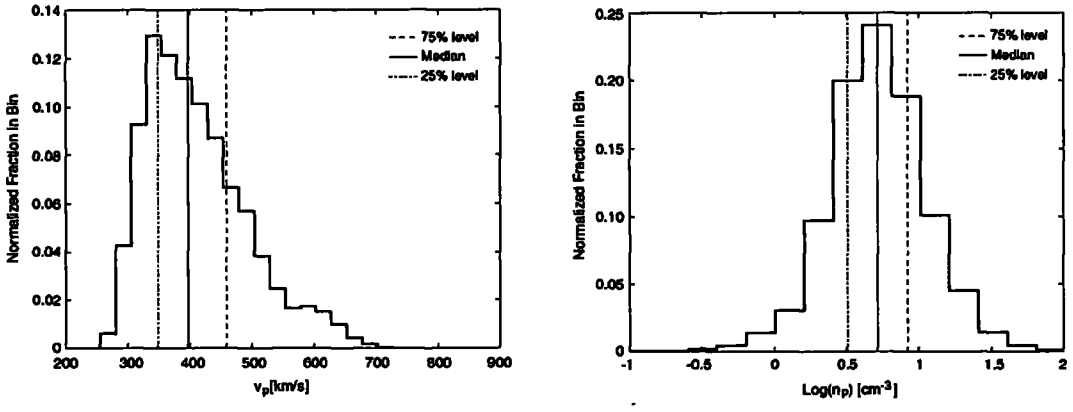

Figure 2.11: Histogram of the solar wind velocity (left panel) and density (right panel) derived from 18 months of ISEE-3 observations. Quartiles of the velocity are 348, 397, and 459 km/s. Quartiles of the density are 3.2, 5.2, and 8.4 cm^{-3}. Adapted from Newbury (2000).

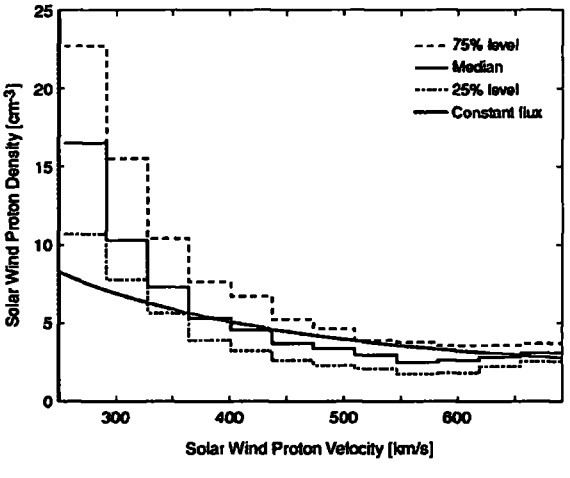

Figure 2.12: The variation of the solar wind density as a function of the solar wind velocity. Adapted from Newbury (2000).

2.5.8 Geomagnetic storms and substorms

A geomagnetic storm is a temporary disturbance of the Earth's magnetosphere caused by a disturbance in the solar wind. Associated with the solar coronal mass ejections (CME), or corotating interaction regions (CIR) (Tsurutani et al., 1995; Laughlin et al., 2008), a geomagnetic storm starts by an interplanetary shock which strikes the Earth's magnetosphere 24 to 36 hours after the event on the Sun. This only happens if the shock propagates in a direction toward the Earth. The solar wind pressure changes modify the electric currents in the ionosphere. Magnetic storms usually last 24 to 48 hours, but some may last for many days.

The main signature of a magnetic storm is a southward interplanetary magnetic field, weakening the northward field usually observed in equatorial regions. It suggests that its origin is a ring current carried by the outer radiation belt. In magnetic storms, the outer belt becomes much more intense, reinforced by protons coming from the tail, as well as by $O+$ ions from the ionosphere.

Geomagnetic substorms are brief (2-3 hour) magnetospheric disturbances that occur when the interplanetary magnetic field turns southward. A geomagnetic substorms (Akasofu, 1964) have been divided into three phases: growth phase, expansion phase, and recovery phase. These disturbances can be seen in the ground-based magnetometers (mainly at high latitudes) due to created/modified ionospheric currents. A level of their disturbation is described by the AE index (Davis and Sugiura, 1966). It is an auroral electrojet index obtained from a number (usually greater than 10) of stations.

2.6 Interaction of interplanetary shocks and rotational discontinuities with the Earth's bow shock

Interactions of the Earth's bow shock (BS) with interplanetary discontinuities can influence the Earth's magnetosphere. This type of interaction has been recently simulated by Yan and Lee (1996), Zhuang et al. (1981), Russell et al. (2000). MHD simulations (Yan and Lee, 1996) are based on the complete set of MHD equations described in previous part.

Initially, in the simulation Yan and Lee (1996), the bow shock and the incident interplanetary shock divide the whole domain into three uniform regions: (region A) the magnetosheath region, (region B) the solar wind region between the bow shock and incident shock or rotational discontinuity, and (region C) the solar wind region behind the incident shock or rotational discontinuity as shown in Figure 2.13(a) in the first panel.

2.6.1 Forward fast shocks (FFSs)

The incident forward fast shock (Figure 2.13(a), second panel) is propagating toward the Earth in the plasma frame. As the incident FFS crosses the bow shock, a series of shocks, expansion waves and discontinuities is generated downstream of the bow shock. These are led by a fast shock, followed by a slow expansion wave, a contact discontinuity, and a slow shock. In the plasma frame, the fast shock and the slow expansion wave propagate away from the bow shock toward the magnetopause, the slow shock propagates toward the bow shock and the contact discontinuity does not propagate. As the plasma flow speed in the x direction from Sun downstream of the bow shock is locally less than the fast-mode phase speed and above the slow-mode phase speed, all the generated waves are actually moving toward the magnetopause. Plasma density, pressure and magnetic pressure increase across the fast shock. The bow shock moves toward the Earth because of an enhanced solar wind pressure behind the FFS front.

2.6.2 Reverse fast shocks (RFSs)

When the incident RFS (Figure 2.13(a), third panel) crosses the bow shock, a fast expansion wave, a slow shock, a contact discontinuity, and a slow expansion wave are produced downstream of the bow shock. The plasma density and pressure increase while the magnetic pressure decreases. The contact discontinuity is created between the slow shock and the slow expansion wave. The plasma flow velocity and magnetic field do not vary across the contact discontinuity. After the shock-shock interaction, the bow shock moves further away from the Earth because of the sudden decrease of the dynamic pressure across the incident reverse shock.

2.6.3 Forward slow shocks (FSSs)

For the incident FSS (Figure 2.13(a), fourth panel) crossing of the bow shock, a fast shock, a slow shock, a contact discontinuity, and a slow expansion wave are generated. From the upstream to the downstream of the slow shock, the plasma density and pressure increase while the magnetic pressure decreases. From the magnetopause side to the bow shock side of the contact discontinuity, the plasma density increases. From the upstream to the downstream of the slow expansion wave, the plasma density and pressure decrease while the magnetic pressure increases.

2.6.4 Reverse slow shocks (RSSs)

As the incident RSS (Figure 2.13(a), fifth panel) crosses the bow shock, the simulation (Yan and Lee, 1996) shows that a fast expansion wave, a slow expansion wave, a contact discontinuity, and a slow shock are present downstream of the bow shock. Because of the lower dynamic pressure behind the incident RSS, the bow shock moves further away from the Earth after the impact of the RSS.

2.7 Incident rotational discontinuities

2.7.1 Interaction between rotational discontinuity and the bow shock

Cable and Lin (1998) in their 1D MHD simulation of interaction between a rotational discontinuity (RD) and the bow shock (BS) showed that the result is an MHD wave pulse that propagates downstream from the BS to the magnetopause. Inside the wave pulse, the plasma density, thermal pressure, dynamic pressure (ρv^2), and total pressure increase, while the magnetic field magnitude decreases. Before the approach of the RD, the radial component of the solar wind velocity is larger than the radial components of the slow and intermediate speeds at all points from the bow shock to the magnetopause. In contrast, after the RD has passed, the radial velocity is less than the slow and intermediate radial components at all points from the bow shock to the magnetopause.

Incident rotational discontinuity (Figure 2.13(b)) can propagate both in the forward and reverse directions in the plasma frame. Simulations of Yan and Lee (1996) suggest that the main product of this interaction includes an intermediate shock (IS) and a pair of slow shocks. A small Alfven wave and an entropy wave are also present. MHD models, according to Sibeck et al. (1997), predict that rotational discontinuities striking the bow shock result in both sunward- and antisunward-moving Alfven/slow mode waves in the magnetosheath.

2.7.2 Forward rotational discontinuities

There are no thermal pressure and magnetic pressure variations across a rotational discontinuity. The dynamic pressure remains constant since the plasma density does not change. As a result, there is no pressure variation associated with a rotational discontinuity. When RD interacts with the Earth's bow shock, a structure is generated in the magnetosheath

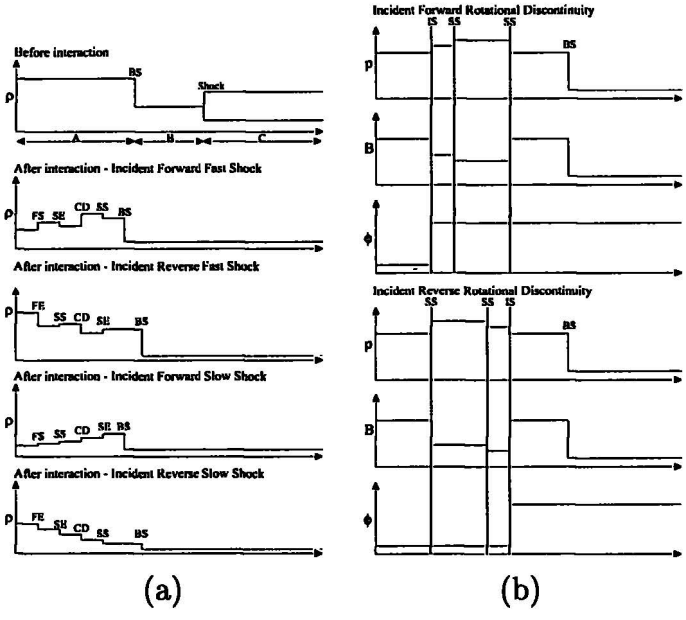

Figure 2.13: (a) A schematic plot of the bow shock interaction with an incident interplanetary shock. Four incident shocks types are considered: a forward fast shock, a reverse fast shock, a forward slow shock, and a reverse slow shock. Before the interaction, the domain is divided into three regions: A, B and C. Six different plasma regions are formed after the interaction. The regions are divided by: BS (bow shock), FS (fast shock), SE (slow expansion wave), CD (contact discontinuity) and SS (slow shock). (b) A schematic plot of the bow shock interaction with incident forward, and reverse rotational discontinuities. Only the main products of the interaction are shown in this plot (Yan and Lee, 1996).

with enhanced plasma density and dynamic pressure. The variation of the IMF may create a strong transient pressure pulse in the magnetosheath, as described by Yan and Lee (1996). The plasma density and thermal pressure decrease across the intermediate shock, similarly as across the slow shock. The tangential magnetic field rotates across the intermediate shock exactly the same angle as the incident rotational discontinuity. When the magnetic field does not satisfy a coplanar condition, the intermediate shock becomes a time-dependent intermediate shock.

2.7.3 Reverse rotational discontinuities

In the plasma frame, the incident rotational discontinuity propagates toward the Sun, instead of toward the Earth. Slow shocks and IS changed their order in the simulation as shown in Figure 2.13(b).

2.8 Incident MHD wave

MHD wave simulations were carried for the following: fast-mode waves, Alfven waves or slow-mode waves (Yan and Lee, 1994).

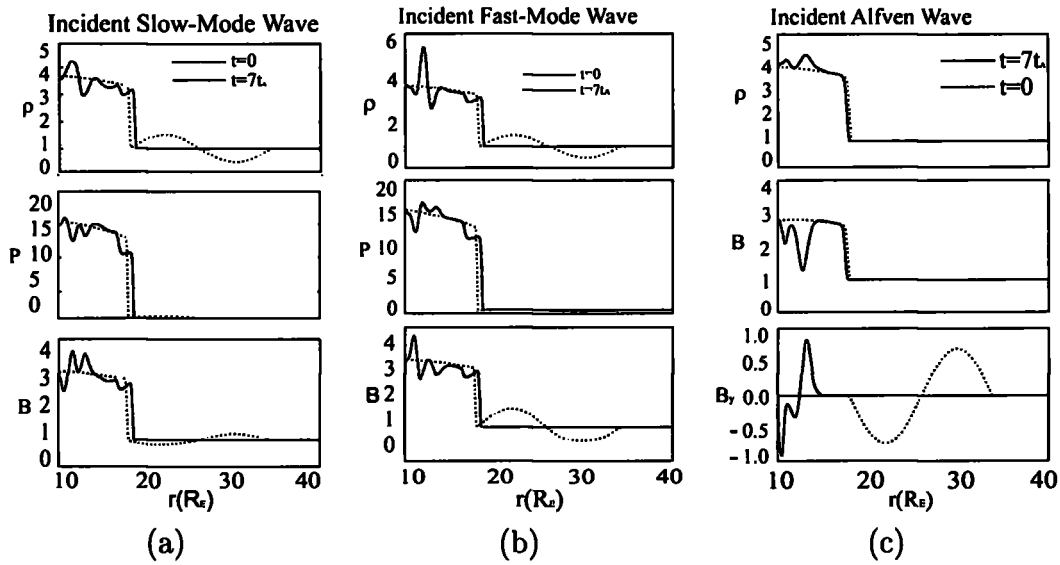

Figure 2.14: (a) Incident Slow-Mode Wave, (b) Incident Fast-Mode Wave, (c) Incident Alfvén-mode wave (Yan and Lee, 1994).

2.8.1 Slow-mode wave

The result of the interaction between the incident slow-mode wave, Figure 2.14a, and the bow shock consists of six waves downstream of the bow shock: one fast-mode wave, two Alfven waves, two slow-mode waves and an entropy wave. In the plasma frame, the fast-mode wave, one slow-mode wave and one Alfven wave propagate towards the magnetopause. The other slow-mode wave and Alfven wave propagate towards the bow shock. The entropy wave does not propagate in the plasma frame. The anti-correlation between the plasma pressure and the magnetic field indicate that these waves are mainly slow-mode waves.

2.8.2 Fast-mode wave

The positive correlation between the plasma density and magnetic field upstream of the bow shock at the time of the interaction with the bow shock indicates that incident wave is a fast-mode wave, see Figure 2.14b. The downstream fast-mode wave is also found to propagate from the bow shock to the magnetopause and then reflected back to the bow shock.

2.8.3 Alfven-mode wave

An Alfven-mode wave, Figure 2.14c, is imposed upstream of the bow shock. The plasma pressure and magnetic field magnitude are constant while B_y and B_z change sinusoidally. The anti-correlation between the density and magnetic field indicates the presence of slow-mode waves in the inner magnetosheath. The plasma density and pressure are found to be in phase (Yan and Lee, 1994).

2.9 Incident tangential discontinuities, HFA

Hot Flow Anomaly (*HFA*) is a type of instability created in the solar wind after interaction with the Earth's bow shock. The HFA is a phenomenon in dimension of few Earth's radii. This type of event has been studied since 1980s (Schwartz et al., 1985, 1988; Schwartz, 1995).

Interaction of the solar wind with the Earth's bow shock creates a population of back-streaming ions. When a tangential discontinuity arrives at the bow shock, reflected ions can be directed into the region of discontinuity. So, diamagnetic cavities are created there, filled

with hot, tenuous, and deflected plasma population. These cavities are swept downstream and can be observed in the magnetosheath (Šafránková et al., 2002).

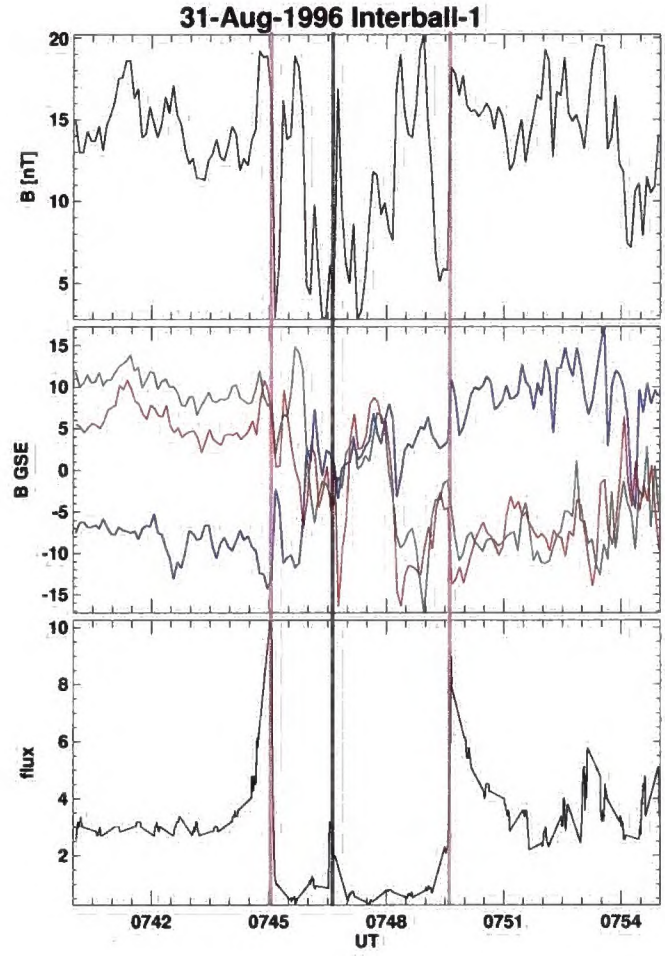

Figure 2.15: Observation of HFA by the Interball-1 satellite on August 31 th, 1996. Upper two panels show the solar wind magnetic field, the third panel shows the plasma flow. In GSE coordinates.

HFA (Paschmann et al., 1988; Schwartz et al., 1988; Thomsen et al., 1988) is often composed of two parts separated by increases of density. A behavior of particles in these regions are different.

Isotropic, near Maxwellian ion and electron velocity distributions are observed in hot central region ($T_i \sim 10^6 - 10^7 K$). Bulk flow velocity is much slower than the ambient solar wind and the flow is deflected at least tangential to the bow shock and sometimes $\sim 90°$ to the Sun-Earth line. Central magnetic field regions have depressed field and enhanced plasma density. Edge regions are compressed. Hot Flow Anomalies (HFAs) cause non-

negligible perturbations of the Earth's magnetosphere. They occur at a rate of several per day, and thus they may play a significant role in the solar-terrestrial dynamics (Schwartz et al., 2000). Observations studied by Sibeck et al. (1999) suggest that HFAs deflect a fraction of the incoming solar wind flow and pressure, thereby allowing the magnetopause to move outward.

2.10 Interaction of IPS with the bow shock and magnetopause

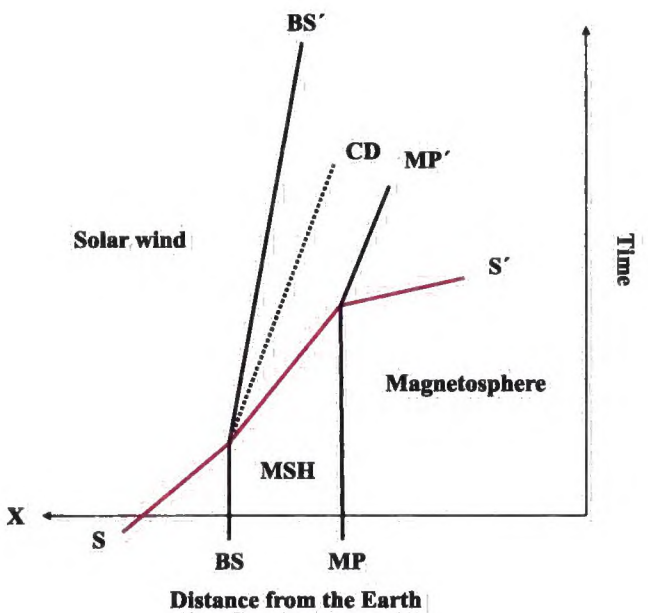

Figure 2.16: Schematic plot of interaction between the fast shock (FS) and the bow shock (BS) and magnetopause (MP). The X axis depicts distance from the Earth (Sun–Earth line) and the Y axis depicts time. The perpendicular lines show initial situation of BS and MP. The oblique lines show the earthward motion (compressions of BS and MP and propagation of FS/disturbance into the magnetosphere) of the structures. MSH ≡ magnetosheath. CD ≡ contact discontinuity. S or S' ≡ shock. Adapted from Yan and Lee (1996).

Interplanetary shocks represent structures which can propagate in the solar wind, into the planetary magnetospheres and interact with them (Figure 2.16), causing their compressions/expansions and modifying magnetopauses and tail currents (Farrugia et al., 1989). On the ground, these processes are related to phenomena called sudden commencements/sudden impulses (Keika et al., 2008). Such correlation to interplanetary shocks impinging on the Earth's magnetosphere have been reported in many papers (e.g., Tsu-

rutani et al. (1995); Gonzalez et al. (1999)). Geomagnetic activity can be described by Dst and Kp indexes. The hourly Dst index (Sugiura and Wilson, 1964) is obtained from magnetometer stations near the equator and the Kp index (Bartels et al., 1939) is obtained from a number of magnetometer stations at mid-latitudes.

Comparing the fast forward shocks to other types of interplanetary shocks near the Earth, they are more significant because of their higher occurrence in the solar wind and their intense compression of the Earth's magnetosphere. These types of shocks propagate in plasma frame with a speed about 50–200 km/s (Berdichevsky et al., 2000).

The shock modification inside the magnetosheath has been studied by several authors using gas dynamic and magnetohydrodynamic modeling or using the Rankine–Hugoniot conditions, such as Spreiter and Stahara (1994), Grib et al. (1979), Grib (1982), and Zhuang et al. (1981). We already mentioned magnetohydrodynamic modeling of the interaction between the Earth's bow shock and interplanetary shocks or rotational discontinuities performed by Yan and Lee (1996). According to them, after interaction of fast forward shocks with the bow shock, a fast shock, a slow expansion wave, a slow shock, and a contact discontinuity can be generated downstream of the bow shock. The bow shock can be modified and moved earthward.

While considering planar FFS in the solar wind, the IP shock front may be curved and delayed near the flank magnetopause, as shown by Koval et al. (2005, 2006a,b). The propagation of FFS along a normal direction in the solar wind and magnetosheath have been also studied by Villante et al. (2004). These authors found a time delay of about 5 minutes from the bow shock to the ground for almost radially propagating structures. They also estimated the magnetosheath speed of the shock to be $1/3 - 1/4$ of the shock speed in the solar wind.

As bow shock is the fast reverse shock, the interaction of the FFS with the bow shock (Šafránková et al., 2007a) is a problem of the interaction of two shocks. A comparison of the spacecraft observations with 3D MHD numerical model (Samsonov et al., 2006) was performed by Šafránková et al. (2007a). Interaction of the FFS with the bow shock creates a train of discontinuities behind fast forward shock that moves with a similar speed in the magnetosphere (see local 3D MHD simulation results by Samsonov et al. (2006)). In the magnetosheath, such compound discontinuity was described by Šafránková et al. (2007b) and its speed determined in a case study by Prech et al. (2008).

The analysis of Rankine-Hugoniot conditions performed by Grib et al. (1979) shows that interactions of FFS with the magnetopause result in a rarefaction waves which are

propagating toward the bow shock (Zhuang et al., 1981).

According to global numerical MHD simulations performed by Guo et al. (2005), the shock orientation plays an important role in determining the IP shock-magnetosphere interaction effects. They compared IP shocks with the same solar wind dynamic pressure and IMF B_z but with the different direction of propagation. The first orientation was parallel and the second oblique to the Sun-Earth line. In the first case, for observation at the geostationary orbit at local noon, the front of the magnetic field compression lasted about 1 min. The ramp may be split into two parts with a small decrease in between. A similar jump existed in the oblique case but lasted 5 minutes.

According to Tamao (1964), isotropic compressional hydromagnetic waves are generated at the magnetopause, starting at a single point of the first contact but later, the source is moving with the IP shock/magnetopause interaction region. The waves are propagating inward through the magnetosphere and may convert to other wave modes. In the case study, Wilken et al. (1982) estimated propagation velocities to be about 600 km/s in the radial direction (from the geostationary orbit to the ground) and about 910 km/s in the azimuthal direction in the geostationary orbit plane. Nopper et al. (1982) estimated impulse disturbance speed about 1500 km/s within the geostationary orbit.

Chapter 3

The aims of the thesis

Practically from the beginning of astronomy scholars studied also our closest star, the Sun. In the 19th century, scientists also began to research phenomena like cometary tails, which were always directed from the Sun. Hence came first ideas about solar wind.

In his model Parker (Parker, 1958) supposed that the solar wind is stationary. Therefore, there are no changes in the plasma density and solar wind speed. Accuracy of this model could be only verified by the first observation of the solar wind at the beginning of the 1960th years from Russian and US satellites, as Luna 2, Luna 3, Mariner 2, Mariner 4, and others. However, observations show that the solar wind is not stationary. Solar wind speed is variable in different parts of the interplanetary space. A faster solar wind in some regions drags magnetic lines faster than in neighboring regions. On their boundaries solar wind and magnetic lines are compressed. In special situations, there can be created interplanetary shocks.

The aims of this thesis are to study different types of interplanetary shocks in the solar wind, their propagation into the Earth's magnetosphere, and their modifications. We have chosen fast forward shocks because of their higher occurrence in the solar wind and as precursors of the arrival of large solar wind structures from the Sun, such as CMEs and CIRs.

Our study is based on observation and we preferentially chose the named structures from the Kasper (2005) and SOHO (2007) databases. To study these processes we utilized all available relevant data from ACE, Wind, Interball–1, Magion–4, IMP–8, Geotail, Cluster, Double Star TC1, geostationary GOES and LANL satellites, Polar, and, in some cases, SOHO and Genesis. During our analysis, we assumed FFS as planar shocks with the constant speed in the solar wind. We calculated shock normals using different methods (RH or 4 S/C), and from the multi-spacecraft timing we calculated disturbance speeds in

the Earth's magnetosphere. We compared the results with existing MHD simulations and also run own simulation aimed to the comparison with the real events.

In the thesis, we discuss following topics:

- Interaction of the interplanetary fast forward shocks with the Earth's bow shock.
- Statistical analysis of the fast forward shock speed in different parts of the Earth's magnetosphere, including a short statistical study to discuss the fast forward shock properties and dependencies on the different solar wind parameters.
- Detailed investigation of two close interplanetary shocks propagating through the magnetosphere.
- Comparison of these observations with results of MHD modeling of the same events.
- Short comparison of two MHD simulation tool results modeling the event.

Chapter 4

Data set

Real measurements are important for the study of interplanetary shocks and their interactions with the Earth's bow shock. Data from the solar wind and the Earth's magnetosphere can be obtained from different satellites. Because of the global character of investigated phenomena, unpredictable time of occurrence and peculiarities in various spacecraft operations and orbits, as much as possible spacecraft/observations points are required for our study. In the following parts there are described satellites that provided data for our analysis and their instruments and orbits.

4.1 Satellite Wind

Satellite WIND (Lepping et al., 1995; Ogilvie et al., 1995; Lin et al., 1995) was launched on November 1, 1994 and has become the first of two NASA spacecraft in the Global Geospace Science initiative and part of the ISTP Project, web-site: http://www-istp.gsfc.nasa.gov/istp/wind. WIND was positioned, Figure 4.1, in a sunward, multiple double-lunar swing orbit with a maximum apogee of 250Re near to the Earth-Sun L1 point. It was followed by series of so/called *petal* orbits, as seen in Figure 4.2. Later, Wind completed several long-term excursions far ahead and behind the Earth on its solar orbit. Nowadays, Wind sits near the Lagrangian L1 point.

8 instruments are on board: 3DP, MFI, SWE, TGRS, WAVES, EPACT, SMSm, KONUS. 3-D Plasma and Energetic Particle experiment (3DP) is designed to measure the full three-dimensional distribution of suprathermal electrons and ions at energies from a few eV to over several hundred keV and provides date with good time resolution.

Magnetic Field Investigation (MFI) is based on the magnetometers previously developed for the Voyager, ISPM, GIOTTO, and Mars Observer missions. The basic config-

uration consists of dual, wide range (0.001 to 65536 nT) triaxial fluxgate magnetometers mounted remote from the spacecraft body on a deployable boom.

Solar Wind Experiment (SWE) includes a sensor especially configured to measure the solar wind parameters as well as flux of a narrow beam of electrons which travel outward from the Sun closely aligned with the interplanetary magnetic field.

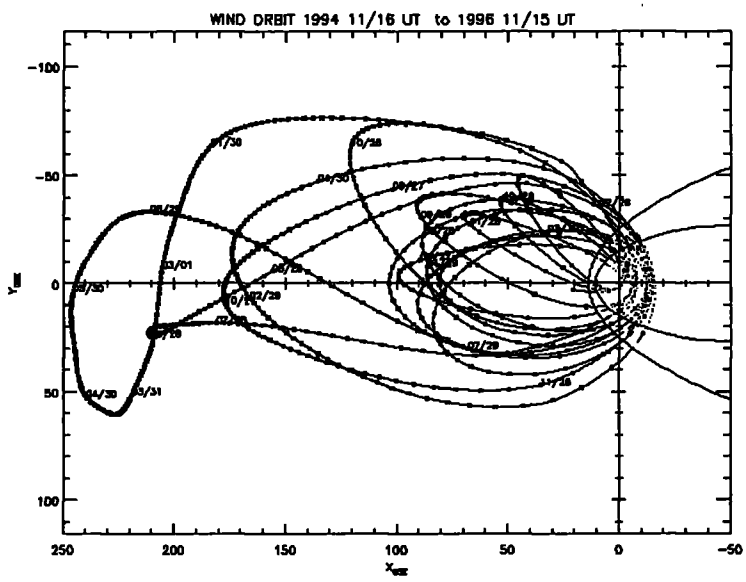

Figure 4.1: Orbit development of satellite Wind in years 1994 till 1996. Direction to the Sun is from the right to the left.

Data time resolution of magnetic field measurements *MFI* is: 3 seconds, 1 minute and hour averages. Data time resolution of plasma measurements *SWE* is cca. 100 seconds, and 3 seconds for the 3DP instrument.

4.2 Satellite Interball-1

The Interball project (Klimov et al., 1997; Nozdrachev et al., 1998; Safrankova et al., 1997) was the solar-terrestrial programme devoted to study various plasma processes in the solar wind and in the Earth magnetosphere by the system of spacecraft consisting of two pairs (satellite-subsatellite). These two pairs of spacecraft moved along different orbits.

Interball-1 and Magion-4 were launched in August 3, 1995 on an elongated elliptical orbit with inclination of $62,8°$, apogee of 200000 km $\simeq$ 31 R_E and orbital period of 92 hours. The second pair of spacecraft (Interball-2, Magion-5) was launched on August 29, 1996 into an ecliptic orbit with apogee 20000 km and inclination of 65°.

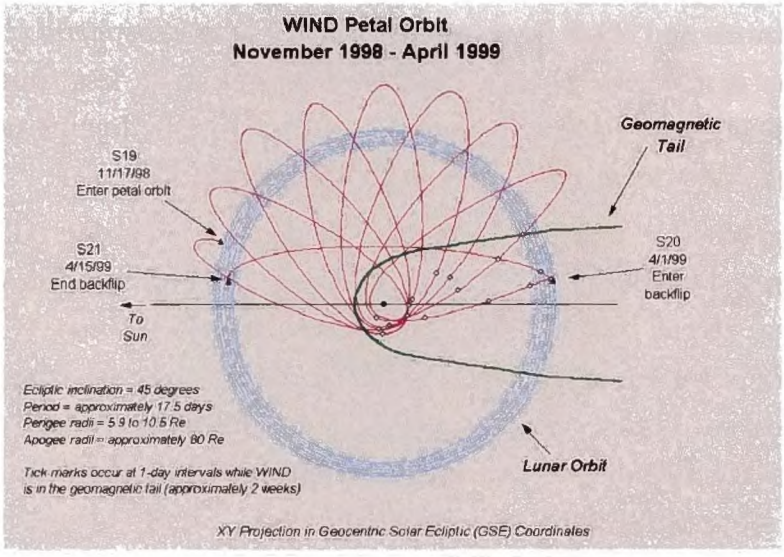

Figure 4.2: Satellite Wind in orbit petal. Blue line means orbit of the Moon, red lines means orbit of satellite Wind. Figure is in XY plane in GSE coordinates.

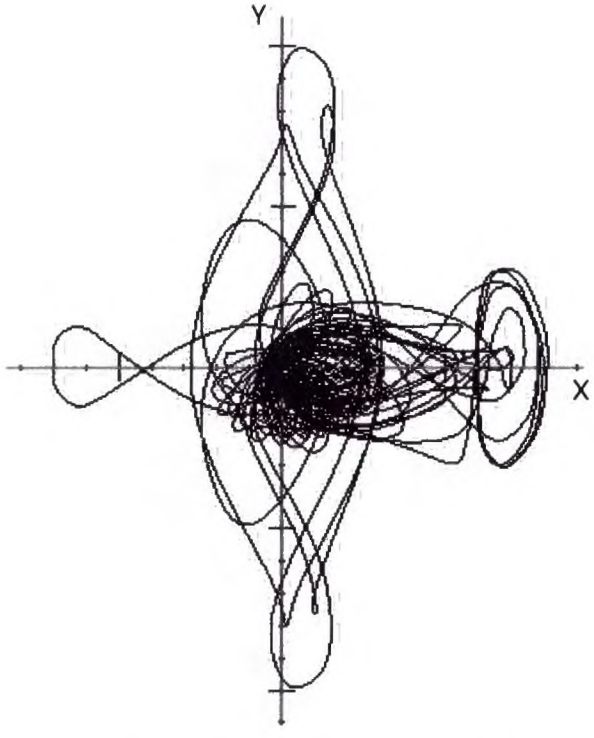

Figure 4.3: Plot of the satellite Wind orbit from 1994 till 2004 is in XY plane in GSE coordinates. Sun is on the right side.

The scientific aim was to study active plasma processes within the tail where powerful currents, substorms and other large-scale non-linear magnetospheric phenomena originate. The separation in the pair of satellites was operated from less than 100 km, allowing to study the small-scale wave and plasma structures at the boundaries, up to about 1-2 Earth's radii to study large plasma structures in the tail.

Onboard Interball-1, magnetic field measurements are carried out by the FM-3I and MIF instruments. FM-3I consisted of two fluxgate magnetometers M1 and M2 covering two different ranges: 200 nT and 1000 nT. The M2 instrument was mostly used to perform the attitude control of the Interball-1 spacecraft. M1 magnetometer data were transmitted at rates of 0.125-16 vectors/sec depending on the instrument operating mode. The magnetic field data from the M2 magnetometer were transmitted at the rate 1 vectors per 6 sec. M1 measured range was 200 nT and sampling rate is 1/8 to 16 measurements per second. M2 measured range was 1000 nT and sampling rate 1/6 measurement per second. The MIF magnetometer had the measured range 0.3-37.5 nT, frequency range 0-2 Hz and sampling rate from 1/4 to 8 measurements per second. The FM-3 M2 magnetometer failed in February 1996, FM-3 M1 and MIF continued working till the end of mission in October 2000.

The VDP instrument was designed for determination of the integral flux vector or integral energetic spectrum over the range 0.2 - 2.4 keV of solar wind or magnetosheath plasma. The instrument included 6 identical Faraday cups. The maximum data rate was 16 samples per second. The VDP instrument began to operate August 14, 1995.

The ELECTRON experiment performed 3-D measurements of the plasma electrons in the energy range from 10 eV to 26 keV, with a good angular resolution. The spectrometer consisted of a quadri-spherical analyzer associated with microchannel plates. Similar to the VDP instrument, it did not operate through the radiation belts.

The study of energetic particle acceleration and transport within the magnetosphere and on its boundaries was the main goal of the DOK-2 experiment. Two particle spectrometers: DOK-2 and its small version DOK-2S were installed on the main satellite and the small subsatellite. DOK-2 used two pairs of energetic particle telescopes. Each telescope had a single, passively cooled, totally depleted, surface-barrier silicon detector. One detector of each pair (1e, 2e) was 0.3 mm thick. A thin foil in front of the detector absorbed protons with energies $E < 400$ keV so this detector measured electron spectrum in the 20 - 420 keV range. The second detector (1p, 2p) of 0.15 mm thickness was supplied with a broom magnet, deflecting electrons up to 1500 keV. It measured the spectrum of ions

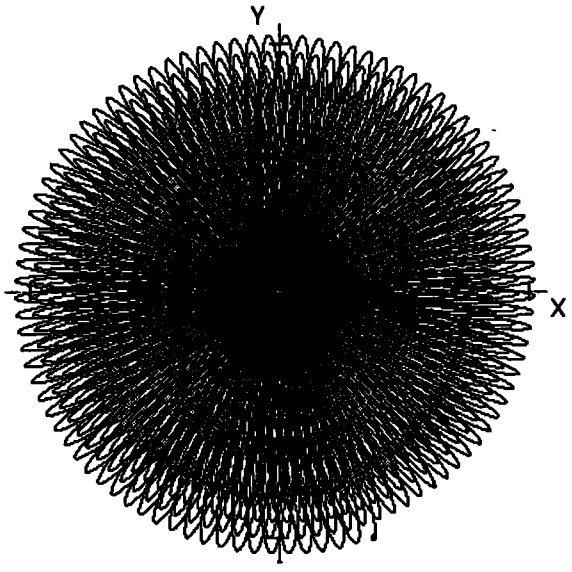

Figure 4.4: Orbit development of the Interball-1 satellite in the XY plane in GSE coordinates. Direction to the Sun is from the right to the left, according to description in X axis.

(protons) in the 20-850 keV range.

4.3 Satellite Magion-4

Magion is a name of the serial of small MAGnetospheric and IONospheric satellites.

Spacecraft	Launch date	Weight	Perigee	Apogee
Magion 1	24.10.1978	15 kg	406 km	768 km
Magion 2	28.09.1989	52 kg	500 km	2500 km
Magion 3	18.12.1991	52 kg	438 km	3070 km
Magion 4	03.08.1995	59 kg	1 000 km	198 000 km
Magion 5	29.08.1996	64 kg	1 000 km	20 000 km

Table 4.1: The Magion satellites development, the weight of each satellites and orbits.

Magion-4 was subsatellite of Interball-1. It was launched on August 3, 1995 and worked till September 1997 on the same orbit as Interball-1. Magion-4 had 10 instruments onboard, from which important to us are data from the instrument VDP-S - detector of plasma flow, MPS/SPS - spectrometer of ions and electrons at range 200 eV - 25 keV and SGR - magnetometer.

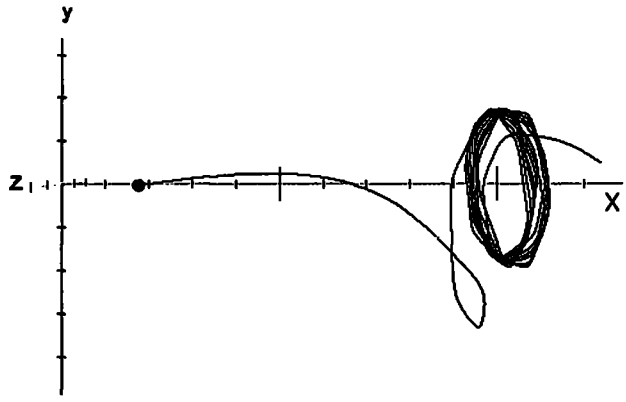

Figure 4.5: Orbit development of the ACE satellite in XY plane in GSE coordinates, from 26.8.1997 till 1.5.2004. Direction to the Sun is from the right to the left, according to description in the X axis.

4.4 Satellite ACE

Advanced Composition Explorer (ACE) (Smith et al., 1998; McComas et al., 1998a) is designed to collect observations of particles of solar, interplanetary, interstellar, and galactic origins, spanning the energy range from that of keV solar wind ions to galactic cosmic ray nuclei up to 600 MeV/nucleon. ACE was launched August 25, 1997. The orbit of the satellite was planed so that the satellite occupies a halo orbit around the L1 Earth-Sun libration point.

The ACE satellite has nine instruments onboard. It provides data measurement of the magnetic field *(MFI)* and plasma parameters *(SWE)*.

At our disposal, we have data of the magnetic field with time resolution of 16 seconds or 5 minutes, and plasma parameters with time resolution of 64 seconds, 5 minutes, or 1 hour.

4.5 Satellite Geotail

The primary objective of satellite Geotail (Kokubun et al., 1994; Mukai et al., 1994) is to study the dynamics of the Earth's magnetotail over a wide range of distances, extending from the near-Earth region (8 Earth radii from the Earth) to the distant tail (about 200 Re from the Earth). Geotail was launched on July 24, 1992.

The Geotail mission was divided into two phases. During the two-year initial phase, the orbit apogee was kept on the nightside of the Earth utilizing the Moon's gravity in a

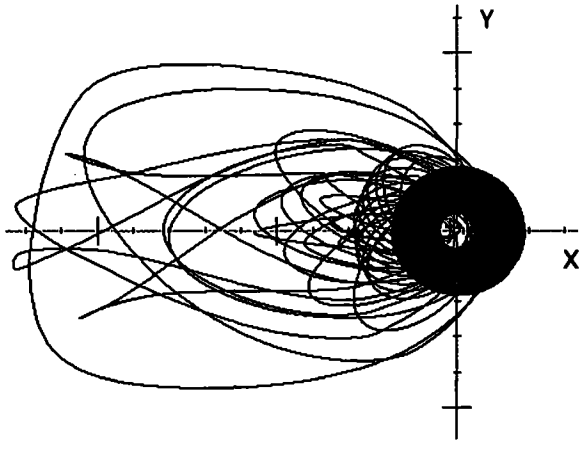

Figure 4.6: Orbit development of the Geotail satellite in the XY plane in GSE coordinates, from 27.7.1992 till 24.5.2004. Direction to the Sun is from the right to the left, according to description in the X axis.

series of double-lunar swing-by maneuvers that resulted in the spacecraft spending most of its time in the distant magnetotail (maximum apogee about 200 Earth radii) with a period varying from one to four months. Then, starting in November 1994, there were a series of maneuvers to bring the spacecraft into its near-Earth orbit. This transition orbit lasted about three months with the apogee varying from 50 RE to 30 RE. The second phase is dedicated to the study of near-Earth magnetospheric processes.

Geotail has seven instruments, such as Comprehensive Plasma Investigation *(CPI)*, Low-Energy Particles *(LEP)*, Magnetic Field Experiment *(MGF)*. At our disposal, we have data of the magnetic field with the time resolution 3 seconds, low energy particles with time resolution 12 seconds, and plasma instruments with time resolution of 45 seconds.

4.6 Satellite IMP-8

IMP-8 was launched on October 26, 1973 to measure the magnetic fields, plasmas, and energetic charged particles of the Earth's magnetotail and magnetosheath and of the near-Earth solar wind. IMP-8, the last of ten IMP satellites, continued to operate in near-circular, 35 Earth Radii, 12-day orbit for almost 3 decades. It's the longest working satellite and it supplied high-quality data till the middle of the year 2003.

Available data of the magnetic field *(MAG)* (http://nssdcftp.gsfc.nasa.gov/spacecraft_data/imp/imp8/mag/ (A. Szabo and R. P. Lepping, NASA GSFC)) had the time reso-

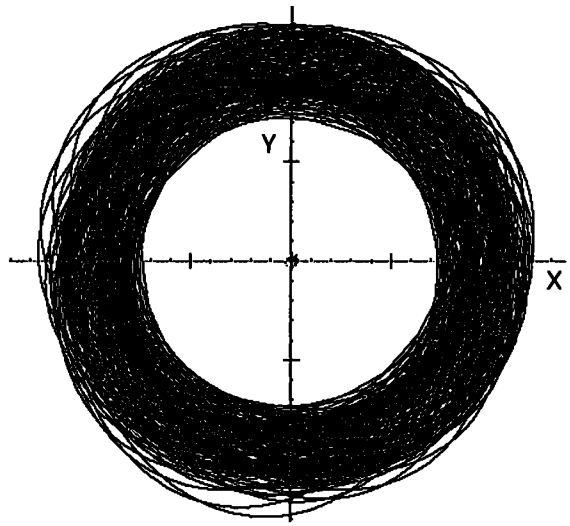

Figure 4.7: Orbit development of the IMP-8 satellite in the XY plane in GSE coordinates, from 30.10.1973 till 1.1.2004. Direction to the Sun is from the right to the left, according to description in the X axis.

lution of 15.36 seconds and plasma parameters *(PLA)* (Bellomo and Mavretic, 1978) had the time resolution of 1 minute.

4.7 Satellite SOHO

Satellite SOHO (Ipavich et al., 1998), the Solar and Heliospheric Observatory, is a project of an international cooperation between ESA and NASA to study the Sun, from its deep core to the outer corona, and the solar wind. SOHO was launched on December 2, 1995.

SOHO occupies a halo orbit at the Earth-Sun L1 Lagrangian point to obtain uninterrupted sunlight. SOHO has twelve instruments. Figure 2.2c was made by its Large Angle Spectroscopic Coronagraph *(LASCO)*.

We can use for our studies only data from the instrument *CELIAS/PM* (Charge, Element, and Isotope Analysis System-Proton Monitor) because there is no instrument which measures interplanetary magnetic field onboard.

4.8 Project Cluster

Four Cluster (Balogh et al., 1997; Reme et al., 1997) spacecraft were launched on August 9, 2000. The aim of this fleet of satellites is to study small-scale structures in the magnetosphere and its environment in three dimensions. The four Cluster spacecraft create a

tetrahedral formation in near-polar orbits. Relative distances between the satellites were varied from several km to several Earth radii. The tetrahedral formation is fundamental for making three-dimensional measurements and for determining the curl of vectorial quantities such as the magnetic field.

Four Cluster spacecraft carry identical sets of 11 scientific instruments. We used Cluster Ion Spectrometry *(CIS)*, Fluxgate Magnetometer *(FGM)*, or Spatio-Temporal Analysis of Magnetic Field Fluctuations *(STAFF)* data.

4.9 Satellite Polar

The Polar satellite (Russell et al., 1995; Harvey et al., 1995) was launched on February 24, 1996 to observe the polar magnetosphere. It provides multi-wavelength imaging of the aurora, measuring plasma entry into the polar magnetosphere and geomagnetic tail, the flow of plasma into the ionosphere and from the ionosphere, and the deposition of particle energy in the ionosphere and upper atmosphere.

Polar has eleven instruments: Plasma Waves Investigation *(PWI)*, Magnetic Fields Experiment *(MFE)*, Toroidal Imaging Mass-Angle Spectrograph *(TIMAS)*, Electric Fields Investigation *(EFI)*, Thermal Ion Dynamics Experiment *(TIDE)*, Ultraviolet Imager *(UVI)*, Visible Imaging System *(VIS)*, Polar Ionospheric X-Ray Imaging Experiment *(PIXIE)*, Charge and Mass Magnetospheric Ion Composition Experiment *(CAMMICE)*, Comprehensive Energetic-Particle Pitch-Angle Distribution - Source/Loss Cone Energetic Particle Spectrometer *(CEPPAD/SEPS)*, and Hot Plasma Analyzer *(HYDRA)*.

4.10 Project GOES

The Geostationary Operational Environmental Satellite (or GOES) program (Singer et al., 1996) is focused on observation of the weather. Satellites from this program are designed to operate in geostationary orbit, 35,790 km (22,240 statute miles) above the Earth, thereby remaining stationary. The first satellite GOES-1 was launched on October 16, 1975. In our studies we used data (measurement of magnetic field) from satellites: GOES-8 (launched on April 13, 1994), GOES-9 (launched on May 23, 1995), GOES-10 (launched on April 25, 1997), GOES-11 (launched on May 3, 2000), and GOES-12 (launched on July 23, 2001).

There are two instruments Triaxial Fluxgate Magnetometer *(MAG)* and Energetic Particle Sensor *(EPX)*. Letter X means a number of the satellite. We used magnetic data to

compare magnetic field inside the Earth's magnetosphere with solar wind data. Regularly data from 2 satellites at two fixed longitudes above the America continent are available.

4.11 Project Double Star

Double Star (Cornilleau-Wehrlin et al., 2005; Carr et al., 2006) involves two satellites operated by the China National Space Administration (CNSA). The two spacecraft are called TC-1 and TC-2, where TC means *Tan Ce*, in English *explorer*. The Equatorial spacecraft (TC-1) was launched into an elliptical orbit inclined at 28.5 to the equator on 29 December 2003 and finished its mission in Septermber 2007. The orbit enabled to investigate the Earth's huge magnetic tail, the region where particles are accelerated towards the planet's magnetic poles by a process known as reconnection. The polar satellite (TC-2) was launched 25 July 2004 into a polar orbit. The main purpose of observations is to concentrate on the processes over the magnetic poles and the development of auroras.

The European participation in the Double Star project is the inclusion of eight instruments, seven of which are identical to the instruments on the Cluster satellites. Equatorial Double Star (TC1) had these instruments on board: Active Spacecraft Potential Control *(ASPOC)*, Fluxgate Magnetometer *(FGM)*, Plasma Electron and Current Experiment *(PEACE)*, Hot Ion Analyzer *(HIA)*, Part of Spatio-Temporal Analysis of Field Fluctuations *(STAFF)* + Digital Wave Processor *(DWP)*, High Energy Electron Detector *(HEED)*, High Energy Proton Detector *(HEPD)*, and Heavy Ion detector *(HID)*.

Polar Double Star (TC2) has these instruments on board: Neutral Atom Imager *(NUADU)*, Fluxgate Magnetometer *(FGM)*, Plasma Electron and Current Experiment *(PEACE)*, Low Energy Ion Detector *(LEID)*, Low Frequency Electromagnetic Wave Detector *(LFEW)*, High Energy Electron Detector *(HEED)*, High Energy Proton Detector *(HEPD)*, and Heavy Ion Detector *(HID)*.

4.12 Other related satellites

For our studies, we sometimes could use additional satellites, such as Genesis - interplanatary dust monitor placed for a limited time to the L1 point. Genesis Solar Wind Plasma Experiment has 2.5 minute averaged data. It is too inaccurate for our studies, however, we can use this data for verification or comparison. Equator-S was designed to study the Earth's equatorial magnetosphere out to distances of 67000 km but provided data only few months in 1998. LANL geosynchronous satellites contain magnetospheric

plasma analyzer *(MPA)* measurements and synchronous orbit particle analyzer *(SOPA)* and complete the GOES geosynchronous observations.

4.13 Data sources

To investigate interaction of interplanetary shocks with the Earth's magnetosphere, we use simultaneous data from different satellites. Onboard instruments and their time resolution are summarized in Table 4.2.

In our study, we used a set of fast forward shocks observed by Wind and SOHO (Kasper, 2005; SOHO, 2007, databases) to show some properties of their propagation in the magnetosphere. The analysis utilizes data from simultaneous observations of interplanetary shocks from available satellites in the solar wind and in the Earth's magnetosphere. The satellites data were obtained through the CDAWeb service (http://cdaweb.gsfc.nasa.gov/sp_phys/) project-dedicated archives (Cluster Active Archive http://caa.estec.esa.int/, DARTS http://www.darts.isas.ac.jp/stp/geotail/, CNES-SADS http://sads.cnes.fr:8010/).

4.14 Data processing

To processing and data visualization, we have used programming language *IDL - Interactive Data Language*, see *http://www.ittvis.com/idl/*. Further, I have used program *JOB*, which enables a common access to satellite data maintained in the Department of Surface and Plasma Science. It is also written in *IDL*. The main authors are Doc. RNDr. Lubomír Přech, Dr. and Doc. RNDr. Ondřej Santolík, Dr.

Satellite	Instrument	Time Resolution [s]
ACE	*Magnetic Field (MFI)*	16
	Parameters of Plasma (SWE)	64
Wind	*Magnetic Field Investigation (MFI)*	3
	Solar Wind Experiment (SWE)	100
	3D Plasma Analyzer (3DP PESA Low)	3
Interball–1	*Magnetometers (MIF/FM3)*	6
	Magnetosheath Ion Flux (VDP)	1
IMP–8	*Magnetometer (MAG)*	15
	Parameters of Plasma (PLA)	60
Geotail	*Magnetic Field (MGF)*	3
	Energetic Particles (LEP)	12
	Comprehensive Plasma Instrument (CPI)	50
GOES	*Magnetometer (MAG)*	60, 0.512
Polar	*Magnetic Fields Experiment (MFE)*	55, 6
	Electric Field Instrument (EFI)	6
Cluster	*Magnetic Field Investigation (FGM)*	4
	Ion Spectrometry Experiment (CIS)	4
Genesis	*Genesis Ion Monitor (GIM)*	150
SOHO	*Celias / Proton Monitor (PM)*	30
Double Star	*Flux Gate Magnetometer (FGM)*	4

Table 4.2: Table summarizes satellites, instruments, and their available time resolutions used in this study.

Chapter 5

Fast forward shocks

For the study of properties of fast forward shocks, we selected suitable events from the Wind interplanetary shock database by Kasper (2005) and the SOHO (2007) shock database. For verifying and comparison, we calculated shock parameters, such as shock normals, and shock speeds using 4 S/C and Rankine–Hugoniot methods.

In comparison to other IPS, fast forward shocks are stronger and have higher occurrence in the solar wind and cause more intense compression of the Earth's magnetosphere, so they are preferential subjects of our study. The fast forward shocks are usually connected with fast stream interfaces of corotating interaction regions or are precursors of large and fast coronal ejecta - flares and magnetic clouds. These types of shocks propagate in plasma frame with a speed about 50–200 km/s (Berdichevsky et al., 2000).

5.1 Interaction of the IP shock with both the bow shock and magnetopause

In the paper of Šafránková et al. (2007a,b), we investigated the evolution of IP shocks through the magnetospheric boundaries in the magnetosheath. We analyzed several observations of IP shocks in the magnetosheath and compared them to results of a local MHD model (Samsonov et al., 2006) and discussed global features of the IP shock-bow shock-magnetopause interaction as well as the structure of the IP shock front. From our detailed analysis based on the Interball-1 observations, we can concluded that:

1. the IP shock passage into the magnetosheath causes the inward motion of the bow shock as a result of changes of parameters downstream of the IP shock, as predicted also by Rankine-Hugoniot conditions (e.g., Grib et al. (1979); Zhuang et al. (1981));

2. the inward bow shock motion is followed by an opposite motion and a combination of these two displacements creates a bow shock indentation (Šafránková et al., 2007b) that moves along the bow shock surface with the IP shock; it is often identified as two bow shock crossings in observations;

3. the interaction of IP shock and bow shock frequently causes a splitting of the IP shock front into two steps (similarly as in 1-D MHD simulations of Yan and Lee (1996))with an usual time lag of the order of one minute. Furthermore, we note that these two observed discontinuities having very similar velocities are generally consistent with the MHD magnetosheath model of Samsonov et al. (2006).

As an example of this comparison of observations with MHD predictions, we present here one event that was observed on July 28, 1996 by Geotail. In the Samsonov et al. (2006) model, an artificial spacecraft were placed on the Z_{GSM} axis near the bow shock and the predicted profiles of basic parameters are plotted in Figure 5.1a for a run with a standing magnetopause. The run uses an increased spatial resolution (grid spacing is 400 km in this case). The spacecraft would observe the IP shock in the magnetosheath and then it would cross the bow shock because of its inward motion. The modification of the magnetosheath parameters by the reverse shock reflected from the standing magnetopause results in the bow shock outward motion that is recorded as a consecutive bow shock crossing.

The IP shock observations in the magnetosheath is shown in Figure 5.1b. The shock was registered by Wind at 1214 UT. Unfortunately, no other spacecraft was in the solar wind and thus the shock parameter determination is based on the Rankine-Hugoniot relations and the Wind data. However, we note that the predicted time of the shock propagation from Wind to Geotail was 50 min, whereas that observed was 52 min. A good match of these two times suggests that the shock parameters given in Figure 5.1b caption were determined properly. Plasma parameters onboard Geotail were measured by two devices. Since their data on the ion density differ, we are showing both values in Figure 5.1b. Our comparison is only qualitative, thus we do not comment these differences.

IP shock observations in the magnetosheath are characterized by an increase of the ion density and a very small increase of the velocity accomplished with a change of its direction characterized by the cone angle, Θ_v in Figure 5.1b. The IP shock is denoted by the vertical dotted line (labeled 1) in Figure 5.1b. The shock is followed (with a delay $\sim$ 55 s) by another discontinuity denoted by the dashed line (labeled 2) in Figure 5.1b.

The changes of the magnetic field are gradual but the ratio between preshock and postshock magnetic fields is about 1.6, similar to that observed in the solar wind. The

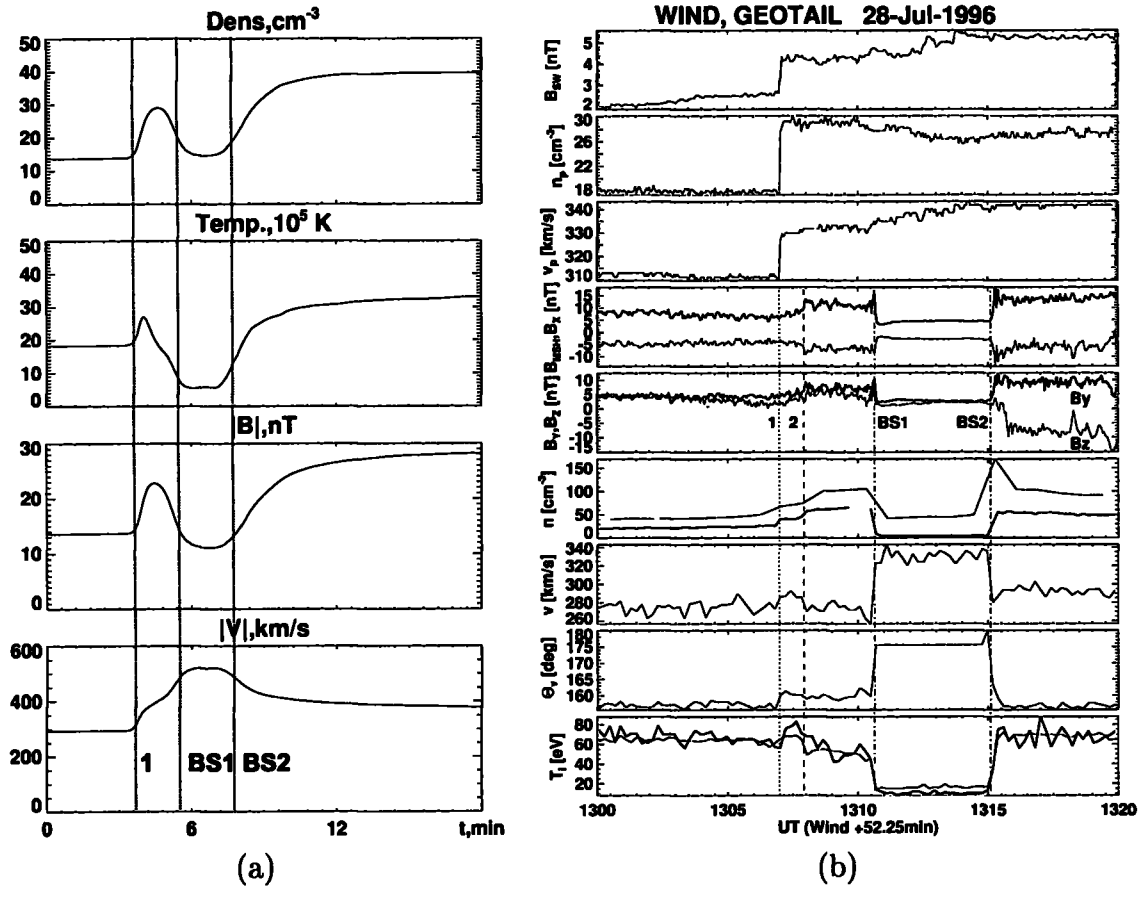

Figure 5.1: (a) Simulated profiles of the density, temperature, magnetic field magnitude, and velocity. The vertical lines denote IP shock (1), bow shock crossings BS1 and BS2. (b) Wind observation of the interplanetary shock on July 28, 1996 (first three panels), together with Geotail observation in the magnetosheath (six lower panels). Panels from top: solar wind magnetic field magnitude B_{SW}, the solar wind density n_p and velocity v_p in GSE coordinates, next two panels showing magnetic field B_{MSH}, B_X, and B_Y, B_Z, density n, velocity v in the magnetosheath, cone angle Θ_v, and ion temperature T. The shock parameters in the solar wind are $v_{sh} = 339$ km/s, $M_A = 2.06$, and $n = [-0.92, -0.06, -0.39]$.

most distinct feature in the Geotail data is short-time excursion ($\sim$ 260 s) into the solar wind that follows the IP shock front with a delay of about 220 s. This feature is similar to the profile in Figure 5.1a. The time delays are a little larger but we would like to note that the analyzed event was characterized by a very low solar wind speed and low Mach number. Consequently, one can expect that the timescales would be larger than those in the model (the shock speed in the numerical simulations was $\sim$ 600 km/s but was $\sim$ 340 km/s in the analyzed case).

5.2 Statistical analysis of the shock speed in the magnetosphere

To study of shock speeds in different locations of the magnetosphere, we analyzed more then 40 interplanetary shock events between years 1995 and 2006. Events were selected with a requirement of the GOES satellites location in the dayside magnetosphere. Disturbance speeds in the Earth's magnetosphere were calculated from timing of satellite observations in the direction of the propagation of the original FFS in the solar wind using the pairs of satellites both located within the magnetosphere. For the calculations, we chose the times of the first signatures of the incoming disturbances. In Table 5.1, it is shown a set of fast forward shocks (from Kasper (2005) and SOHO (2007)), which were a subject of our investigation. The table summarizes calculated parameters: normal vectors, shock speeds, solar wind speeds, compression ratios, values of the cone angle of the normal and upstream total IMF values.

According to our study (Andreeova and Prech, 2007b), we can summarize that the speed of waves in the Earth's magnetosphere are higher than the original shock speed in the solar wind (Figure 5.2a) and slightly differ for different magnetosphere regions: dayside, central part, and nightside. According to Figure 5.2b these disturbance speeds gradually increase from the dayside to the nightside.

The compression ratio, defined as the ratio of downstream and upstream densities, and dynamic pressure are the attributes which describe the shock strength. The dependence of disturbance speeds on the upstream dynamic pressure is displayed in Figure 5.3a. The dependence decreases for smaller values of the dynamic pressure (less than 2.5nPa) and starts to increase with higher values of dynamic pressures. In the case study of 9th November, 2002, we found that the disturbance speeds in the magnetosphere are higher for the case of higher dynamic pressure (in case of higher shock speed in the solar wind).

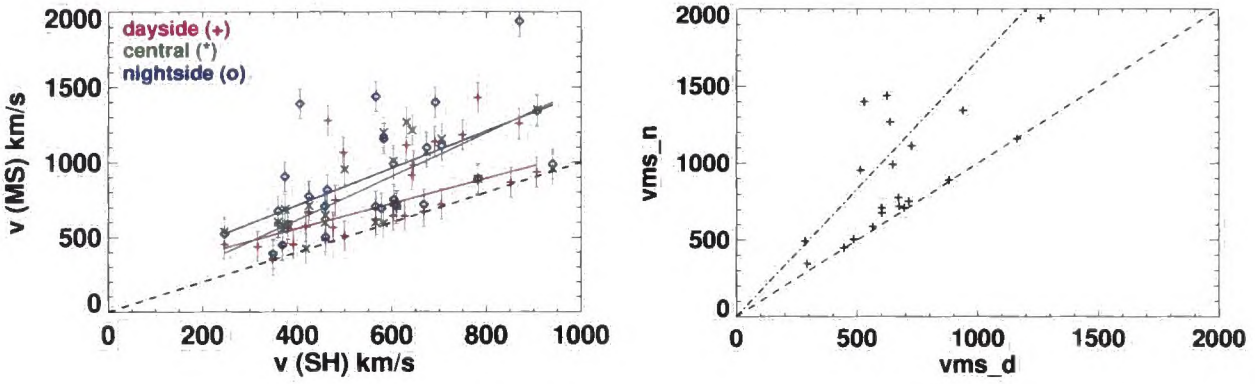

Figure 5.2: (a) Relation of the disturbance speed in the Earth's magnetosphere to the shock speed in the solar wind: blue color denotes dayside values, green trans-terminator (central) values and red color - nightside values. Red, green and blue lines show linear fits of these dependencies. Disturbance speed is higher in the Earth's magnetosphere than in the solar wind and higher in the nightside than in the dayside magnetosphere.(b) Relation of the nightside disturbance speed to the dayside disturbance speed. Dashed line depicts ratio 1:1 and means lower limit. Higher values show that speeds gradually increase from the dayside to the nightside region.

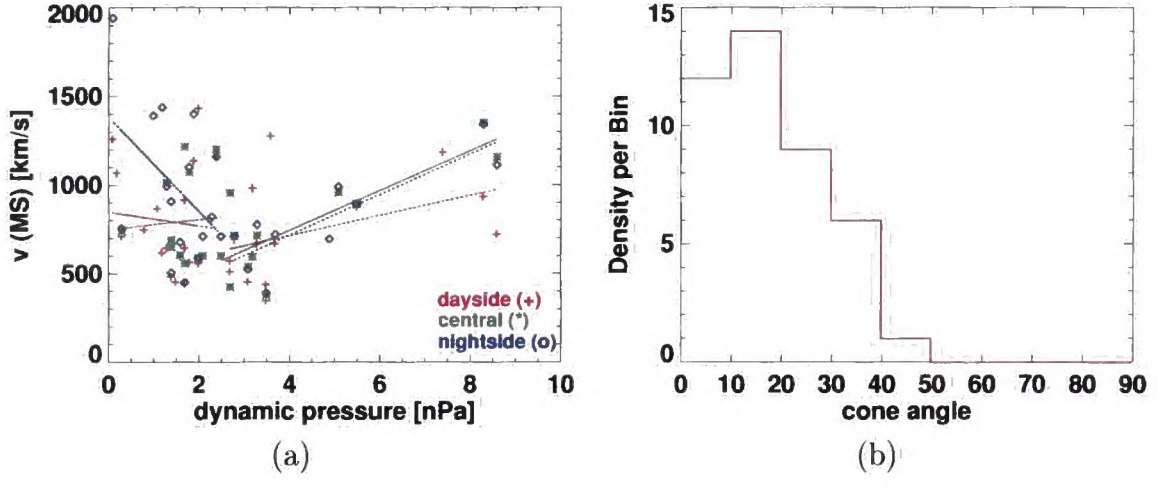

Figure 5.3: (a) Dependence of the disturbance speed on the dynamic pressure upstream of the IP shock. Dashed color lines depict linear fits of these dependencies. (b) Distribution of cone angles of the shock normal (0-90 degrees) for the events in our data set. The cone angle of a shock perpendicular to the Sun-Earth line is 0 degree, the cone angle equal to 90 degrees corresponds to a shock parallel to the Sun-Earth line. Fast forward shocks propagate almost quasi-perpendicular to Sun-Earth line.

2006-01-01	13:26:16	-0.88 0.04 0.47	610	433	1.30	28.3	10.9	695^{G12-Po}	$713^{G12-G10}$	$710^{G10-DS1}$	2.8	6.8
2005-09-11	00:57:55	-0.81 0.58 -0.10	940	850	2.96	36.2	6.9	-	958^{G10-Cl}	990^{Cl-DS1}	5.1	-2.9
2005-09-09	13:32:58	-0.76 -0.62 -0.17	450	340	3.12	40.5	5.3	330^{G12-GE}	$320^{G10-G12}$	490^{Po-DS1}	3.1	-0.6
2005-09-02	13:50:13	0.95 0.19 -0.26	566	530	2.20	18.8	7.5	-	601^{Po-GE}	710^{Po-Cl}	2.1	5.3
2005-08-24	05:35:22	-0.96 -0.11 0.25	578	461	2.57	15.6	10.6	-	-	695^{Cl-DS1}	4.9	4.7
2005-07-10	02:42:28	-0.93 -0.05 0.37	464	354	1.77	22.2	10.5	-	-	819^{Cl-Po}	2.3	-3.4
2005-06-12	06:48:38	-0.90 -0.37 -0.23	374	353	2.40	26.1	2.9	-	690^{DS1-Po}	906^{Cl-Po}	1.4	0.8
2004-11-09	18:25:00	-0.90 0.36 0.25	705	642	2.96	25.8	6.7	$725^{G10-G12}$	1157^{G12-Cl}	1112^{Cl-Po}	8.6	-2.2
2004-11-07	17:59:12	-0.98 -0.16 0.14	750	463	2.11	11.5	19.1	1187^{G10-Cl}	-	-	7.4	16.4
2004-09-13	19:44:52	-0.81 -0.43 0.39	604	330	1.95	35.5	11.2	$714^{G10-G12}$	740^{G12-Po}	754^{Cl-Po}	0.3	-0.6
2004-07-30	20:27:19	-0.91 0.16 0.38	604	440	1.58	24.3	4.4	$648^{G10-G12}$	1012^{G10-Cl}	992^{Cl-GE}	1.3	-1.3
2004-04-12	18:29:43	-0.95 -0.05 0.31	566	439	2.30	18.4	3.7	$622^{G10-G12}$	-	1438^{Cl-GE}	1.2	-0.1
2004-04-10	20:21:28	-0.80 -0.40 -0.44	443	432	2.07	36.6	4.4	601^{G10-Cl}	605^{Cl-Po}	678^{Po-GE}	1.6	2.4
2003-05-30	15:55:13	-0.96 -0.08 0.29	692	625	1.62	17.2	12.0	528^{G12-Cl}	-	1400^{Po-GE}	1.9	10.8
2003-05-29	18:31:08	-0.99 -0.01 0.05	907	693	2.12	8.1	16.7	$938^{G10-G12}$	1352^{G10-Po}	1342^{Cl-GE}	8.3	-14.3
2002-11-26	21:45:43	0.99 0.03 -0.06	782	453	1.53	8.1	10.8	881^{G8-G10}	890^{G10-Po}	892^{Cl-GE}	5.5	2.6
2002-11-09	17:24:49	-0.99 0.15 -0.05	380	344	1.39	8.1	4.5	564^{G8-G10}	589^{G10-Po}	588^{Po-C1}	2.0	2.6
2002-11-09	18:27:49	-0.98 -0.03 -0.20	425	362	2.10	11.5	7.1	671^{MP-G8}	714^{G10-Cl}	776^{Po-Cl}	3.3	3.8
2002-08-18	18:40:44	-0.96 0.06 0.29	673	485	2.72	16.3	2.9	-	1070^{G10-Cl}	1100^{Cl-GE}	1.8	1.4
2002-07-29	13:14:55	-0.95 -0.02 -0.31	460	414	2.80	18.1	4.5	485^{C8-GE}	650^{Po-GE}	505^{G10-Po}	1.4	-0.1
2002-03-20	13:19:40	-0.87 0.16 0.47	870	415	1.46	29.6	13.4	1261^{G8-Po}	-	1940^{G10-G8}	0.1	0.2
2001-11-19	18:15:31	-0.99 0.10 -0.14	628	456	1.95	8.1	6.3	648^{G8-G10}	-	-	1.7	2.6
2001-10-11	16:50:55	-0.99 0.04 0.01	583	411	1.97	8.1	9.2	-	595^{G8-Cl}	-	3.2	2.1
2001-09-25	20:17:16	-0.79 -0.61 0.07	852	457	3.24	37.8	4.1	869^{G8-G10}	-	-	1.1	-0.4
2001-04-18	00:49:46	-0.92 0.35 -0.15	583	392	2.30	22.6	4.4	1162^{G10-Po}	1200^{G8-G10}	1158^{G8-GE}	2.4	-1.3
2000-09-06	17:03:19	0.91 0.39 -0.15	501	380	2.42	24.6	9.2	514^{G8-G10}	954^{Po-G10}	-	2.7	4.7
2000-07-19	15:30:22	-0.97 -0.16 0.16	643	507	1.75	14.1	5.2	917^{G8-GE}	1214^{Po-GE}	-	1.7	-1.9
2000-07-15	14:34:50	-0.86 0.01 0.51	631	-	-	30.7	12.8	1118^{G8-I8}	1267^{G10-Po}	-	-	1.3
2000-07-14	15:33:29	0.99 0.07 -0.14	783	634	-	9.3	4.4	1434^{G8-GE}	-	-	2.0	0.8
2000-06-04	14:45:48	-0.71 0.64 -0.30	481	414	1.11	45.1	4.2	751^{G8-Po}	-	-	0.8	1.5
2000-04-06	16:32:13	-0.98 -0.08 -0.16	647	407	2.26	11.5	7.1	984^{G8-G10}	-	-	3.2	-0.4
1999-12-12	15:54:01	0.99 0.02 0.10	498	374	2.76	5.8	5.0	1071^{G8-G10}	-	-	0.2	-1.3
1999-11-05	20:03:10	-0.93 0.29 -0.22	392	327	1.48	21.6	6.7	456^{G8-G10}	-	-	1.5	-2.4
1999-09-15	20:08:40	-0.83 -0.16 0.53	668	596	1.03	33.9	4.7	674^{G8-GE}	-	721^{Po-IB}	3.7	3.6
1999-06-26	19:30:58	-0.99 0.11 0.13	466	352	1.97	8.1	12.0	1280^{G8-G10}	-	-	3.6	10.7
1999-05-05	15:40:25	-0.92 -0.33 -0.22	476	386	2.04	23.6	3.7	569^{G8-G10}	-	-	1.8	1.2
1998-04-07	16:53:35	-0.91 0.06 -0.42	369	293	2.13	24.5	7.2	445^{G8-G9}	558^{G8-Po}	450^{Po-GE}	1.7	-2.2
1998-01-31	15:53:46	-0.94 0.33 0.30	419	372	1.60	19.9	9.7	577^{G8-G9}	425^{G8-Po}	-	2.7	1.0
1997-11-06	22:19:33	-0.87 0.32 0.39	459	365	2.23	30.1	4.1	-	601^{G8-G9}	710^{G8-GE}	2.5	-1.1
1997-04-30	18:05:44	-0.88 0.30 0.37	349	340	1.63	28.4	4.1	350^{G8-G9}	378^{G8-Po}	390^{Po-GE}	3.5	-2.9
1997-03-20	19:42:23	-0.77 -0.05 0.63	317	304	1.66	39.6	2.7	442^{G8-G9}	-	-	3.5	0.9

Table 5.1: Subset of events from 1997 – 2006 years observed by the SOHO and Wind satellites, the values (in the solar wind) are calculated from the Wind data. In the first two columns, there are the date and time (UT) of the event, next parameters are normal vector, shock speed (v_{sh}), solar wind speed (v_{sw}), compression ratio (C), cone angle of the normal (CONE), upstream total IMF strength (Bt). Disturbance speeds (v(MS)D, v(MS)C and v(MS)N) in the magnetosphere are calculated along the shock normal. The pairs of satellites used for speed calculations are also indicated. D,C,N stands for dayside, central region, and nightside values. Last two columns are the upstream dynamic pressure and IMF Bz component.

Also, a simulation GUMICS-4 showed solar wind dynamic pressure jump similar to the real observation.

Fast forward shocks in our set propagate almost quasiperpendicular, as it shown in Figure 5.3b. Histogram of cone angles shows the distribution of cone angles (angle between the shock front normal and the Sun-Earth line). For perpendicular propagation of FFS, the cone angle is equal zero.

Dependence of the magnetospheric speed v_{MS} to shock speed v_{SH} ratio on the IP shock compression ratio (Andreeova and Prech, 2007b) is within 1 to 1.6 for the most events in the dayside, but it has a much larger spread 1 to 3 in the nightside (Andreeova and Prech, 2007b). Shock speed values seem almost independent to the compression ratio values. The relation of the disturbance/shock speed ratio to the solar wind magnetic field B_z/B relative component seems to be only weak if any, for the dayside observations (Andreeova and Prech, 2007b). It can be positive for the nightside but the spread is high and for most of the observed cases the B_z component was not the main component of the magnetic field vector and we also have a lack of data with the mainly southward IMF. The dependence of the disturbance/shock speed ratio v_{MS}/v_{SH} on the IP shock cone angle shows a weak decreasing tendency but the spread of values was high (Andreeova and Prech, 2007b).

Uncertainties of the shock parameters depend on chosen intervals of upstream and downstream plasma parameters and magnetic field, and time resolution of satellite data. Shock speeds uncertainties in the solar wind are approximately $\pm$ 10 km/s. Disturbance speeds in the Earth's magnetosphere have higher errors about 16 per cents and depend mainly on pure time resolution of given satellites. Simulations and case studies showed that the disturbance front in the tail is greatly distorted. This may explain particularly large scatter of far nightside values, caused by position of satellites in different regions, such as plasma sheet, north/south lobes etc.

5.3 Detailed analysis of events: November 9, 2002

In our study (Andreeova and Prech, 2007a), where we described two events classified as fast forward shocks in a broader detail, we assumed planar interplanetary shocks and expected no change during their propagations in the solar wind. The used shock normal directions may affect our speed calculations.

On November 9th, 2002 (Table 5.2, 5.3), the Wind satellite observed two interplanetary shocks in sequence after 1724 UT and 1827 UT (Andreeova and Prech, 2007a) [A1]. The corresponding components of the shock normal vector were (-0.99, 0.15, -0.05) and (-0.98,

Satellite	X [Re]	Y [Re]	Z [Re]	Arrival Time, UT	Region
SOHO	241.3	-82.0	14.3	1642:36	SW
ACE	229.9	40.9	-17.0	1648:10	SW
Genesis	186.9	-1.5	-1.5	1659:00	SW
Wind	96.4	-29.9	5.5	1724:49	SW
Geotail	18.55	8.13	1.92	1747:50	SW
GOES–8	6.06	1.25	2.32	1750:34	MS
GOES–10	4.62	-4.72	0.06	1750:38	MS
Polar	-5.9	6.0	1.7	1752:50	MS
Cluster SC1	-8.60	13.8	4.43	1753:30	MS
-	11.4	-1.2	0.6	1749:29	MP

Table 5.2: Satellite locations in GSE coordinates and arrival times/compression onsets for the first shock on November 9th, 2002. The last line shows the estimated arrival of the IP shock to the magnetopause. SW — solar wind, MS — magnetosphere.

Satellite	X [Re]	Y [Re]	Z [Re]	Arrival Time, UT	Region
SOHO	241.2	-82.1	14.2	1755:56	SW
ACE	229.9	41.0	-17.0	1754:12	SW
Genesis	186.9	-1.5	-1.5	1807:00	SW
Wind	96.6	-29.9	5.5	1827:49	SW
Geotail	17.76	8.63	1.76	1846:08	SW
GOES–8	5.41	2.8	2.56	1849:07	MS
GOES–I0	5.57	-3.48	0.73	1849:13	MS
Polar	-5.55	5.2	2.2	1850:40	MS
Cluster SC1	-8.62	14.34	3.93	1851:00	MS
-	9.4	0.3	-1.9	1848:29	MP

Table 5.3: Satellite locations in GSE coordinates and arrival times/compression onsets for the second shock on November 9th, 2002. The estimated arrival of the shock to the magnetopause in the last line. SW — solar wind, MS — magnetosphere.

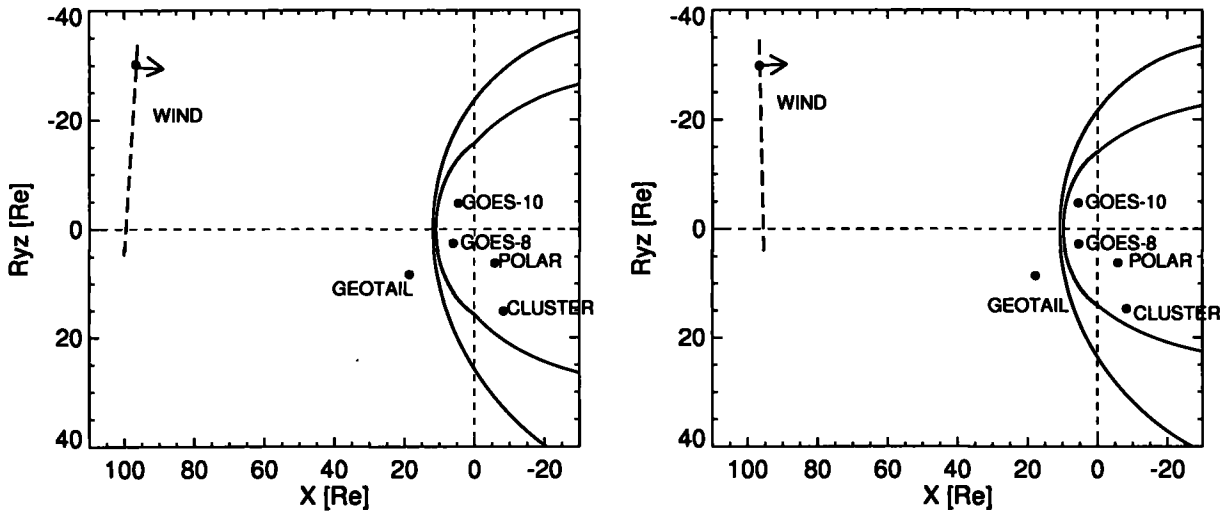

Figure 5.4: (a) November 9th, 2002 event: positions of given satellites for the first part of the event observed by Wind at 1724 UT. The dashed line indicates the interplanetary shock front. The Jeřáb et al. (2005) and Petrinec and Russell (1996) models were used to determine the bow shock and magnetopause positions before the shock arrival. R_{yz} denotes the distance from the X axis, distinguishing the dawn/dusk sides (sign of Y), $R_{yz} = sign(y) \cdot \sqrt{y^2 + z^2}$. (b) November 9th, 2002 event: positions of given satellites for the second part of the event observed by Wind at 1827 UT. R_{yz} has the same meaning as in the left panel.

-0.03, -0.20) in the GSE system. The θ_{Bn} angle was $\sim 43°$ and $70°$, the compression ratio 1.69 and 2.01, respectively.

The IMF was Parker-spiral-like and B_Z was positive both upstream and downstream of these events ($\theta \approx 30 - 60°, \phi \approx 130°$). The situation is depicted in Figure 5.4a,b for the two events. During the given time, the satellites SOHO, ACE, Genesis, and Geotail were also operating in the solar wind, while the geosynchronous GOES–8 and GOES–I0 satellites were in the Earth's dayside magnetosphere. The Cluster spacecraft constellation was situated on the night side in the dusk flank plasma sheet near the magnetopause before the events. It orbited behind the quasiperpendicular part of the bow shock, so we don't expect any foreshock effects there. Polar was also in the nightside magnetosphere closer to the Earth.

The propagation speeds inside the magnetosphere, see Table 5.4, are significantly higher than speeds of fast forward shocks calculated from the Wind satellite in the solar wind (see Figure 5.5a,b). Our results generally agree with estimates by Wilken et al. (1982) and Nopper et al. (1982)(about 600–1500 km/s): our compressional front speeds (about 600–700

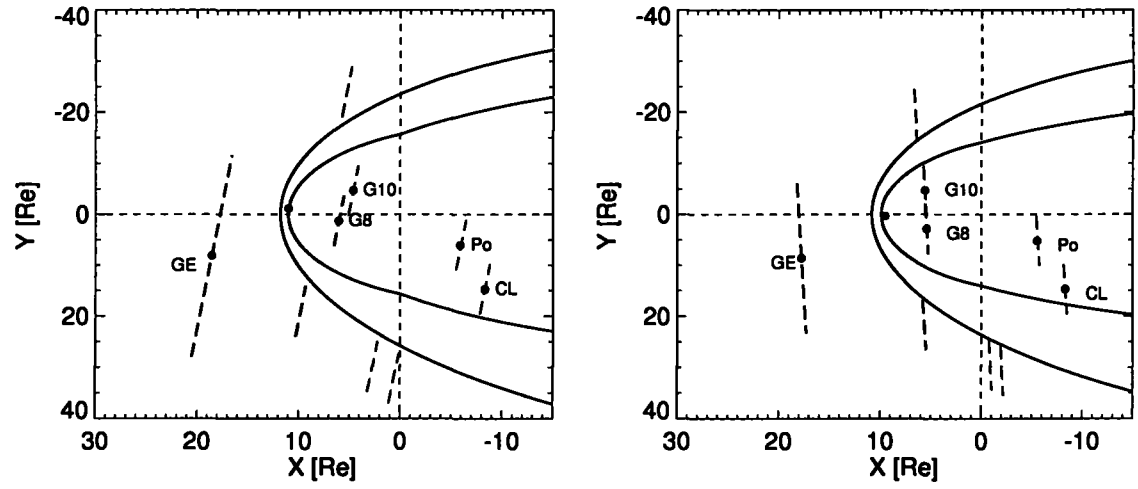

Figure 5.5: (a) Positions of satellites for the first case on November 97h, 2002. Comparison of propagation of disturbance in the Earth's magnetosphere and propagation of original shock in the solar wind. Dashed lines in the magnetosphere depict observations of disturbance. Dashed lines in the solar wind depict the shock, if we assume conservation of the speed and shape of both shocks in the solar wind. (b) Similar situation for the second case.

km/s for the events on November 9th, 2002) are similar to their lower values representing the radial inward motion, but are smaller than their values for the azimuthal/near-geostationary-orbit propagation. The difference may be caused by a diverse state of the magnetosphere and content of plasma (mainly the density of plasma near and outside the geostationary orbit): in the Wilken et al. (1982) case, the preshock magnetopause had been already compressed near to the geosynchronous orbit (subsolar magnetopause at about $R_0 \sim 7.8\ R_E$). Likewise, we got higher speed for the second event when the magnetopause was initially closer to the Earth ($R_0 \sim 9.7\ R_E$) than before the first event ($R_0 \sim 11.7\ R_E$). We also got slightly higher values for the propagation speed to Cluster (significant at least in the second event) that was farther from the Earth than Polar. On the other hand, the higher speed for the second event may be supported by the faster and stronger interplanetary shock actuating along the magnetopause.

There is a notable difference between high- and low-resolution data from GOES. As it is seen from Table 5.1, each satellite GOES can provide two time resolutions. Observed events have duration about 1–5 minutes and so one-minute resolution data are not suitable for our study, but on the other hand, we had a difficult access to the high time resolution data. Detailed comparison of the two shock fronts as registered by the near-Earth spacecraft is provided in Figure 5.6a,b. Both shock fronts at Geotail (in both cases top panels) last about

Date UT	v_n	v_{sh}	v_{MS}	S/C
2002-11-09 1724:49	336	380	590	G8—Cl
			588	G8—Po
2002-11-09 1827:49	351	425	741	G8—Cl
			714	G8—Po

Table 5.4: Two studied fast forward shocks (observed by Wind). Speed units are km/s in the GSE coordinate system. v_n is the upstream solar wind speed along the direction of the shock normal, v_{sh} is the calculated speed of the shock taken from the Kasper (2005) database, v_{MS} denotes the calculated speed of disturbance inside the Earth's magnetosphere determined between two satellites in the last column (G8 ≡ GOES–8, Po ≡ Polar, Cl ≡ Cluster SC1).

10 s. From the high-resolution data, two parts of the fronts on the GOES spacecraft can be distinguished. First, there are slow 3–5 min. long ramps, already reported elsewhere. On top, at the beginning of them, there are very fast step-like fronts taking about one half of the total field compression. They last about 10 s - the same time as the original shock fronts seen in the solar wind by Geotail, and they are mainly caused by the increase of the H_p (northward) component at GOES–8. A small decrease of the magnitude follows after this fast front, similarly as in the simulation case 1 by Guo et al. (2005). The second part of fronts starts by a steep ($\sim$ 30 s) decrease of the H_e (earthward) component and continuing increase of the H_p component. No such double-part structure is seen in the Geotail data, which was upstream the bow shock in the solar wind. The last panel in Figure 5.6 shows magnetic field magnitudes from the Cluster spacecraft. During the first event, the Cluster fleet saw large fluctuations of the magnetic field magnitude. At the moment of the passage of the disturbance after 1753 UT, their frequency increased and the first leading front is quite fast (about 30 s, not resolved at SC2). During the second event (after 1852 UT), a wide ramp is seen by all Cluster spacecraft lasting up to 7 min. (at SC2).

5.4 Temporal conclusion of the November 9, 2002 study

For the selected FFSs, we calculated speeds of corresponding disturbances inside the Earth's magnetosphere between pairs of satellites along the original shock normal direction. Calculated speeds of disturbances were higher in the Earth's magnetosphere than in the solar wind (Andreeova and Prech (2007a)) [A1]. Speeds of the disturbances in the magnetosphere calculated from MP to GOES 8, 10 were for the first event 550-580 km/s

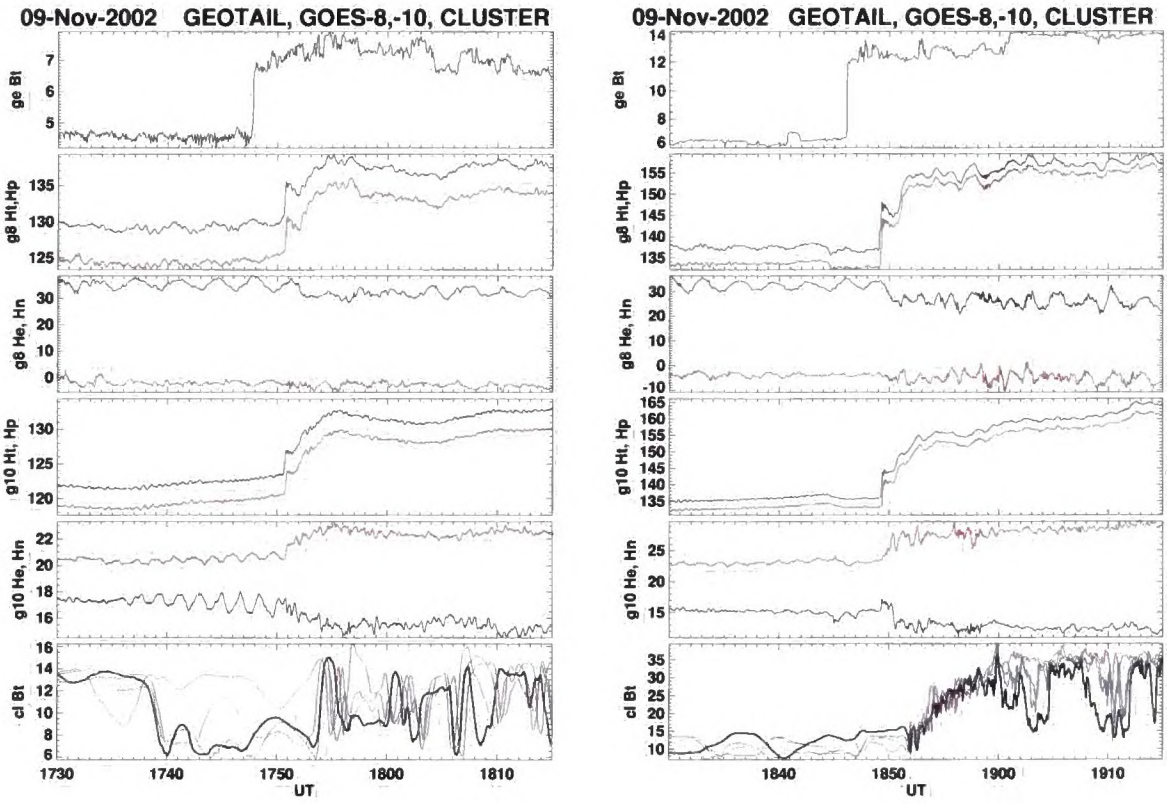

(a) (b)

Figure 5.6: November 9th, 2002 events in detail. (a) Shock at 1750 UT, (b) Shock at 1850 UT. The top panels show the magnitude of IMF as measured by Geotail. The next two panel pairs depict the GOES–8 and GOES–10 high-resolution magnetic field data in local S/C coordinates (H_t magnitude, H_p northward component (in red), H_e earthward component, H_n normal to both H_p and H_e, eastward (in red)). The bottom panels plot the magnitude of magnetic fields measured by Cluster SC1 (black), SC2 (red), SC3 (green), and SC4 (blue). All panels in nT units.

and for the second event 670 km/s, from the dayside to the nightside magnetosphere for the first event 580-590 km/s and for the second event 710-760 km/s, and between Cluster and Polar in the nightside for the first event 590 km/s and for the second event 780 km/s. The speed of the disturbances gradually increased from the dayside to the tail. Speeds were higher in the second case than in the first case. MP was more compressed (R_0 11.7 R_E, 9.7 R_E), so the magnetic field was stronger in the second case - Alfven speed was higher, so the driving IP shock was faster. A significant distortion of the wave front was expected near the flank magnetopause. Our results agree with the conclusions of the Guo et al. (2005) simulation.

For the reported events, GOES measurements revealed very fast fronts of the magnetic field compression (about 10 s), comparable with the interplanetary shock front duration in the solar wind, followed by another slower compression and rotation of the magnetic field.

Russell et al. (1999) explained a similar fast front observation by forming shock–like features due to slowing of compressional waves below the speed of IPS in the denser inner magnetosphere.

Other proposed explanations are:

1. Observation of the original shock in magnetosphere is followed by a reverse going rarefaction wave reflected from the denser plasmasphere (supported by numerical simulations by Guo et al. (2005), Ridley et al. (2006)). On the other hand, Samsonov et al. (2007) supported a reflection of IP shock at ionosphere rather than at plasmasphere.

2. A double part structure is created during the interaction of IPS with the BS/MP system and swept into the magnetosphere. Similar double-step profiles of the density and magnetic field of IPS in the magnetosheath were already reported, e.g., by Samsonov et al. (2006) and Šafránková et al. (2007b), but timing related to different propagation speeds would have to be verified. So far we were not able to find simultaneous multipoint observations in the magnetosheath and at the geostationary orbit with sufficient time resolution.

5.5 Global MHD simulation

To verify our experimental investigation, we used the numerical MHD models. Simulations enable us to discuss the processes inside the magnetosphere and to trace the disturbance propagation and to directly compare observations with predictions.

The first selected GUMICS-4 code (Grand Unified Magnetosphere-Ionosphere Coupling simulation, Janhunen, 1996) is a global MHD simulation coupled with a comprehensive ionospheric model developed and run at Finnish Meteorological Institute. It consists of two parts: MHD magnetospheric part and electrostatic ionospheric part.

The GUMICS-4 global MHD simulation solves the ideal MHD equations to provide the self-consistent temporal and spatial evolutions of the plasma in the magnetosphere and in the solar wind. The simulation box ranges from 32 R_E upstream of the Earth to -224 R_E in the tailward direction and ± 64 R_E in the directions perpendicular to the Sun-Earth line.

Disturbance	Event 1		Event 2	
	Data	GUMICS-4	Data	GUMICS-4
v_{sw}	324	-	348	-
$v_{sh}(SW)$	380	360	425	420
Uncertainty	± 10	± 20	± 10	± 20
$v_{ms}(D)$	550	390	671	425
$v_{ms}(D-N)$	588	500	745	570
$v_{ms}(N)$	588	410	776	780
Uncertainty	± 50	± 85	± 50	± 85

Table 5.5: November 9, 2002 interplanetary shock event: Propagation speeds in the solar wind and in the magnetosphere: v_{sw} is the solar wind speed, v_{sh} is the shock speed in the solar wind, v_{ms} is the disturbance speed in the magnetosphere, where D denotes dayside values, N nightside value and D-N means trans-terminator ("central") values. Speeds determined from observations are shown in the left columns, while those determined from the GUMICS-4 global MHD simulation are shown in the right columns for the two events separately.

The equations are solved in the geocentric solar ecliptic (GSE) coordinates. The finest grid resolution is 1/4 R_E whenever the code detects large spatial gradients.

The second selected tool is the 3D global BATS-R-US tool (Block-Adaptive-Tree-Solar wind-Roe-Upwind-Scheme) described by Groth et al. (2000), provided by CCMC (Community Coordinated Modeling Center) and run at web-site http://ccmc.gsfc.nasa.gov/index.php.

The Space Weather Modeling Framework (BATS-R-US with Rice Convection Model) contains 9 modules that cover the various regions between the Sun and Earth. We have used Global Magnetosphere (GM) module which describes the Earth's magnetosphere and is driven by upstream satellite data (Wind). The GM module includes the magnetosphere from 33 R_E upstream to some 250 R_E downtail. The GM module has a near-Earth boundary located between 2.5 and 3.5 R_E distance from the center of the Earth. Near-Earth boundary conditions are determined by the interaction with the Inner Magnetosphere (IM) module. The IM module obtains the information on closed field lines from GM and the electrostatic potential from the Ionospheric Electrodynamics module and provides density and pressure corrections back to GM. The finest grid resolution is 1/4 R_E around the Earth or in the dayside magnetosphere.

5.5.1 Comparison of observation with GUMICS-4

Andreeova et al. (2008) [A2] compared the case study of the November 9, 2002 events with the global MHD simulation GUMICS-4 .

Satellite	Real data	GUMICS-4
GOES-8	1750:41, 1849:12 UT	1753:00, 1850:30 UT
GOES-10	1750:44, 1849:16 UT	1753:00, 1850:00 UT
Polar	1752:50, 1850:40 UT	1756:00, 1853:30 UT
Cluster-1	1753:20, 1852:10 UT	1755:30, 1853:00 UT

Table 5.6: Observation times for both events as compared to MHD simulation GUMICS-4.

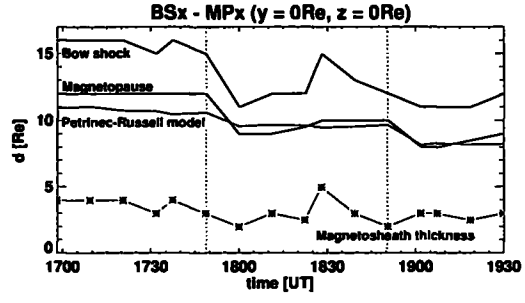

Figure 5.7: November 9, 2002 interplanetary shock event simulation: Magnetopause and bow shock distances from the Earth in R_E. The red line shows the magnetosheath thickness along the Sun-Earth line. The green line shows the magnetopause position derived from the Petrinec and Russell model of the magnetopause using the Wind satellite data.

While in the solar wind, the shock fronts lasted for about 10 s, disturbance fronts in the dayside magnetosphere showed slower compression, and lasted for about 5 min. The simulation produced disturbance fronts, which lasted about 6 minutes. As it was mentioned above, the solar wind shock speeds from the real data were calculated to be about 392 km/s for the first case and about 425 km/s for the second one. Calculated GUMICS-4 shock speeds were about 360 and 420 km/s, Table 5.5. Timing of the real and simulation observations is summarized in Table 5.6. The simulation showed disturbance passages with a time delay about 140 s for the first event and about 60 s for the second event.

GOES-8 and 10 satellites observed magnetic field compressions but there are no plasma measurements on these spacecraft. Polar observed mainly a density compression and almost no magnetic field compression. Apart from the magnetic field compression, Cluster observed also density compression, fluctuations in velocity, and ion deflection (tailward). During simulation, at the position of the real satellites (GOES-8, 10) we found magnetic field and density compression. At the position of Polar, the simulated data showed mainly a density compression. And at the position of Cluster except density compression, there was also weak a magnetic field compression.

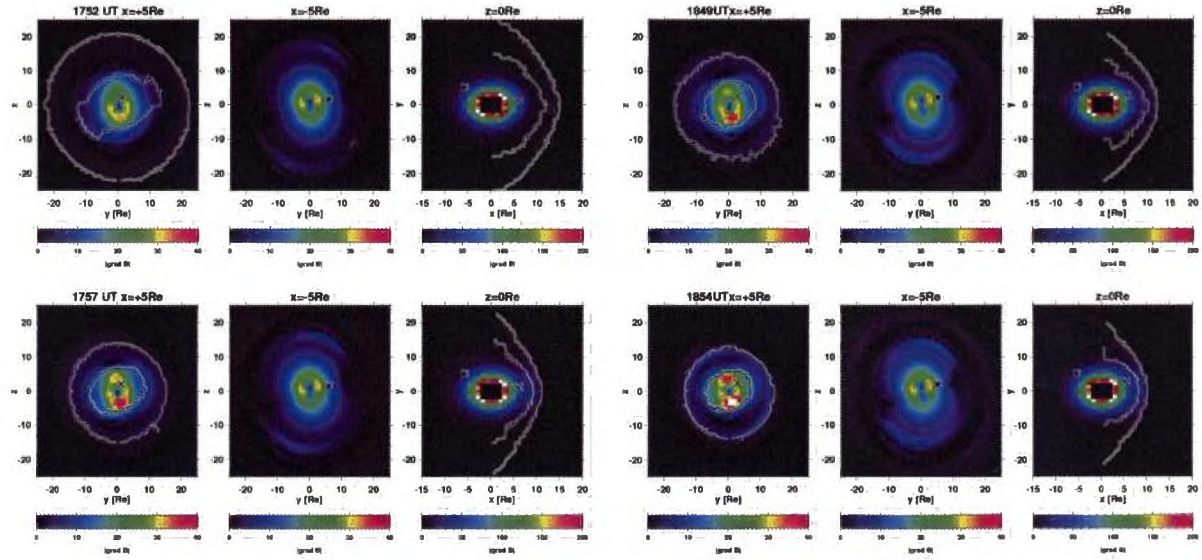

(a) (b)

Figure 5.8: (a) November 9, 2002 interplanetary shock Event 1 simulation: A cross-section of the magnetosphere in the YZ-plane at X = 5 R_E (left), X = -5 R_E (middle), and in the equatorial plane (right) at Z = 0 R_E at 1752 UT (top row) and 1757 UT (bottom row). The color coding shows magnitudes of the magnetic field gradient in nT/R_E. The black and white lines in the left and right panels show the positions of the bow shock and the magnetopause. The position of GOES-8 and Polar are shown with the black and white cross and asterisk, respectively. (b) November 9, 2002 interplanetary shock Event 2 simulation: magnitudes of the magnetic field gradient in nT/R_E in a format similar to panel (a) at 1849 UT (top row) and 1854 UT (bottom row).

According to the simulation, after interaction with FFS, the magnetopause starts to move earthward with the speed of about 30 km/s for both cases. First FFS reaches the magnetopause at time 1750 UT, the second FFS at time 1850 UT. In the second case, the magnetosphere was more compressed, the main reason being the higher solar wind shock speed in the second case. From the density gradient and magnetic field we detected positions of the dayside magnetopause and dayside bow shock. They are shown in Figure 5.7, where we depict the positions of the structures at the nose of the magnetosphere because FFS propagated almost perpendicularly to the Sun-Earth line. The bow shock reacts mainly to changes of the solar wind conditions, magnetic field, and dynamic pressure. Magnetopause interacts with the FFS.

GUMICS-4 showed a solar wind dynamic pressure jump from 1.3 nPa up to 5.1 nPa for the first case and a jump from 3.4 nPa up to 8.8 nPa for the second case. The disturbance speeds in the Earth's magnetosphere were higher for the second case. The real data ob-

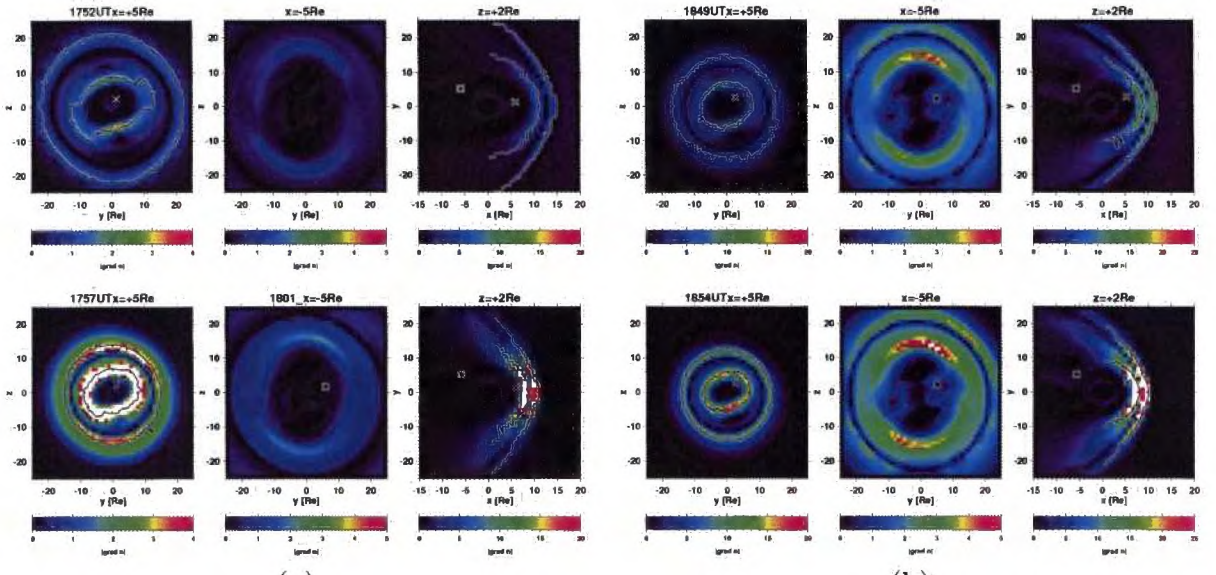

(a) (b)

Figure 5.9: (a) November 9, 2002 interplanetary shock Event 1 simulation: A cross-section of the magnetosphere in the YZ-plane at X = 5 R_E (left), X = -5 R_E (middle), and in the equatorial plane (right) at Z = +2 R_E at 1752 UT (top row) and 1757 UT (bottom row). The color coding shows magnitudes of the plasma density gradient in cm^{-3}/R_E in the given plane. The black and white lines in the left and right panels show the positions of the bow shock and the magnetopause. The position of GOES-8 and Polar are shown with the black and white cross and asterisk, respectively. (b) November 9, 2002 interplanetary shock Event 2 simulation: magnitudes of the plasma density gradient in cm^{-3}/R_E in a format similar to panel (a) at 1849 UT (top row) and 1854 UT (bottom row).

served jump from 1.1 nPa up to 5.2 nPa for the first event and a jump from 3.3 nPa up to 9.3 nPa for the second event. As it was mentioned above, the magnetospheric disturbance speeds were higher for the second event (as shown in Table 5.5).

The GUMICS-4 simulation allows us to trace the whole process of the changing magnetosphere as a response to the shock/disturbance passage. Figures 5.8, 5.9 show the time evolution of the magnetic field and plasma density 2D gradients during the first (1752 and 1757 UT) and the second event (1849 and 1854 UT). The black and white lines represent the positions of the dayside bow shock and the magnetopause. The positions of GOES-8 (black and white cross) and Polar (black and white asterisk) are also depicted in the figures. The panels show cuts in the YZ-plane at X=$\pm$ 5 R_E and in the equatorial plane at Z = 0 R_E for Figure 5.8, and at Z =2 R_E for Figure 5.9.

Figure 5.8 illustrates the strong compression of the magnetosphere during both shock passages. According to the simulation, the bow shock moves from near 16 to near 13

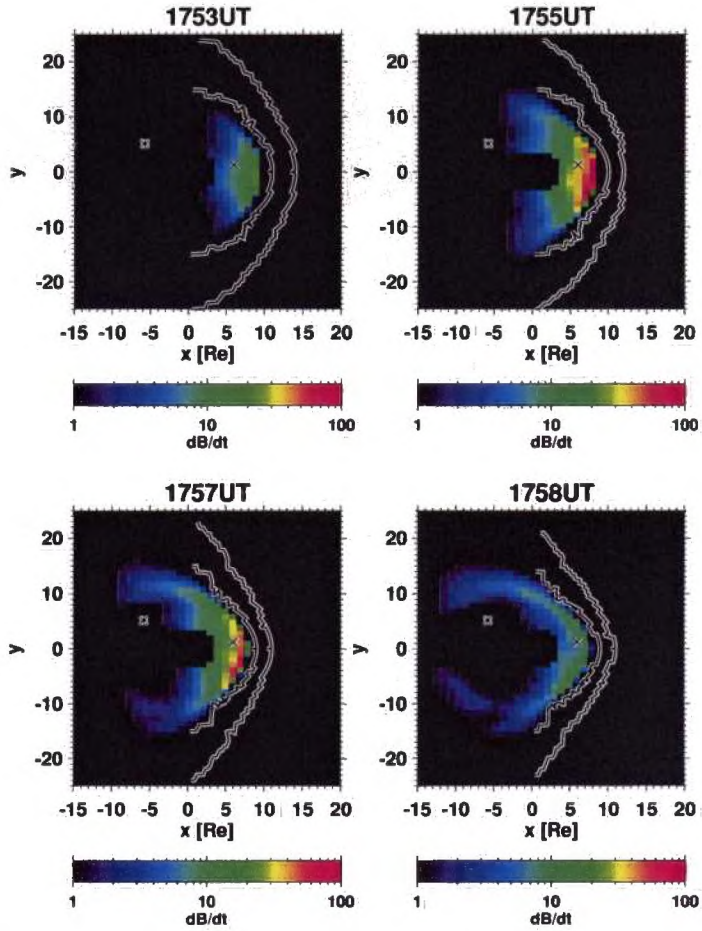

Figure 5.10: November 9, 2002 interplanetary shock Event 1: the disturbance propagation in the equatorial plane using time derivatives of magnetic field in four times: 1753, 1755, 1757, and 1758 UT. The color scale is in nT/min.

R_E during the first event, and from near 15 to near 12 R_E during the second event, see Figure 5.7. The magnetopause compression was not axially symmetric with respect to the Sun-Earth line; during both events, the compression was stronger in the low latitudes than near the polar regions.

Figure 5.9 shows that the Polar satellite was located in the enhanced plasma flow during both events. During the first event, Polar observed a slower increase of the plasma density, which can be interpreted as Polar being at the edge of the plasma flow. During the disturbance passages, the plasma flow crossed over the satellite and was seen as an intensification of the flow speeds at that location. During the second event, the plasma flow was stronger and closer to the Earth, which was caused by an already more compressed magnetosphere after the first disturbance passage.

Figure 5.10 demonstrates that the disturbance front does not stay planar in the magnetosphere. Similarly, recent global MHD simulations (Ridley et al., 2006) have also shown a significant deformation of the interplanetary shock front in the magnetosphere. Further, Koval et al. (2005, 2006b) have shown the IP shock deceleration in the magnetosheath near the magnetopause, according to the observations and simulations.

The normals of both interplanetary shocks are not strictly parallel to the Sun-Earth line and this induces an asymmetry to the disturbance propagation across the magnetosphere as it is demonstrated in Figure 5.10. It displays the disturbance propagation in the equatorial plane using time derivatives of the magnetic field. The compression of the magnetic field is a little stronger in the dayside magnetosphere adjacent to the interplanetary shock front. The disturbance wavefront is slightly faster on the opposite side of the magnetosphere (both dayside and nightside) where the wavefront normal is closer to the original shock propagation direction.

5.5.2 Comparison of GUMICS-4 with BATS-R-US

To compare the real observation and to verify the GUMICS-4 simulation, we performed also simulation of those events using the 3D global BATS-R-US model, Figure 5.11.

In the GUMICS-4 simulation, we used data from Geotail, which was located in front of the Earth's bow shock, as the solar wind input. BATS-R-US simulation used Wind data instead, propagated to the simulation box entry side.

Figure 5.11 brings the magnetic field and plasma density comparison of both simulations with the real observation of the GOES-8 satellite position. At the beginning both simulations observed in the beginning lower values of the magnetic field (about 10nT), however, they attained the same level as real observations after the first shock passage. GUMICS-4 observed larger fluctuations about $\pm$ 10 nT. We have no plasma density observation from GOES satellites. GUMICS-4 observed lower values of the plasma density (from 1.5 cm^{-3} to 10 cm^{-3}) than the BATS-R-US (from 20 cm^{-3} to 25 cm^{-3}) simulation. Both simulations showed similar plasma density profiles. During the first disturbance passage, they saw almost no change in the plasma density. The second event appears that there was stronger plasma compression.

The shock fronts lasted about 30 s in the solar wind, however, in the Earth's magnetosphere, the disturbance fronts lasted about 5 min (GOES-8 and 10), with remark to the fast initial part according to high time resolution data. Simulation BATS-T-US reveals also 5 minutes, simulation GUMICS-4 reveals 7 minutes for the first event, for the second

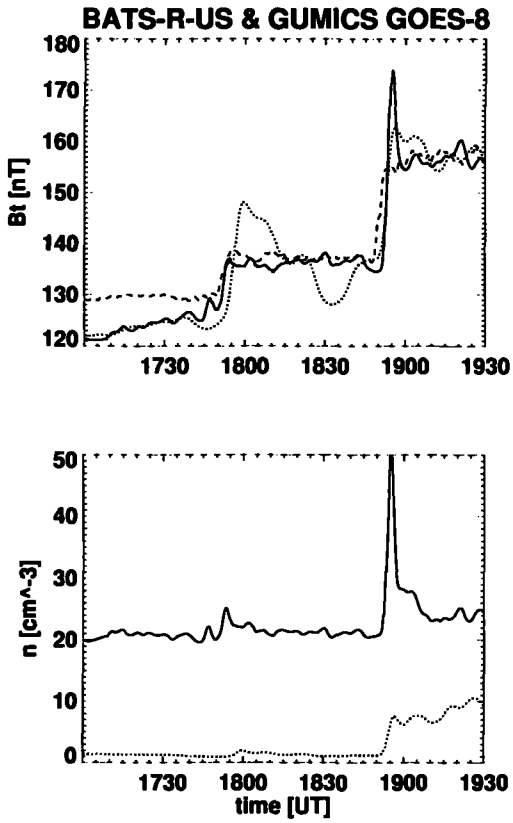

Figure 5.11: November 9, 2002 interplanetary shock event in position of the GOES-8 satellite: comparison of the total magnetic field and plasma density with BATS-R-US and GUMICS-4 simulations. The dashed red line represents the GOES-8 observation, the solid black line represents the BATS-R-US simulation, and the dotted blue line represents the GUMICS-4 simulation.

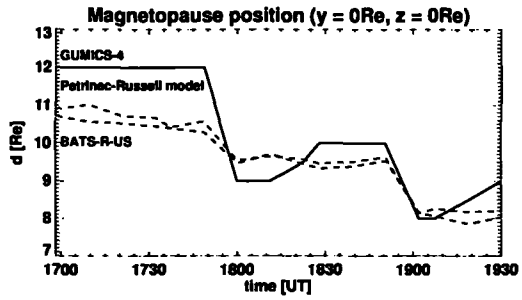

Figure 5.12: November 9, 2002 magnetopause position: the dashed black line shows the magnetopause position derived from the Petrinec and Russell model using the Wind satellite data, the dashed red line shows the results of the BATS-R-US model, and solid black line depicts the GUMICS-4 simulation.

event also 5 minutes. The first passage was observed in the same time according to the BATS-R-US simulation and the GOES-8 satellite observation. GUMICS-4 had 2-minute time delay. In the second case, both simulations showed the same 1-minute time delay here.

Magnetopause positions were compared in Figure 5.12. The BATS-R-US magnetopause position (red dashed line) corresponded mainly to the Petrinec and Russell model. The GUMICS-4 magnetopause position stayed stable till the first moment of the interaction of magnetopause with the IP shock.

Currently the BATS-R-US tool allows a slightly better time resolution of the simulation than GUMICS-4. Both models cannot perform the exact simulation of real events, as they need to set $B_X = 0$ at the solar wind input. Also they enter the same solar wind input conditions at the whole simulation box entry side. Because of that it was not possible to simulate oblique structures in the solar wind like CIR driven shocks and other similar phenomena. The MHD model by Samsonov will be soon ready to perform simulations of this kind.

Chapter 6

Conclusions

The main part of the thesis concentrates on the analysis and simulation of a fast forward shock in the solar wind and its evolution through the magnetosheath to the inner magnetosphere.

In our statistical study (Andreeova and Prech, 2007b) and (Andreeova and Prech, 2007a)[A1] based on 42 events registered during 1997-2006 years we have investigated the propagation of IP shocks in the Earth's magnetosphere. Under assumptions of planar shocks, we calculated shock normals applying different methods (Andreeova and Prech, 2007b) and associated disturbance speeds inside the magnetosphere using a timing of various spacecraft. We obtained speeds in the range of 450-1500 km/s (consistently with Nopper et al. (1982) and Wilken et al. (1982)). We showed that the disturbance speeds in the magnetosphere are higher than the original shock speed in the solar wind and that the propagation speeds gradually increase tailward from the subsolar point. Furthermore, a comparison of propagation speeds with the upstream solar wind dynamic pressure showed that these speeds are larger for higher dynamic pressure. The dependence of disturbance speeds in the magnetosphere on the southward/northward Bz component and the IP shock compression ratios were not clear enough in our data set.

In details, we studied double fast forward shocks on November 9, 2002 using measurements of many spacecraft (Andreeova and Prech, 2007a; Andreeova et al., 2008)[A1,A2]. For these two shocks, we estimated the speeds of disturbance propagation between the dayside and nightside magnetosphere to be 590 km/s and 714-741 km/s, respectively. We partially attributed this increase to higher Alfven speed in the outer magnetosphere due to the compression of the magnetosphere as a consequence of the first event, and partially to the faster and stronger driving interplanetary shock. Furthermore, high-time resolution GOES magnetic field data revealed a complex structure of the compressional wave fronts at

the dayside geosynchronous orbit during these events, with initial very steep parts (10 s). We discussed the double-step profiles in the density and magnetic field during the passage of the IP shock through the magnetosheath (Šafránková et al., 2007a,b; Samsonov et al., 2006).

The observations of the November events were compared with the GUMICS-4 and BATS-R-US global MHD models (Andreeova et al., 2008)[A2]. The simulation results allow us to trace the 3D propagations of the IP shock front in different regions of the magnetosphere. Using these simulations, we confirmed that the disturbance speeds in the Earth's magnetosphere were higher for the second shock due to the higher dynamic pressure. Moreover, we showed that the profile and speed changes were largest within the high-latitude magnetosheath and plasma sheet and that the front of the disturbance is significantly deformed in the magnetosphere (Andreeova et al., 2008)[A2].

Bibliography

Abraham-Shrauner, B., 1972. Determination of magnetohydrodynamic shock normals. J. Geophys. Res. 77, 736–739.

Abraham-Shrauner, B., Yun, S. H., 1976. Interplanetary shocks seen by AMES plasma probe on Pioneer 6 and 7. J. Geophys. Res. 81, 2097–2102.

Akasofu, S.-I., Apr. 1964. The development of the auroral substorm. Planet. Space Sci. 12, 273–+.

Andreeova, K., Prech, L., 2007a. Propagation of interplanetary shocks into the Earth's magnetosphere. Adv. Space Res. 40, 1871–1880, doi:10.1016/j.asr.2007.04.079.

Andreeova, K., Prech, L., 2007b. Properties of Fast Forward Shock Caused Waves in the Magnetosphere. in WDS'07 Proceedings of Contributed Papers: Part II - Physics of Plasmas and Ionized Media, 7–13Edited by J. Safrankova and J. Pavlu, Prague, Matfyzpress.

Andreeova, K., Pulkkinen, T. I., Laitinen, T., Prech, L., 2008. Shock propagation in the magnetosphere: Observations and MHD simulations compared. J. Geophys. Res., accepted.

Araki, T., 1977. Global structure of geomagnetic sudden commencements. Planet. Space Sci. 25, 373–384.

Balogh, A., Dunlop, M. W., Cowley, S. W. H., Southwood, D. J., Thomlinson, J. G., Glassmeier, K. H., Musmann, G., Luhr, H., Buchert, S., Acuna, M. H., Fairfield, D. H., Slavin, J. A., Riedler, W., Schwingenschuh, K., Kivelson, M. G., 1997. The Cluster Magnetic Field Investigation. Space Sci. Rev. 79, 65–91.

Bartels, J., Heck, N. H., Johnston, H. F., 1939. The three-hour-range index measuring geomagnetic activity. J. Geophys. Res. 44, 441.

Bellomo, A., Mavretic, A., 1978. Description of the MIT plasma experiment on IMP 7/8. in Rep. CSR TR-78-2, 51 Cent. for Space Res., MIT, Cambridge.

Berdichevsky, D. B., Szabo, A., Lepping, R. P., Vinas, A. F., Mariani, F., 2000. Interplanetary fast shocks and associated drivers observed through the 23rd solar minimum by Wind over its first 2.5 years. J. Geophys. Res. 105, 27289–27314.

Burlaga, L. F., 1971. Hydromagnetic waves and discontinuities in the solar wind. Space Sci. Rev. 12, 600–657.

Cable, S., Lin, Y., 1998. Three-dimensional MHD simulations of interplanetary rotational discontinuities impacting the Earth's bow shock and magnetosheath. J. Geophys. Res. 103, 29551–29568.

Carr, C., Brown, P., Zhang, T. L., Aydogar, O., Magnes, W., Auster, U., Balogh, A., Beek, T., Eichelberger, H., Fornacon, K.-H., Georgescu, E., Gloag, J., Liao, H., Ludlam, M., Nakamura, R., O'Brien, H., Oddy, T., Richter, I., 2006. The Double Star magnetic field investigation: Overview of instrument performance and initial results. Adv. Space Res. 38, 1828–1833.

Cornilleau-Wehrlin, N., Alleyne, H., Yearby, K., de la Porte de Vaux, B., Santolik, O., Parrot, M., Belmont, G., Rezeau, L., Le Contel, O., Roux, A., Attie, D., Robert, P., Bouzid, V., Herment, D., Cao, J., 2005. The staff-dwp wave instrument on the dsp equatorial spacecraft: description and first results. Annales Geophysicae 23, 2785 – 2801.

Davis, T. N., Sugiura, M., 1966. Auroral Electrojet Activity Index AE and Its Universal Time Variations. J. Geophys. Res. 71, 785–+.

Farris, M. H., Russell, C. T., 1994. Determining the standoff distance of the bow shock: Mach number dependence and use of models. J. Geophys. Res. 99, 17681.

Farrugia, C. J., Freeman, M. P., Cowley, S. W. H., Southwood, D. J., Lockwood, M., Etemadi, A., 1989. Pressure-driven magnetopause motions and attendant response on the ground. Planet. Space Sci. 37, 589–607.

Formisano, V., 1979. Orientation and shape of the earth's bow shock in three dimensions. Planet. Space Sci. 27, 1151–1161.

Formisano, V., Hedgecock, P. C., Moreno, G., Sear, J., Bollea, D., 1971. Observations of Earth's bow shock for low mach numbers. Planet. Space Sci. 19, 1519–1531.

Gonzales, W. D., Joselyn, J. A., Kamide, Y., Kroehl, H. W., Rostoker, G., Tsurutani, B. T., Vasyliunas, V. M., 1994. What is a geomagnetic storm? J. Geophys. Res. 99, 5771–5792.

Gonzalez, W. D., Tsurutani, B. T., Clúa de Gonzalez, A. L., 1999. Interplanetary origin of geomagnetic storms. Space Sci. Rev. 88, 529–562.

Grib, S. A., 1982. Interaction of non-perpendicular/parallel solar wind shock waves with the Earth's magnetosphere. Space Sci. Rev. 32, 43–48.

Grib, S. A., Briunelli, B. E., Dryer, M., Shen, W.-W., 1979. Interaction of interplanetary shock waves with the bow shock-magnetopause system. J. Geophys. Res. 84, 5907–5921.

Groth, C. P. T., De Zeeuw, D. L., Gombosi, T. I., Powell, K. G., 2000. Global three-dimensional MHD simulation of a space weather event: CME formation, interplanetary propagation, and interaction with the magnetosphere. J. Geophys. Res. 105, 25053–25078.

Guo, X.-C., Hu, Y.-Q., Wang, C., 2005. Earth's magnetosphere impinged by interplanetary shocks of different orientations. Chin. Phys. Lett. 22, 3221–3224.

Harvey, P., Mozer, F. S., Pankow, D., Wygant, J., Maynard, N. C., Singer, H., Sullivan, W., Anderson, P. B., Pfaff, R., Aggson, T., Pedersen, A., Fälthammar, C.-G., Tanskannen, P., Feb. 1995. The Electric Field Instrument on the Polar Satellite. Space Sci. Rev. 71, 583–596.

Ipavich, F. M., Galvin, A. B., Lasley, S. E., Paquette, J. A., Hefti, S., Reiche, K.-U., Coplan, M. A., Gloeckler, G., Bochsler, P., Hovestadt, D., Grünwaldt, H., Hilchenbach, M., Gliem, F., Axford, W. I., Balsiger, H., Bürgi, A., Geiss, J., Hsieh, K. C., Kallenbach, R., Klecker, B., Lee, M. A., Managadze, G. G., Marsch, E., Möbius, E., Neugebauer, M., Scholer, M., Verigin, M. I., Wilken, B., Wurz, P., 1998. Solar wind measurements with SOHO: The CELIAS/MTOF proton monitor. J. Geophys. Res. 103, 17205–17214.

Janhunen, P., 1996. GUMICS-3 A Global Ionosphere-Magnetosphere Coupling Simulation with High Ionospheric Resolution. In: Guyenne, T.-D., Hilgers, A. (Eds.), Environment Modeling for Space-Based Applications. Vol. 392 of ESA Special Publication. pp. 233–+.

Jeřáb, M., Němeček, Z., Šafránková, J., Jelínek, K., Měrka, J., 2005. A study of bow shock locations. Planet. Space Sci. 53, 85–94.

Kasper, J. C., 2005. Interplanetary shock database from WIND satellite. URL `http://space.mit.edu/home/jck/shockdb/shockdb.htm`

Keika, K., Nakamura, R., Baumjohann, W., Runov, A., Takada, T., Volwerk, M., Zhang, T. L., Klecker, B., Lucek, E. A., Carr, C., Rème, H., Dandouras, I., André, M., Frey, H., 2008. Response of the inner magnetosphere and the plasma sheet to a sudden impulse. J. Geophys. Res. 113, 7–+, doi:10.1029/2007JA012763.

Kivelson, M. G., Russell, C. T., 1995. Introduction to Space Physics. Introduction to Space Physics, Edited by Margaret G. Kivelson and Christopher T. Russell, pp. 586. ISBN 0521451043. Cambridge, UK: Cambridge University Press, April 1995.

Klimov, S., Romanov, S., Amata, E., Blecki, J., Büchner, J., Juchniewicz, J., Rustenbach, J., Triska, P., Woolliscroft, L. J. C., Savin, S., Afanas'yev, Y., de Angelis, U., Auster, U., Bellucci, G., Best, A., Farnik, F., Formisano, V., Gough, P., Grard, R., Grushin, V., Haerendel, G., Ivchenko, V., Korepanov, V., Lehmann, H., Nikutowski, B., Nozdrachev, M., Orsini, S., Parrot, M., Petrukovich, A., Rauch, J. L., Sauer, K., Skalsky, A., Slominski, J., Trotignon, J. G., Vojta, J., Wronowski, R., 1997. ASPI experiment: measurements of fields and waves on board the INTERBALL-1 spacecraft. Annales Geophysicae 15, 514–527.

Kokubun, S., Yamamoto, T., Acuna, M. H., Hayashi, K., Shiokawa, K., Kawano, H., 1994. The Geotail Magnetic Field Experiment. J. Geomag. Geoelectr. 46, 7–21.

Koval, A., Šafránková, J., Němeček, Z., Přech, L., 2006a. Propagation of interplanetary shocks through the solar wind and magnetosheath. Advances in Space Research 38, 552–558.

Koval, A., Šafránková, J., Němeček, Z., Přech, L., Samsonov, A. A., Richardson, J. D., 2005. Deformation of interplanetary shock fronts in the magnetosheath. Geophys. Res. Let. 32, L15101, doi:10.1029/2005GL023009.

Koval, A., Šafránková, J., Němeček, Z., Samsonov, A. A., Přech, L., Richardson, J. D., Hayosh, M., 2006b. Interplanetary shock in the magnetosheath: Comparison of experimental data with MHD modeling. Geophys. Res. Let. 33, L11102, doi:10.1029/2006GL025707.

Laughlin, L. K., Turner, N. E., Mitchell, E. J., 2008. Geoeffectiveness of CIR and CME Events: Factors Contributing to Their Differences. Journal of the Southeastern Association for Research in Astronomy 2, 19–22.

Lepping, R. P., Acũna, M. H., Burlaga, L. F., Farrell, W. M., Slavin, J. A., Schatten, K. H., Mariani, F., Ness, N. F., Neubauer, F. M., Whang, Y. C., Byrnes, J. B., Kennon, R. S., Panetta, P. V., Scheifele, J., Worley, E. M., 1995. The Wind Magnetic Field Investigation. Space Sci. Rev. 71, 207–229.

Lepping, R. P., Argentiero, P. D., 1971. Single spacecraft method of estimating shock normals. J. Geophys. Res. 76, 4349–4359.

Lin, R. P., Anderson, K. A., Ashford, S., Carlson, C., Curtis, D., Ergun, R., Larson, D., McFadden, J., McCarthy, M., Parks, G. K., Rème, H., Bosqued, J. M., Coutelier, J., Cotin, F., D'Uston, C., Wenzel, K.-P., Sanderson, T. R., Henrion, J., Ronnet, J. C., Paschmann, G., 1995. A Three-Dimensional Plasma and Energetic Particle Investigation for the Wind Spacecraft. Space Sci. Rev. 71, 125–153.

McComas, D. J., Bame, S. J., Barker, P., Feldman, W. C., Phillips, J. L., Riley, P., Griffee, J. W., 1998a. Solar Wind Electron Proton Alpha Monitor (SWEPAM) for the Advanced Composition Explorer. Space Sci. Rev. 86, 563–612.

McComas, D. J., Riley, P., Gosling, J. T., Balogh, A., Forsyth, R., Feb. 1998b. Ulysses rapid crossing of the polar coronal hole boundary. J. Geophys. Res. 103, 1955–1967.

Merka, J., Szabo, A., Narock, T. W., King, J. H., Paularena, K. I., Richardson, J. D., 2003. A comparison of IMP 8 observed bow shock positions with model predictions. J. Geophys. Res. 108, 6–1, doi:10.1029/2002JA009384.

Mukai, T., Machida, S., Saito, Y., Hirahara, M., Terasawa, T., Kaya, N., Obara, T., Ejiri, M., A., N., 1994. The low energy particle (LEP) experiment onboard the Geotail satellite. J. Geomagn. Geoelectr. 46, 669–692.

Nemecek, Z., Safrankova, J., 1991. The Earth's bow shock and magnetopause position as a result of the solar wind-magnetosphere interaction. J. Atmos. Terr. Phys. 53, 1049–1054.

Newbury, J. A., 2000. Plasma heating and thermal transport in the solar wind near 1 AU. Ph.D. thesis, University of California, Los Angeles.

Nopper, Jr., R. W., Hughes, W. J., Maclennan, C. G., McPherron, R. L., 1982. Impulse-excited pulsations during the July 29, 1977, event. J. Geophys. Res. 87, 5911–5916.

Nozdrachev, M. N., Skalsky, A. A., Styazhkin, V. A., Petrov, V. G., 1998. Some Results of Magnetic Field Measurements by the FM-3I Flux-Gate Instrument Onboard the INTERBALL-1 Spacecraft. Cosmic Research 36, 251–+.

Ogilvie, K. W., Chornay, D. J., Fritzenreiter, R. J., Hunsaker, F., Keller, J., Lobell, J., Miller, G., Scudder, J. D., Sittler, Jr., E. C., Torbert, R. B., Bodet, D., Needell, G., Lazarus, A. J., Steinberg, J. T., Tappan, J. H., Mavretic, A., Gergin, E., 1995. SWE, A Comprehensive Plasma Instrument for the Wind Spacecraft. Space Sci. Rev 71, 55–77.

Parker, E. N., 1958. Dynamics of the Interplanetary Gas and Magnetic Fields. Astrophysical Journal 128, 664–676.

Parker, E. N., 1963. Interplanetary dynamical processes. New York, Interscience Publishers, 1963.

Paschmann, G., Haerendel, G., Sckopke, N., Moebius, E., Luehr, H., 1988. Three-dimensional plasma structures with anomalous flow directions near the Earth's bow shock. J. Geophys. Res. 93, 11279–11294.

Peredo, M., Slavin, J. A., Mazur, E., Curtis, S. A., 1995. Three-dimensional position and shape of the bow shock and their variation with Alfvenic, sonic and magnetosonic Mach numbers and interplanetery magnetic field orientation. J. Geophys. Res. 100, 7907–7916.

Petrinec, S. M., Russell, C. T., 1996. Near-Earth magnetopause shape and size as determined from the magnetopase flaring angle. J. Geophys. Res. 101, 137–152.

Petrinec, S. P., Song, P., Russell, C. T., 1991. Solar cycle variations in the size and shape of the magnetopause. J. Geophys. Res. 96, 7893–7896.

Prech, L., Safrankova, J., Nemecek, Z., 2008. Response of magnetospheric boundaries to the interplanetary shock: Themis contribution. Geophys. Res. Lett. 35, L17S02, doi:10.1029/2008GL033593.

Reme, H., Bosqued, J. M., Sauvaud, J. A., Cros, A., Dandouras, J., Aoustin, C., Bouyssou, J., Camus, T., Cuvilo, J., Martz, C., Medale, J. L., Perrier, H., Romefort, D., Rouzaud,

J., D'Uston, C., Mobius, E., Crocker, K., Granoff, M., Kistler, L. M., Popecki, M., Hovestadt, D., Klecker, B., Paschmann, G., Scholer, M., Carlson, C. W., Curtis, D. W., Lin, R. P., McFadden, J. P., Formisano, V., Amata, E., Bavassano-Cattaneo, M. B., Baldetti, P., Belluci, G., Bruno, R., Chionchio, G., di Lellis, A., Shelley, E. G., Ghielmetti, A. G., Lennartsson, W., Korth, A., Rosenbauer, H., Lundin, R., Olsen, S., Parks, G. K., McCarthy, M., Balsiger, H., 1997. The Cluster Ion Spectrometry (cis) Experiment. Space Sci. Rev. 79, 303–350.

Ridley, A. J., De Zeeuw, D. L., Manchester, W. B., Hansen, K. C., 2006. The magnetospheric and ionospheric response to a very strong interplanetary shock and coronal mass ejection. Adv. Space Res. 38, 263–272.

Russell, C. T., Snare, R. C., Means, J. D., Pierce, D., Dearborn, D., Larson, M., Barr, G., Le, G., 1995. The GGS/POLAR magnetic fields investigation. Space Sci. Rev. 71, 563–582.

Russell, C. T., Wang, Y. L., Raeder, J., Tokar, R. L., Smith, C. W., Ogilvie, K. W., Lazarus, A. J., Lepping, R. P., Szabo, A., Kawano, H., Mukai, T., Savin, S., Yermolaev, Y. I., Zhou, X.-Y., Tsurutani, B. T., 2000. The interplanetary shock of September 24, 1998: Arrival at Earth. J. Geophys. Res. 105, 25143–25154.

Russell, C. T., Zhou, X. W., Chi, P. J., Kawano, H., Moore, T. E., Peterson, W. K., Cladis, J. B., Singer, H. J., 1999. Sudden compression of the outer magnetosphere associated with an ionospheric mass ejection. Geophys. Res. Let. 26, 2343–2346.

Safrankova, J., Zastenker, G., Nemecek, Z., Fedorov, A., Simersky, M., Prech, L., May 1997. Small scale observation of magnetopause motion: preliminary results of the INTERBALL project. Annales Geophysicae 15, 562–569.

Samsonov, A. A., Němeček, Z., Šafránková, 2006. Numerical MHD modeling of propagation of interplanetary shock through the magnetosheath. J. Geophys. Res. 111, A08210, doi:10.1029/2005JA011537.

Samsonov, A. A., Sibeck, D. G., Imber, J., 2007. MHD simulation for the interaction of an interplanetary shock with the Earth's magnetosphere. J. Geophys. Res. 112, 12220–+.

Schwartz, S. J., 1995. Hot flow anomalies near the Earth's bow shock. Adv. Space Res. 15, 107–106.

Schwartz, S. J., Chaloner, C. P., Hall, D. S., Christiansen, P. J., Johnstones, A. D., 1985. An active current sheet in the solar wind. Nature 318, 269–271.

Schwartz, S. J., Kessel, R. L., Brown, C. C., Woolliscroft, L. J. C., Dunlop, M. W., 1988. Active current sheets near the Earth's bow shock. J. Geophys. Res. 93, 11295–11310.

Schwartz, S. J., Paschmann, G., Sckopke, N., Bauer, T. M., Dunlop, M., Fazakerley, A. N., Thomsen, M. F., 2000. Conditions for the formation of hot flow anomalies at Earth's bow shock. J. Geophys. Res. 105, 12639–12650.

Sibeck, D. G., Borodkova, N. L., Schwartz, S. J., Owen, C. J., Kessel, R., Kokubun, S., Lepping, R. P., Lin, R., Liou, K., Lühr, H., McEntire, R. W., Meng, C.-I., Mukai, T., Nemecek, Z., Parks, G., Phan, T. D., Romanov, S. A., Safrankova, J., Sauvaud, J.-A., Singer, H. J., Solovyev, S. I., Szabo, A., Takahashi, K., Williams, D. J., Yumoto, K., Zastenker, G. N., 1999. Comprehensive study of the magnetospheric response to a hot flow anomaly. J. Geophys. Res. 104, 4577–4594.

Sibeck, D. G., Takahashi, K., Kokubun, S., Mukai, T., Ogilvie, K. W., Szabo, A., 1997. A case study of oppositely propagating Alfvénic fluctuations in the solar wind and magnetosheath. Geophys. Res. Let. 24, 3133–3136.

Singer, H. J., Matheson, L., Grubb, R., Newman, A., Bouwer, S. D., 1996. Monitoring space weather with the GEOS magnetometers. SPIE conference proceedings, GEOS-8 and Beyond 2812, 299–308.

Smith, C. W., L'Heureux, J., Ness, N. F., Acuña, M. H., Burlaga, L. F., Scheifele, J., Jul. 1998. The ACE Magnetic Fields Experiment. Space Sci. Rev. 86, 613–632.

Smith, E. J., Wolfe, J. H., 1976. Observations of interaction regions and corotating shocks between one and five AU - Pioneers 10 and 11. Geophys. Res. Let. 3, 137–140.

SOHO, 2007. Interplanetary shocks and other interesting events from SOHO satellite. URL `http://umtof.umd.edu/pm/figs.html`

Spreiter, J. R., Stahara, S. S., 1994. Gasdynamic and magnetohydrodynamic modeling of the magnetosheath: A tutorial. Adv. Space Res. 14, 5–19.

Sugiura, M., Wilson, C. R., 1964. Oscillation of the Geomagnetic Field Lines and Associated Magnetic Perturbations at Conjugate Points. J. Geophys. Res. 69, 1211–+.

Szabo, A., 1994. An improved solution to the 'Rankine-Hugoniot' problem. J. Geophys. Res. 99, 14737–+.

Tamao, T., 1964. The structure of three-dimensional hydromagnetic waves in a uniform cold plasma. J. Geomagn. Geoelectr. 18, 89–114.

Thomsen, M. F., Gosling, J. T., Bame, S. J., Quest, K. B., Russell, C. T., 1988. On the origin of hot diamagnetic cavities near the earth's bow shock. J. Geophys. Res. 93, 11311–11325.

Tsurutani, B. T., Gonzalez, W. D., Gonzalez, A. L. C., Tang, F., Arballo, J. K., Okada, M., 1995. Interplanetary origin of geomagnetic activity in the declining phase of the solar cycle. J. Geophys. Res. 100, 21717–21734.

Šafránková, J., Přech, L., Němeček, Z., Sibeck, D., 2002. The structure of hot flow anomalies in the magnetosheath. Adv. Space Res. 30, 2737–2744.

Šafránková, J., Němeček, Z., Přech, L., Samsonov, A. A., Koval, A., Andréeová, K., 2007a. Interaction of interplanetary shocks with the bow shock. Planet. Space Sci. 55, 2324–2329, doi: 10.1016/j.pss.2007.05.012.

Šafránková, J., Němeček, Z., Přech, L., Samsonov, A. A., Koval, A., Andréeová, K., 2007b. Modification of interplanetary shocks near the bow shock and through the magnetosheath. J. Geophys. Res. 112, 8212–+, doi:10.1029/2007JA012503.

Viñas, A. F., Scudder, J. D., 1986. Fast and optimal solution to the 'Rankine-Hugoniot problem'. J. Geophys. Res. 91, 39–58.

Villante, U., Lepidi, S., Francia, P., Bruno, T., 2004. Some aspects of the interaction of interplanetary shocks with the Earth's magnetosphere: an estimate of the propagation time through the magnetosheath. J. Atm. Solar-Terr. Phys. 66, 337–341.

Whang, Y. C., 1991a. Parametric study of the formation of magnetohydrodynamic shocks. I - Model. II - Slow shocks. Astrophysical Journal 377, 250–262.

Whang, Y. C., 1991b. Shock interactions in the outer heliosphere. Space Sci. Rev. 57, 339–388.

Wilken, B., Goertz, C. K., Baker, D. N., Higbie, P. R., Fritz, T. A., 1982. The SSC on July 29, 1977 and its propagation within the magnetosphere. J. Geophys. Res. 87, 5901–5910.

Yan, M., Lee, L. C., 1994. Generation of slow-mode waves in front of the dayside magnetopause. Geophys. Res. Let. 21, 629–632.

Yan, M., Lee, L. C., 1996. Interaction of interplanetary shocks and rotational discontinuities with the Earth's bow shock. J. Geophys. Res. 101, 4835–4848.

Zhuang, H. C., Russell, C. T., Smith, E. J., Gosling, J. T., 1981. Three-dimensional interaction of interplanetary shock waves with the bow shock and magnetopause - A comparison of theory with ISEE observations. J. Geophys. Res. 86, 5590–5600.

Appendix A

List of publications

Papers included in the thesis

A1 **Andreeova, K.**, L. Prech (2007), Propagation of interplanetary shocks into the Earths magnetosphere, *Adv. Space Res.*, 40, 1871-1880.

A2 **Andreeova, K.**, T. I. Pulkkinen, T. V. Laitinen, L. Prech (2008), Interaction of interplanetary shocks with the Earth's magnetosphere: Observations and global MHD simulations compared during the Nov 9, 2002 event, accepted to *J. Geophys. Res.*.

Other papers related to the topics

- **Andreeova, K.** (2005), Interaction between IMF discontinuities or shocks and the Earth's Bow Shock, in WDS'05 *Proceedings of Contributed Papers: Part II - Physics of Plasmas and Ionized Media*, edited by J. Safrankova, pp. 213-219, Prague, Matfyzpress.

- **Andreeova, K.**, and L. Prech (2006), Propagation of interplanetary shocks into the Earth's magnetosphere, in WDS'06 *Proceedings of Contributed Papers: Part II - Physics of Plasmas and Ionized Media*, edited by J. Safrankova and J. Pavlu, pp. 7-13, Prague, Matfyzpress.

- **Andreeova, K.**, and L. Prech (2007), Properties of Fast Forward Shock Caused Waves in the Magnetosphere, in WDS'07 *Proceedings of Contributed Papers: Part II - Physics of Plasmas and Ionized Media*, edited by J. Safrankova and J. Pavlu, pp. 22-28, Prague, Matfyzpress.

- Safrankova, J., Z. Nemecek, L. Prech, A. A. Samsonov, A. Koval, and **K. Andreeova**

(2007), Interaction of interplanetary shocks with the bow shock, *Planet. Space Sci.*, 55, 2324-2329.

- Safrankova, J., Z. Nemecek, L. Prech, A. A. Samsonov, A. Koval, and **K. Andreeova** (2007), Modification of interplanetary shocks near the bow shock and through the magnetosheath, *J. Geophys. Res.*, 112, A08212, doi:10.1029/2007JA012503.

Appendix B

Attached article

[A1] **Andreeova, K.**, L. Prech (2007), Propagation of interplanetary shocks into the Earths magnetosphere, *Adv. Space Res.*, 40, 1871-1880.

Available online at www.sciencedirect.com
ScienceDirect
Advances in Space Research 40 (2007) 1871–1880
ADVANCES IN SPACE RESEARCH (a COSPAR publication)
www.elsevier.com/locate/asr

Propagation of interplanetary shocks into the Earth's magnetosphere

K. Andréeová, L. Přech *

Charles University, Faculty of Mathematics and Physics, V Holesovickach 2, CZ-18000 Prague 8, Czech Republic

Received 9 November 2006; received in revised form 23 April 2007; accepted 24 April 2007

Abstract

This paper is devoted to the study of propagation of disturbances caused by interplanetary shocks (IPS) through the Earth's magnetosphere. Using simultaneous observations of various fast forward shocks by different satellites in the solar wind, magnetosheath and magnetosphere from 1995 till 2002, we traced the interplanetary shocks into the Earth's magnetosphere, we calculated the velocity of their propagation into the Earth's magnetosphere and analyzed fronts of the disturbances. From the onset of disturbances at different satellites in the magnetosphere we obtained speed values ranging from 500 to 1300 km/s in the direction along the IP shock normal, that is in a general agreement with results of previous numerical MHD simulations. The paper discusses in detail a sequence of two events on November 9th, 2002. For the two cases we estimated the propagation speed of the IP shock caused disturbance between the dayside and nightside magnetosphere to be ~590 km/s and ~714–741 km/s, respectively. We partially attributed this increase to higher Alfven speed in the outer magnetosphere due to the compression of the magnetosphere as a consequence of the first event, and partially to the faster and stronger driving interplanetary shock. High-time resolution GOES magnetic field data revealed a complex structure of the compressional wave fronts at the dayside geosynchronous orbit during these events, with initial very steep parts (~10 s). We discuss a few possible mechanisms of such steep front formation in the paper.

Keywords: Interplanetary shock; Magnetosphere; Magnetosphere–solar wind interaction; Propagation speed; Compressional waves; Shock front profile

1. Introduction

Influences of external sources on the Earth's magnetosphere have already been studied by many authors, e.g., Le et al. (1998); Le and Russell (1998); Zhuang et al. (1981). Interplanetary shocks (IPS) represent structures, which can propagate in the solar wind into planetary magnetospheres and interact with them effectively, causing their compressions/expansions and modifying magnetopause and tail currents. On the ground, these processes are related to phenomena called sudden commencements/sudden impulses. Their effect on human technologies leads to a need to study these phenomena.

Interplanetary shocks are driven by two main sources, first by coronal mass ejections/magnetic clouds (CME/MC) and other solar transients and second by corotating interaction regions (CIR). Because of the large scale of these phenomena, interplanetary shocks are in general assumed to be planar, at least in the Earth's magnetosphere cross-scale (Russell et al., 2000). Several authors (e.g., Szabo et al., 2001) show that some observations should be explained rather by a curved surface of the IPS. The occurrence rate and mean strength of the interplanetary fast shocks seem to be correlated with the solar cycle (Berdichevsky et al., 2000).

Interplanetary shocks can be classified according to jumps of plasma parameters and magnetic field strength as fast/slow shocks and forward/reverse shocks (Burlaga, 1971). In this paper, we selected fast forward shocks (FFS) among other interplanetary shock observations.

* Corresponding author.
E-mail addresses: andreeova@seznam.cz (K. Andréeová), lubomir.prech@mff.cuni.cz (L. Přech).

0273-1177/$30
doi:10.1016/j.asr.2007.04.079

magnetosphere. By chance, they make it possible to describe the interplanetary shocks' propagation around the magnetosphere in much greater detail, namely to compare fronts and their speeds in various places. This is a motivation of this paper.

2. Data sources – instruments

To investigate interaction of interplanetary shocks with the Earth's magnetosphere, we use simultaneous data from different satellites. Onboard instruments and their time resolution are summarized in Table 1.

For the study, we selected suitable events from the Wind/ACE/IMP–8 interplanetary shock database compiled by Kasper (2005), who provided also shock parameters derived by a number of available methods, namely interplanetary shock normal and velocity vectors. For some intervals (with a sufficient number of S/C localized in the solar wind) we were also able to verify these parameters with values obtained from the timing and position of 4 S/C observations of the interplanetary shock in the solar wind.

3. Analysis of events

Table 2 shows the list of selected fast forward shocks (observed by the Wind satellite). As we wanted to verify propagation speeds inside the magnetosphere, we searched in particular for events during which the GOES satellites are in the dayside near local noon and other satellites can be found operating also in the dayside or on the flanks of the magnetosphere. At the same time, we required good data coverage upstream of the bow shock, possibly allowing to distinguish foreshock effects. It turns that such constraints considerably limit the number of events that can be studied.

Table 1
The table summarizes satellites, instruments, and available time resolution used in this study

Satellite	Instrument	Time resolution [s]
ACE	Magnetic Field (MFI)	16
	Parameters of Plasma (SWE)	64
Wind	Magnetic Field Investigation (MFI)	3
	Solar Wind Experiment (SWE)	100
	3D Plasma Analyzer (3DP PESA Low)	3
Interball–1	Magnetometers (MIF/FM3)	6
	Magnetosheath Ion Flux (VDP)	1
IMP–8	Magnetometer (MAG)	15
	Parameters of Plasma (PLA)	60
Geotail	Magnetic Field (MGF)	3
	Energetic Particles (LEP)	12
	Comprehensive Plasma Instrument (CPI)	50
GOES	Magnetometer (MAG)	60, 0.512
Polar	Magnetic Fields Experiment (MFE)	55, 6
	Electric Field Instrument (EFI)	6
Cluster	Magnetic Field Investigation (FGM)	4
	Ion Spectrometry Experiment (CIS)	4
Genesis	Genesis Ion Monitor (GIM)	150
SOHO	Celias/Proton Monitor (PM)	30

The columns of Table 2 contain components of the normal vector to these FFSs, solar wind speed in the direction of the normal towards a given shock, and the calculated speed of the shock (according to Kasper, 2005). The last but one column shows the velocity of disturbance inside the Earth's magnetosphere calculated from the timing of observations in the dayside magnetosphere using the satellites pair indicated in the last column. The velocity was calculated in the direction of the propagation of the original shock in the solar wind, assuming conservation of its planar front. We took the very first signatures of the disturbance front in the magnetosphere as the decisive moments for the speed calculation and thus v_{MS} represents the upper limit for the speed value.

Comparing columns v_{sh} and v_{MS}, it is clear that the calculated speed of the wave inside the Earth's magnetosphere is higher than the speed of shocks in the solar wind. Kasper (2005) used eight different methods to compute the normals. His application of the Rankine–Hugoniot method leads to the most consistent results. Uncertainties of the shock speeds are approximately ± 10 km/s. While in the solar wind rapid fronts (tens of seconds) of the FF shocks in magnetic fields and plasma parameters are observed, the shock disturbances in the Earth's dayside magnetosphere exhibit much slower compressions of the magnetic field lasting several minutes (3–5 min), as measured by the Polar, GOES-8, GOES-9, GOES-10, and Cluster satellites at various places. We will show that this is not always true with good time resolution data.

We did not find any case which could be completely in agreement with the simulations made by Guo et al. (2005) for their oblique case. The events shown in Table 2 are similar to their case number one by topology (shock propagation parallel to the Sun–Earth line) and we will do a comparison later.

We would like to describe two of the selected cases in broader detail. On November 9th, 2002, the Wind satellite observed two interplanetary shocks in sequence after 17:24 UT and 18:27 UT. The corresponding components of the shock normal vector were (−0.99, 0.15, −0.05) and (−0.98, −0.03, −0.20) in the GSE system. The θ_{Bn} angle was ~43° and 70°, the compression ratio 1.69 and 2.01, respectively.

The IMF was Parker-spiral-like and B_Z positive both upstream and downstream of these events ($\theta \approx 30$–$60°$, $\phi \approx 130°$). The situation is depicted in Figs. 1 and 2 for the two events. During that time, the satellites SOHO, ACE, Genesis, and Geotail were also operating in the solar wind, while the geosynchronous GOES-8 and GOES-10 satellites were in the Earth's magnetosphere. The Cluster spacecraft constellation was situated on the night side in the dusk flank

Table 2
List of the selected fast forward shocks (observed by Wind)

Date	UT	$\vec{R}[R_E]$	$\vec{n}$	v_n	v_{sh}	v_{MS}	S/C
1999 09 15	20:08:40	(69.7, −34.8, −2.8)	(−0.83, −0.16, 0.53)	400	668	457	G8–Po
2001 10 11	16:50:55	(59.4, −65.8, 7.1)	(−0.99, 0.04, 0.01)	356	583	811	G8–Cl
2001 11 19	18:15:31	(−0.20, −72.36, 5.74)	(−0.98, 0.10, −0.14)	421	628	1270	G10–Cl
2002 08 18	18:40:55	(49.3, 75.3, 5.3)	(−0.96, 0.06, 0.29)	404	673	625	G8–Cl
2002 11 09	17:24:49	(96.7, −29.7, 5.5)	(−0.99, 0.15, −0.05)	336	380	590	G8–Cl
						588	G8–Po
2002 11 09	18:27:49	(96.7, −29.7, 5.5)	(−0.98, −0.03, −0.20)	351	425	741	G8–Cl
						714	G8–Po

Speed units are km/s and the position of the Wind satellite and shock normal vectors are in the GSE coordinate system. v_n is the upstream solar wind speed along the direction of the shock normal, v_{sh} is the calculated speed of the shock (from Kasper (2005)), v_{MS} denotes the calculated speed of disturbance (see text) inside the Earth's magnetosphere based on the spacecraft indicated in the last column (G8 ≡ GOES-8, G10 ≡ GOES-10, Po ≡ Polar, Cl ≡ Cluster SC1).

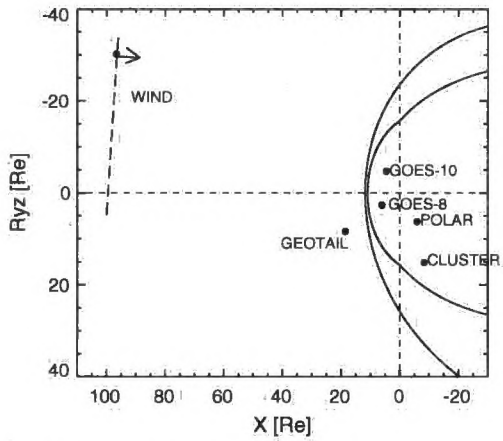

Fig. 1. November 9th, 2002 event: positions of given satellites for the first event observed by Wind at 17:24 UT. The dashed line indicates the interplanetary shock front. The Jeřáb et al. (2005) and Petrinec and Russell (1996) models were used to determine the bow shock and magnetopause positions before the shock arrival. R_{yz} denotes the distance from the X axis, distinguishing the dawn/dusk sides (sign of Y), $R_{yz} = \mathrm{sign}(y) \cdot \sqrt{y^2 + z^2}$.

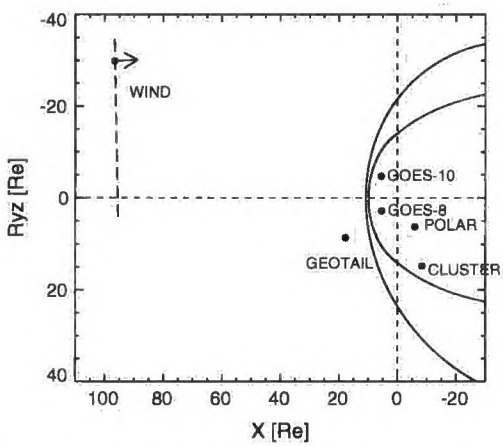

Fig. 2. November 9th, 2002 event: positions of given satellites for the second event observed by Wind at 18:27 UT. R_{yz} has the same meaning as in the previous figure.

plasma sheet near the magnetopause before the events. It orbited behind the quasiperpendicular part of the bow shock, so we don't expect any foreshock effects there.

Interplanetary magnetic field data and plasma parameters from selected far solar wind monitors are plotted in Fig. 3a, while similar data from Geotail (located in the bow shock vicinity) are depicted in Fig. 3b. Besides the two fast forward shock events seen by Geotail at 17:47:50 UT and 18:46:08 UT, there was another discontinuity registered by Geotail at 19:00:46 UT. Small jumps in the magnetic field magnitude and proton speed, and a decrease of density and temperature (not shown) lead us to conclude that this event is a weak reverse slow shock. The discontinuity brought some dynamic pressure relief on the magnetosphere delayed about 14 min after the compression by the second fast forward shock. However, Wind observations show the discontinuity was much weaker at 18:44:09 UT, so its influence is questionable.

Magnetospheric data are presented in Fig. 4a,b. All satellites in the solar wind and the satellites GOES-8 and GOES-10 in the magnetosphere registered both events as distinct jumps of the B_Z magnetic field component and total magnetic field strength (see Tables 3 and 4), while only the second event is easily discernible in Cluster SC1 data (Fig. 4b). Polar located in the nightside magnetosphere registered the events only as a weak increase of the magnetic field magnitude and plasma density. At least four periods of quasiharmonic global resonances with about 12 min repetition can be found in both the magnitude and B_Z magnetic field component from GOES-8 and GOES-10 after 19:00 UT, but not at Cluster.

During the first event, only a small increase in the ion density and velocity, and higher-frequency fluctuations in the magnetic field can be seen, as demonstrated in Cluster SC1 CIS data in Figs. 4b and 5. The most discernible features are damped periodic ion velocity oscillations (period about 11 min) started by the first disturbance passage and lasting at least 1 h (practically till the second disturbance arrival).

The second event resulted in the LLBL inner boundary crossing of Cluster SC1 at 18:53:10 UT. Detailed investigation of CIS data in Fig. 5 shows a drop of the ion energy and an increase of the ion velocity $-v_x$ component at 18:51:00 UT (i.e., approximately 2 min earlier). We consider this as the first attribute of the incoming shock disturbance.

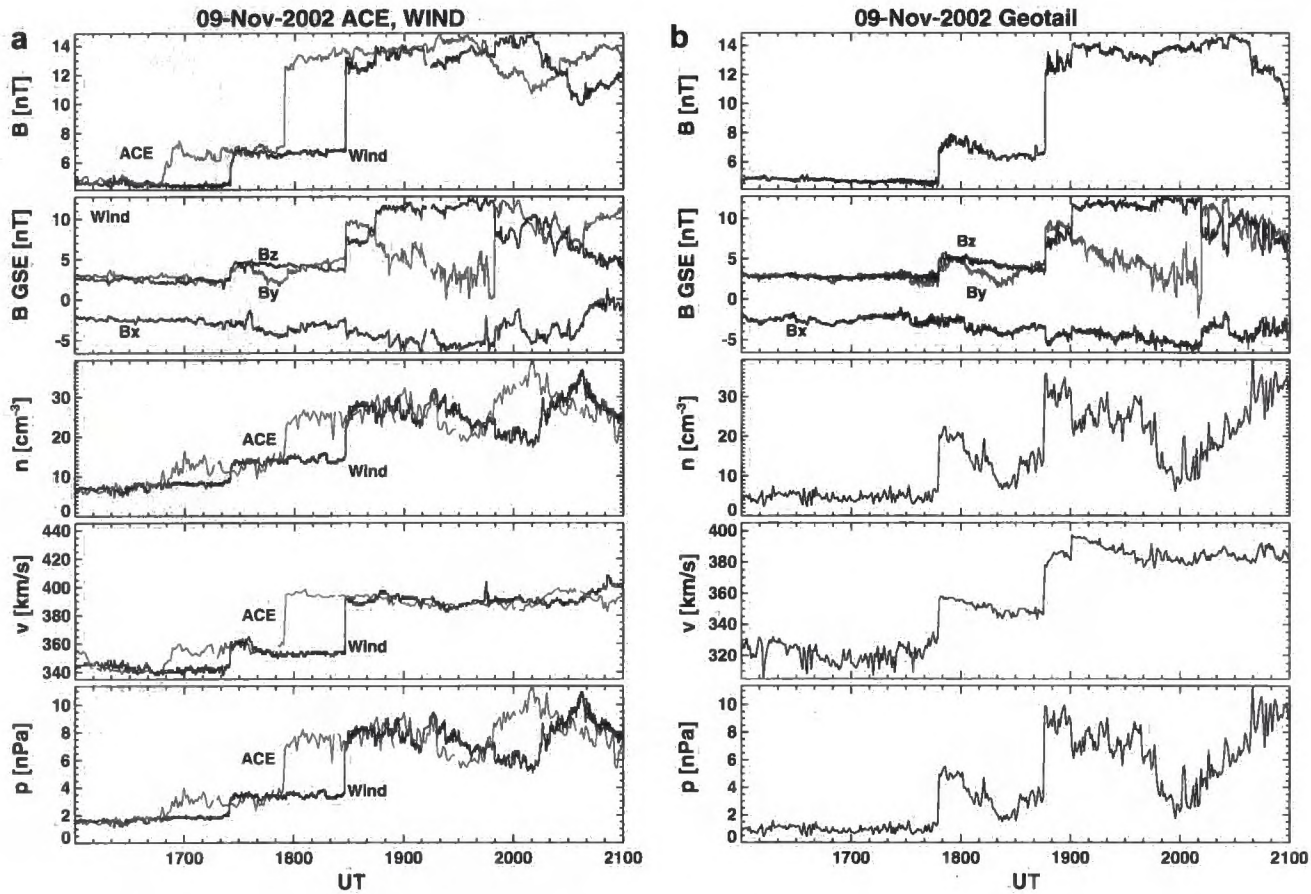

Fig. 3. November 9th, 2002 event. (a) Magnetic field magnitude and components (Wind only), proton density and speed, and the solar wind dynamic pressure from the satellites ACE and Wind located far in the solar wind. (b) Observations of the same solar wind parameters from the Geotail satellite close to the bow shock. The bottom three panels show the CPI instrument data.

Detailed comparison of the two shock fronts as registered by the near-Earth spacecraft is provided in Fig. 6. Both shock fronts at Geotail last about 10 s. From the high-resolution data, two parts of the fronts on the GOES spacecraft can be distinguished. First, there are slow 3–5 min long ramps, already reported elsewhere. On top, at the beginning of them, there are very fast step-like fronts taking about one half of the total field compression. They last about 10 s – the same time as the original shock fronts seen in the solar wind by Geotail, and they are mainly caused by the increase of the H_p (northward) component at GOES-8. A small decrease of the magnitude follows after this fast front, similarly as in the simulation case 1 by Guo et al. (2005). The second part of fronts starts by a steep (~30 s) decrease of the H_e (earthward) component and continuing increase of the H_p component. No such double-part structure is seen in the Geotail data. During the first event, the Cluster fleet saw large fluctuations of the magnetic field magnitude (see also Fig. 4b). At the moment of the passage of the disturbance after 17:53 UT, their frequency increased and the first leading front is again quite fast (about 30 s, not resolved at SC2). During the second event (after 18:52 UT), a wide ramp is seen by all Cluster spacecraft lasting up to 7 min (at SC2).

Tables 3 and 4 show locations of particular satellites and arrival times for both events. Here we took the beginning of the fast ramp of the magnetic field compressions in GOES data as the arrival time of the fastest waves constituting the disturbance. The speed of disturbances was calculated along the direction of the propagation of the original shock in the solar wind. Higher calculated values mean that the given shock signatures propagated faster in the magnetosphere than shocks seen by the Wind satellite.

At 17:25 UT, the speed of the shock was 380 km/s, at 18:28 UT the shock speed was 425 km/s, according to the Wind data. Also, the second IP shock was stronger than the first one according to Kasper (2005) (compression ratios 1.69 and 2.01, respectively). From timing of observed disturbances in the magnetosphere based on the GOES-8 and Cluster SC1 (Polar) satellites, we determined the speed of the disturbance fronts as 590 (588) km/s and 741 (714) km/s, for the two events, respectively. If we calculate this speed again for the second case, but taking the Cluster SC1 LLBL inner boundary crossing (about 130 s later) as the arrival time, we get a smaller value, 344 km/s (381 km/s for the Geotail—Cluster SC1 pair).

We also estimated the time when the two shocks touched the magnetopause for the first time. We used the

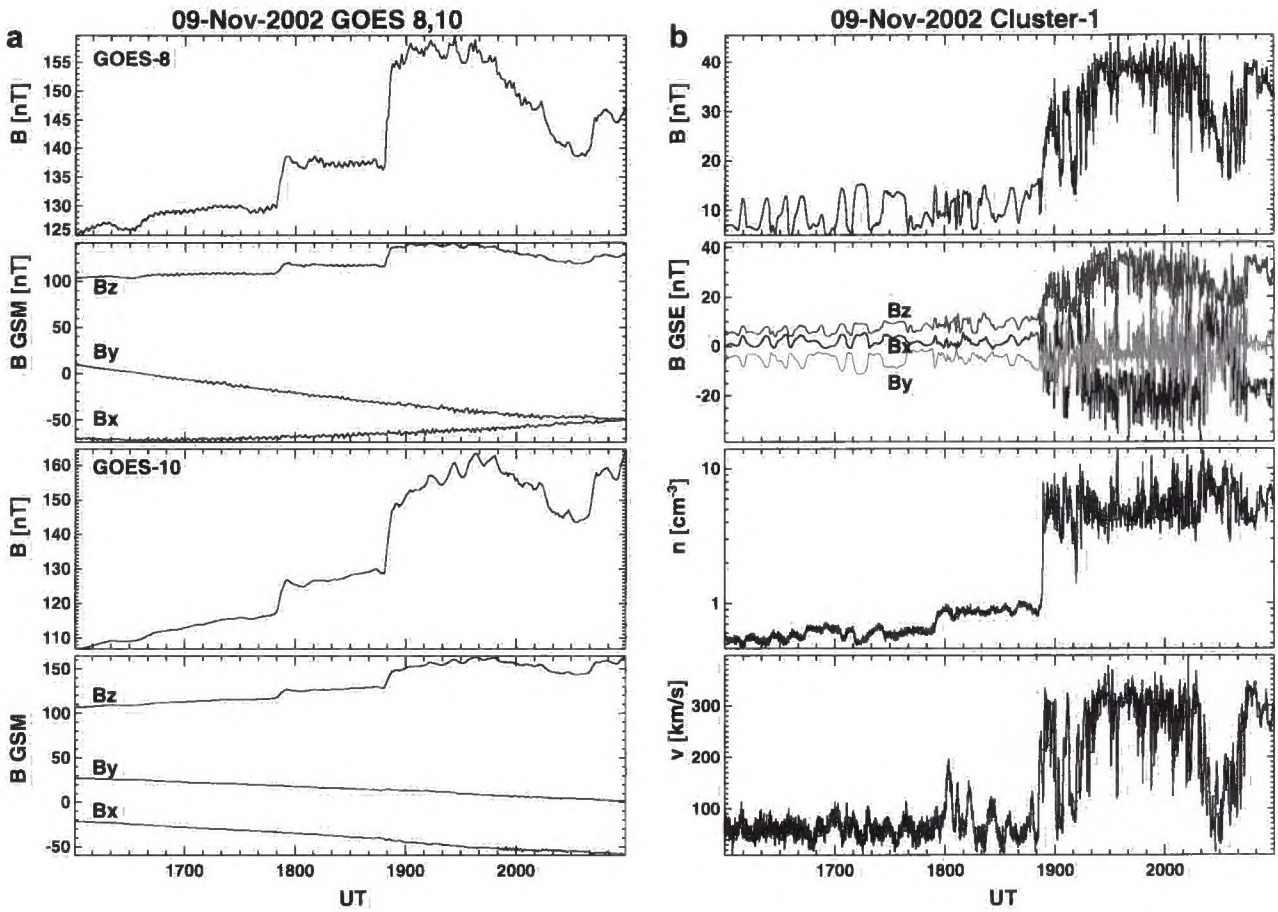

Fig. 4. November 9th, 2002 event. (a) Observations of the magnetic fields from the geosynchronous satellites GOES-8 and GOES-10 in the GSM coordinates. (b) Cluster SC1 primary parameters. The top two panels show the magnetic field, next two panels plot the ion density and speed.

Table 3
Satellite locations in GSE coordinates and arrival times/compression onsets for the first shock on November 9th, 2002

Satellite	X [Re]	Y [Re]	Z [Re]	Arrival time, UT	Region
SOHO	241.3	−82.0	14.3	16:42:36	SW
ACE	229.9	40.9	−17.0	16:48:10	SW
Genesis	186.9	−1.5	−1.5	16:59:00	SW
Wind	96.4	−29.9	5.5	17:24:49	SW
Geotail	18.55	8.13	1.92	17:47:50	SW
GOES-8	6.06	1.25	2.32	17:50:34	MS
GOES-10	4.62	−4.72	0.06	17:50:38	MS
Polar	−5.9	6.0	1.7	17:52:50	MS
Cluster SC1	−8.60	13.8	4.43	17:53:30	MS
–	11.4	−1.2	0.6	17:49:29	MP

The last line shows the estimated arrival of the IP shock to the magnetopause. SW – solar wind, MS – magnetosphere.

Table 4
Satellite locations in GSE coordinates and arrival times/compression onsets for the second shock on November 9th, 2002

Satellite	X [Re]	Y [Re]	Z [Re]	Arrival time, UT	Region
SOHO	241.2	−82.1	14.2	17:55:56	SW
ACE	229.9	41.0	−17.0	17:54:12	SW
Genesis	186.9	−1.5	−1.5	18:07:00	SW
Wind	96.6	−29.9	5.5	18:27:49	SW
Geotail	17.76	8.63	1.76	18:46:08	SW
GOES-8	5.41	2.8	2.56	18:49:07	MS
GOES-10	5.57	−3.48	0.73	18:49:13	MS
Polar	−5.55	5.2	2.2	18:50:40	MS
Cluster SC1	−8.62	14.34	3.93	18:51:00	MS
–	9.4	0.3	−1.9	18:48:29	MP

The estimated arrival of the shock to the magnetopause in the last line. SW – solar wind, MS – magnetosphere.

Petrinec and Russell (1996) model of the magnetopause position and the Geotail magnetic field and solar wind dynamic pressure measured in front of the shocks. We considered the planar shocks and no deceleration in the magnetosheath. Using these estimations, we got the average speed of the compressional wave front from the magnetopause to GOES-8 (GOES-10) 550 (578) km/s and 671 (483) km/s for the two shocks, respectively. The speeds are slower than the dayside/nightside speeds evaluated above.

4. Discussion

We studied fast forward shocks and their manifestation in the Earth's magnetosphere. The results are summarized

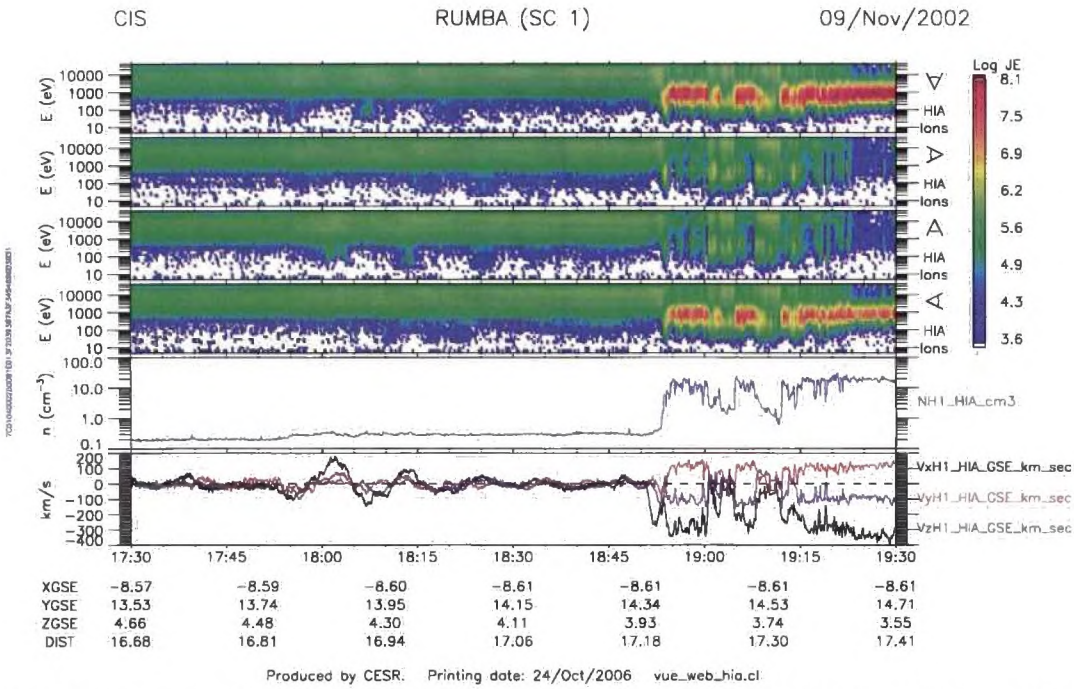

Fig. 5. November 9th, 2002 event: Data plot of the CIS experiment onboard Cluster SC1. The top 4 panels show spectrograms from the HIA sensor, for ions arriving in the 90° × 180° sectors with a field-of-view pointing in the Sun, dusk, tail, and dawn directions, respectively (in particle energy flux: keV/(cm^2 s sr keV)). The next two panels show the ion density and ion bulk velocity.

in three tables. Table 2 presents cases chosen according to Wind satellite observations (Kasper, 2005) and calculated shock speeds and components of normal vectors. Propagation speeds of given disturbances in the Earth's magnetosphere along the IP shock normal were calculated from pairs of satellites inside the Earth's magnetosphere. Tables 3 and 4 present the shock observation times determined using the fleet of satellites. The front length is usually less than 30 s in the solar wind, but the duration of the plasma parameter change for the related disturbance inside the Earth's magnetosphere is about 3–5 min, which is comparable with the propagation time of the disturbance in the dayside magnetosphere.

For the two events from November 9th, 2002 we found a very steep initial part of the magnetic field compression in the GOES high-resolution data, with practically the same duration as the shock fronts in the solar wind, followed by a second much slower part. This double-part structure can have several explanations. Either we see the original non-degraded shock in the magnetosphere, which may be followed by a reverse-going rarefaction wave reflected from the denser regions near the Earth, and then the compression slowly continues as the shock passes around the magnetosphere (see e.g., Takeuchi et al. (2002) for ramp duration model). This explanation can be supported by the results of numerical simulations (Guo et al., 2005; Ridley et al., 2006), but its timing seems to be questionable for our case. Unfortunately, missing plasma observations do not allow us to better describe the front structure and to verify this statement. The second explanation would be that the double-part structure has been already created by the interaction of the interplanetary shock within the bow shock–magnetopause system and then it is swept into the magnetosphere. We have already seen similar double-step profiles in the density and magnetic field during the passage of IPS through the magnetosheath (Šafránková et al., accepted for publication; Samsonov et al., 2006). Another explanation was given by Russell et al. (1999), who also observed a similar very rapid front of the magnetic field strength at dayside geosynchronous orbit and explained it simply by forming a shock-like feature when the compressional waves slow below the speed of the interplanetary disturbance in the denser dayside magnetosphere. The Magnetospheric Plasma Analyzer onboard the LANL 1990 geosynchronous satellite (during our events at ~14:30–15:30 MLT) reported the partial density of low energy ions about 10 cm^{-3} which gives too high Alfven speed to justify the steep magnetic field front only by the last explanation.

The propagation speeds inside the magnetosphere are significantly higher than speeds of fast forward shocks calculated from the Wind satellite in the solar wind. Our results generally agree with estimates by Wilken et al. (1982) and Nopper et al. (1982), about 600–1500 km/s: our compressional front speeds (about 600–700 km/s for the events on November 9th, 2002) are similar to their lower values representing the radial inward motion, but are smaller than their values for the azimuthal/near-geostationary-orbit propagation. The difference may be caused by a diverse state of the magnetosphere and content of plasma (mainly the density of plasma near and outside the geostationary orbit): in the Wilken et al. (1982) case, the preshock

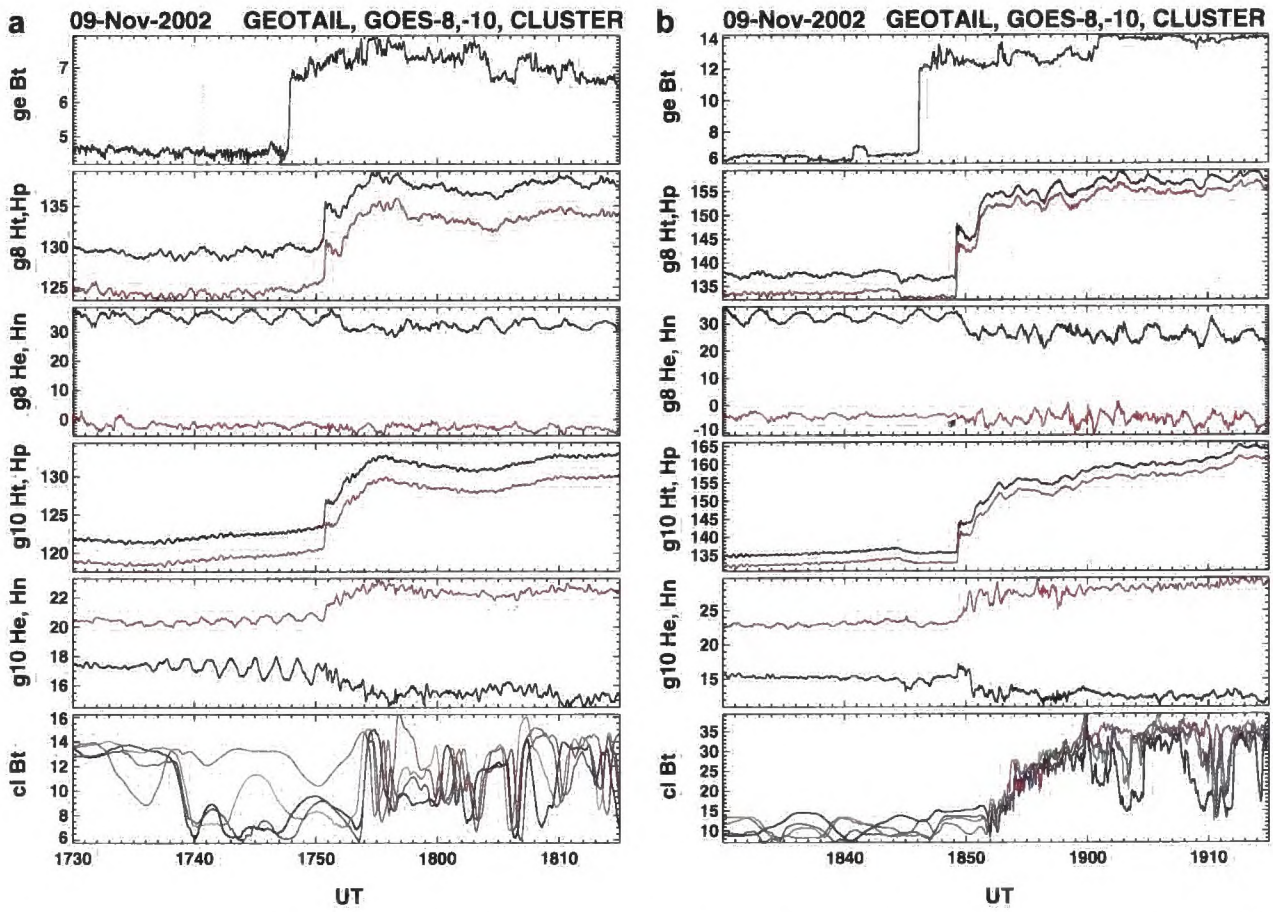

Fig. 6. November 9th, 2002 events in detail. (a) Shock at 17:50 UT, (b) Shock at 18:50 UT. The top panel shows the magnitude of IMF as measured by Geotail. The next two panel pairs depict the GOES-8 and GOES-10 high-resolution magnetic field data in local S/C coordinates (H_t magnitude, H_p northward component (in red), H_e earthward component, H_n normal to both H_p and H_e, eastward (in red)). The bottom panel plots the magnitude of magnetic fields measured by the Cluster SC1 (black), SC2 (red), SC3 (green), and SC4 (blue). All panels in nT units.

magnetopause had been already compressed near to the geosynchronous orbit (subsolar magnetopause at about $R_0 \sim 7.8R_E$). Likewise we got higher speed for the second event when the magnetopause was initially closer to the Earth ($R_0 \sim 9.7R_E$) than before the first event ($R_0 \sim 11.7R_E$). We also got slightly higher values for the propagation speed to Cluster (significant at least in the second event) that was farther from the Earth than Polar. On the other hand, the higher speed for the second event may be supported by the faster and stronger interplanetary shock actuating along the magnetopause.

The cases from Table 2 are hardly comparable from the point of view of the satellite configuration and the magnetosphere state and thus do not give decisive answer on the importance of IP shock properties on the disturbance propagation speed in the magnetosphere. Examination of more cases is in progress to enable some statistical study of the dependence of disturbance propagation speed on various factors.

On November 9th, 2002, Cluster, which was near the flank nightside magnetopause, sensed the disturbance front moving through the magnetosphere about 2 minutes earlier than the constellation encountered the LLBL boundary as a signature of the magnetopause movement. Also recent global MHD simulations (Ridley et al., 2006) show a significant deformation and outrun of the interplanetary shock front in the magnetosphere. On the other hand, Koval et al. (2005); Koval et al. (2006) show the IP shock retardation in the magnetosheath flanks near the magnetopause, according to both observations and simulation. From this, a considerable refraction of the interplanetary shock front is expected along the nightside magnetopause.

In our study, we assumed planar interplanetary shocks and we expected no change during their propagation in the solar wind. The used shock normal directions may affect our speed calculations. Determinations of shock normals in the solar wind were made by different methods. For the presented events, we used the Rankine–Hugoniot method results (Kasper, 2005), based on the local Wind data. Uncertainty of these results is dependent on chosen intervals of upstream and downstream plasma parameters and magnetic fields and the time resolution of available data. Deviations of the shock speeds are usually less than 10 km/s and errors of the shock normal direction are 5°–10°. Kasper (2005) used eight methods to compute the normals. Among them, the R–H method led to the most

Nopper Jr., R.W., Hughes, W.J., Maclennan, C.G., McPherron, R.L. Impulse-excited pulsations during the July 29, 1977, event. J. Geophys. Res. 87, 5911–5916, 1982.

Petrinec, S.M., Russell, C.T. Near-Earth magnetopause shape and size as determined from the magnetopause flaring angle. J. Geophys. Res. 101, 137–152, 1996.

Ridley, A.J., De Zeeuw, D.L., Manchester, W.B., Hansen, K.C. The magnetospheric and ionospheric response to a very strong interplanetary shock and coronal mass ejection. Adv. Space Res. 38, 263–272, doi:10.1016/j.asr.2006.06.010, 2006.

Russell, C.T., Zhou, X.W., Chi, P.J., Kawano, H., Moore, T.E., Peterson, W.K., Cladis, J.B., Singer, H.J. Sudden compression of the outer magnetosphere associated with an ionospheric mass ejection. Geophys. Res. Let. 26, 2343–2346, 1999.

Russell, C.T., Wang, Y.L., Raeder, J., Tokar, R.L., Smith, C.W., Ogilvie, K.W., Lazarus, A.J., Lepping, R.P., Szabo, A., Kawano, H., Mukai, T., Savin, S., Yermolaev, Y.I., Zhou, X.-Y., Tsurutani, B.T. The interplanetary shock of September 24, 1998: arrival at Earth. J. Geophys. Res. 105, 25143–25154, 2000.

Šafránková, J., Němeček, Z., Přech, L., Samsonov, A.A., Koval, A., Andréeová, K. Modification of interplanetary shocks near the bow shock and through the magnetosheath. J. Geophys. Res., accepted for publication, doi:10.1029/2007JA012503.

Samsonov, A.A., Němeček, Z., Šafránková, J. Numerical MHD modeling of propagation of interplanetary shock through the magnetosheath. J. Geophys. Res. 111, A08210, doi:10.1029/2005JA011537, 2006.

Spreiter, J.R., Stahara, S.S. Gasdynamic and magnetohydrodynamic modeling of the magnetosheath: a tutorial. Adv. Space Res. 14, 5–19, 1994.

Szabo, A., Lepping, R.P., Merka, J., Smith, C.W., Skoug, R.M. The evolution of interplanetary shocks driven by magnetic clouds. In: Battrick, B., Sawaya-Lacoste, H., Marsch, E., Martinez Pillet, V., Fleck, B., Marsden, R. (Eds.), Solar encounter. Proceedings of the First Solar Orbiter Workshop. ESA SP-493. pp. 383–387. 2001.

Takeuchi, T., Russell, C.T., Araki, T. Effect of the orientation of interplanetary shock on the geomagnetic sudden commencement. J. Geophys. Res. 107, 1423, doi:10.1029/2002JA009597, 2002.

Tamao, T. The structure of three-dimensional hydromagnetic waves in a uniform cold plasma. J. Geomagn. Geoelectr. 18, 89–114, 1964.

Villante, U., Lepidi, S., Francia, P., Bruno, T. Some aspects of the interaction of interplanetary shocks with the Earth's magnetosphere: an estimate of the propagation time through the magnetosheath. J. Atm. Solar-Terr. Phys. 66, 337–341, doi:10.1016/j.jastp.2004.01.003, 2004.

Wilken, B., Goertz, C.K., Baker, D.N., Higbie, P.R., Fritz, T.A. The SSC on July 29, 1977 and its propagation within the magnetosphere. J. Geophys. Res. 87, 5901–5910, 1982.

Yan, M., Lee, L.C. Interaction of interplanetary shocks and rotational discontinuities with the Earth's bow shock. J. Geophys. Res. 101, 4835–4848, 1996.

Zhuang, H.C., Russell, C.T., Smith, E.J., Gosling, J.T. Three-dimensional interaction of interplanetary shock waves with the bow shock and magnetopause – A comparison of theory with ISEE observations. J. Geophys. Res. 86, 5590–5600, 1981.

Appendix C

Attached article

[**A2**] **Andreeova, K.**, T. I. Pulkkinen, T. V. Laitinen, L. Prech (2008), Interaction of interplanetary shocks with the Earth's magnetosphere: Observations and global MHD simulations compared during the Nov 9, 2002 event, accepted to *J. Geophys. Res.*.

Shock propagation in the magnetosphere: Observations and MHD simulations compared

K. Andreeova[1], T. I. Pulkkinen[2], T. V. Laitinen[2,3], L. Prech[1]

Abstract. We examine the propagation of disturbances in the Earth's magnetosphere caused by fast forward shock interaction with the magnetopause. Our statistical study as well as event analyzes show that the propagation speeds are larger in the magnetosphere than in the solar wind, and larger in the nightside magnetosphere than in the dayside magnetosphere. A case study of a double shock during November 9, 2002 is examined both observationally and using the GUMICS-4 global MHD simulation. Tracing the disturbance propagation allows us to confirm that the MHD simulation results are in a good agreement with the in-situ observations. The simulation results show that the propagation of the disturbance occurs in the antisunward direction, simultaneously at all clock angles. However, changes in the magnetosheath are largest at high latitudes, while in the magnetotail the largest variations are seen in the plasma sheet.

1. Introduction

Interplanetary shocks (IPS) propagate in the solar wind at almost constant speed and, as they arrive at Earth orbit, interact with the Earth's magnetosphere. During the interaction, the shocks cause compression and/or expansion of the magnetosphere and modify the magnetopause position and tail currents. On ground, these processes are associated with sudden impulses, sometimes called sudden commencements [*Le et al.*, 1998; *Le and Russell*, 1998; *Zhuang et al.*, 1981].

Interplanetary shocks are mainly driven by two sources, coronal mass ejections (CME) and corotating interaction regions (CIR). Even though several authors have shown that the surface of the interplanetary shocks can be rather curved at larger distances [*Szabo et al.*, 2001], in our study it is sufficient to assume that the shock fronts are planar, as the interplanetary shocks interacting with the magnetosphere are large in comparison to the size of the magnetosphere.

Interplanetary shocks can be classified to four types according to the associated changes in the solar wind plasma and interplanetary magnetic field [*Burlaga*, 1971]: Fast forward, fast reverse, slow forward, and slow reverse shocks. In our study, we concentrate on fast forward shocks (FFS), which propagate antisunward toward the Earth with speed of about 50–200 km/s in the reference frame of the ambient plasma [*Berdichevsky et al.*, 2000].

Fast forward shocks interact with the Earth's bow shock, magnetosheath and magnetopause. These interactions have been studied by several authors using gasdynamic and magnetohydrodynamic (MHD) models or Rankine-Hugoniot conditions [*Spreiter and Stahara*, 1994; *Grib et al.*, 1979; *Grib*, 1982; *Zhuang et al.*, 1981]. After interaction with the interplanetary shock, the bow shock is modified and moves earthward. Even though the shock front in the solar wind is considered to be planar, in the magnetosheath the front becomes curved near the flanks of the magnetotail [*Koval et al.*, 2005, 2006]. The shock deceleration in the magnetosheath has been estimated both by observational and simulation techniques to range from about one third to about a quarter of the original shock speed [*Koval et al.*, 2005; *Villante et al.*, 2004]. A time delay of about 5 minutes was found from interaction at the bow shock to observation of the disturbance on ground [*Villante et al.*, 2004]. According to the MHD simulation results [*Samsonov et al.*, 2006], after the interaction with the bow shock the FFS shock in the magnetosheath is followed by a discontinuity that was identified as a close combination of three discontinuities. They propagate with nearly the same speeds, but these speeds are lower than that of the IP shock. Observationally, such a discontinuity was examined by *Šafránková et al.* [2007] and its speed determined in a case study by *Prech et al.* [2008].

Guo et al. [2005] showed that the shock orientation is significant for the disturbance propagation in the magnetosphere: They performed a global numerical MHD simulation of the interaction between a FFS and the Earth's magnetosphere. They compared two FFSs with the same solar wind dynamic pressure and Z-component of interplanetary magnetic field (IMF) but with two different shock normal orientations, one parallel to the Sun-Earth line and the other oblique. In both cases, the shock caused compression of the magnetosphere. For the parallel case, the compression lasted about one minute at geostationary orbit near local noon. The ramp was split into two phases with a small decrease in the middle. The second, oblique case was similar to the first one, but it lasted five minutes. Similar double structure has been found by numerical simulations by *Ridley et al.* [2006].

In the magnetosphere, the fast mode wave and Alfvén wave velocities are higher than in the surrounding solar wind. The FFS is associated with a sudden increase of the solar wind dynamic pressure. When it reaches the magnetopause, the magnetopause starts to get compressed and moves earthward, which leads to launching of different types of waves within the magnetosphere: *Tamao* [1964] found isotropic compressional hydrodynamic waves generated at the magnetopause, propagating inward into the magnetosphere at speeds somewhat higher than the local Alfvén wave speed. *Wilken et al.* [1982] estimated the propagation speeds to be about 600 km/s in the radial direction from geostationary orbit to ground, and about 910 km/s in the azimuthal direction in the equatorial plane. Finally, *Nopper et al.* [1982] estimated an impulse disturbance speed of about 1500 km/s at geostationary orbit.

Recently, *Samsonov et al.* [2007] used the global BATS-R-US MHD code to simulate the interaction of a moderately strong interplanetary shock propagating along the Sun-Earth line with the magnetosphere and a 1D MHD code to study its interaction with plasmapause/plasmasphere. The authors showed that the fast shock reflected from the global code inner boundary. The second simulation suggests that such reflection occurs mainly at the dayside ionosphere rather than plasmapause. In their simulation, the reflected fast shock plays an important role in the magnetospheric boundary dynamics, as it terminates the magnetopause inward movement and reverse the movement of the bow shock. The global simulation predicted also a secondary fast compressional wave moving

[1]Charles University Prague, Czech Republic
[2]Finnish Meteorological Institute, Helsinki, Finland
[3]Now at: Swedish Institute for Space Physics, Uppsala, Sweden

0148-0227/08/2008JA013350$9.00

between magnetopause and the inner boundary. From their simulation an average speed of the primary and reflected fast shocks in the magnetosphere can be estimated about 700 km/s in agreement with their assumptions of mean Alfven velocity in outer dayside magnetosphere 1000 km/s and in the plasmasphere 500 km/s. The results of this simulation also help to interpret high-time resolution geosynchronous magnetic field observations by *Andreeova and Prech* [2007] during two events recorded on November 9, 2002 and studied also later in this paper.

The large number of spacecraft operating in the Earth's magnetosphere during last decade allow us to pursue studies that follow in detail the propagation and evolution of dynamic events in the magnetosphere. In this paper, we study a large number of FFS events and follow the disturbance in different parts of the magnetosphere. However, since even with this fleet, the number of observation points is limited, we use the global MHD simulation GUMICS-4 [*Janhunen*, 1996] to follow the propagation of the shock and related discontinuities at all locations throughout the November 9, 2002 events.

2. Data sources

We have selected FFS events from the interplanetary shock database compiled by Kasper (Kasper, J. C., Interplanetary shock database from WIND satellite, http://space.mit.edu/home/jck/shockdb/shockdb.htm, 2005) and from the SOHO database (Interplanetary shocks and other interesting events from SOHO satellite, http://umtof.umd.edu/pm/figs.html, 2007).

For verification and comparison we calculated shock parameters, such as shock normals and speeds, using methods utilizing four spacecraft measurements and the Rankine-Hugoniot (RH) equations (e.g. *Szabo* [1994]):

$$
\begin{aligned}
\Delta[G_n] &\equiv \Delta[\rho(V_n - V_S)] = 0 \\
\Delta[B_n] &\equiv \Delta[\mathbf{B}\cdot\hat{n}] = 0 \\
\Delta[\mathbf{S_t}] &\equiv \Delta\left[\rho(V_n - V_S)\mathbf{V_t} - \frac{B_n}{\mu_0}\mathbf{B_t}\right] = 0 \\
\Delta[\mathbf{E_t}] &\equiv \Delta[(\hat{n}\times\mathbf{V_t})B_n - (V_n - V_S)(\hat{n}\times\mathbf{B_t})] = 0 \\
\Delta[S_n] &\equiv \Delta\left[P + \frac{{B_t}^2}{2\mu_0} + \rho(V_n - V_S)^2\right] = 0 \\
\Delta[\varepsilon] &\equiv \Delta\left[\rho(V_n - V_S)\left(\frac{(\mathbf{V} - V_S\hat{n})^2}{2} + \frac{\gamma}{\gamma-1}\frac{P}{\rho} + \frac{B^2}{\mu_0\rho}\right)\right. \\
&\quad \left. - \frac{B_n(\mathbf{V} - V_S\hat{n})\cdot\mathbf{B}}{\mu_0}\right] = 0
\end{aligned}
$$

where V_S is the shock speed along the normal, $\mathbf{V}$ and $\mathbf{B}$ are the plasma bulk velocity and the magnetic field, γ is the ratio of specific heats, μ_0 is the vacuum permeability, ρ is the mass density, $P = nkT$ is the total scalar isotropic thermal pressure, and $\hat{n}$ is the shock normal unit vector. The subscripts n and t refer to the normal and tangential components of the above quantities. The variables G_n, B_n, $\mathbf{S_t}$, $\mathbf{E_t}$, S_n, and ε denote the conserved quantities across the shock, the mass flux, normal magnetic field, tangential momentum flux, tangential electric field, normal momentum flux, and energy flux. The notation $\Delta[]$ refers to the difference across the shock.

The four-spacecraft timing method was used if data were available from at least 4 spacecraft in the solar wind. We used satellite positions and times of the shock passage to determine normal direction and propagation speed $\mathbf{r}_{\alpha\beta}\cdot\mathbf{n} = V_d\cdot t_{\alpha\beta}$, where $\mathbf{r}_{\alpha\beta}$ is the separation vector between two satellites α and β, and $t_{\alpha\beta}$ is the time difference between the observations. V_d is the propagation speed.

For investigation of the interaction of the IPS with the Earth's magnetosphere, we have used simultaneous plasma and magnetic field data from GOES-series [*Singer et al.*, 1996], Polar [*Russell et al.*, 1995; *Harvey et al.*, 1995], Geotail [*Kokubun et al.*, 1994; *Mukai et al.*, 1994], Cluster [*Balogh et al.*, 1997; *Reme et al.*, 1997], Wind [*Lepping et al.*, 1995; *Ogilvie et al.*, 1995; *Lin et al.*, 1995], and ACE [*Smith et al.*, 1998; *McComas et al.*, 1998]. The spacecraft provided data in the solar wind, magnetosheath, and in the magnetosphere.

3. GUMICS-4 global MHD simulation

The GUMICS-4 global magnetohydrodynamic (MHD) simulation solves the ideal MHD equations to provide the self-consistent temporal and spatial evolution of the plasma dynamics in the magnetosphere and the solar wind [*Janhunen*, 1996]. The fully conservative MHD equations are solved in a simulation box extending from 32 R_E upstream of the Earth to $-224R_E$ in the tailward direction and ± 64 R_E in the directions perpendicular to the Sun-Earth line. The equations are solved in the geocentric solar ecliptic (GSE) coordinates. The inner boundary of the MHD domain is a spherical shell with a radius of 3.7 R_E, which maps along the dipole field to about 60° latitude. The MHD grid is adaptive in a sense that the grid is automatically refined to a minimum cell size of 0.25 R_E whenever the code detects large spatial gradients. Furthermore, the code uses subcycling in order to save computation time, i.e., the time step varies dynamically with the local travel time of the fast magnetosonic wave across the grid cell [*Janhunen*, 1996]. Solar wind density, temperature, velocity, and magnetic field are given as boundary conditions along the sunward boundary while supersonic outflow conditions are applied on the other boundaries of the simulation box. It is assumed that B_X in the interplanetary field is zero

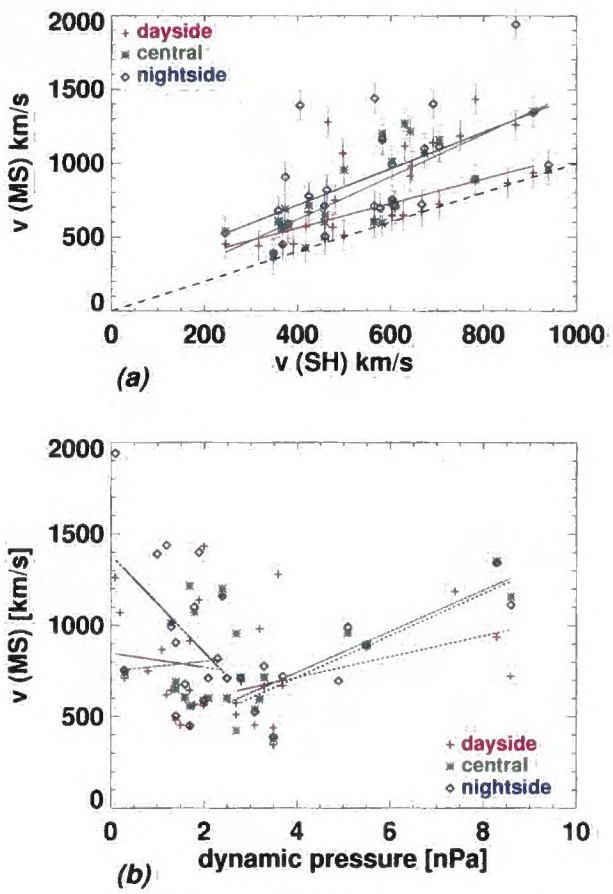

Figure 1. Statistics of shock propagation speeds: Top panel - relation of the disturbance speed in the Earth's magnetosphere to the shock speed in the solar wind. The speeds are color-coded according to the magnetospheric region: Red color denotes dayside values, green trans-terminator ("central") values, and blue color nightside values. The red, green and blue lines show linear fits to the individual observations, and the error estimates are shown by the vertical bars. Bottom panel - dependence of the disturbance speed on the dynamic pressure upstream of interplanetary shock. The red, green and blue lines lines show linear fits to these data in two pressure ranges, $P \leq 2.5$ nPa and $P \geq 2.5$ nPa.

to ensure that the field at the sunward edge of the simulation box is divergenceless.

The MHD part is coupled to an electrostatic solver of the ionospheric potential at an altitude of 110 km. The ionospheric potential is mapped to the magnetosphere along dipole field lines through a passive medium that only transmits electromagnetic effects, and where no currents flow perpendicularly to the magnetic field. The ionosphere – magnetosphere coupling loop includes mapping of the field-aligned currents and electron precipitation from the magnetosphere to the ionosphere. Precipitation from the magnetosphere is modeled as a Maxwellian population in the magnetosphere having a finite probability to fall into the loss cone. The electron precipitation is used to compute the ionospheric electron densities, which are calculated from ionization and recombination rates in several non-uniformly spaced altitude levels between about 60 and 200 km. The electron densities are then used to obtain the height-integrated Pedersen and Hall conductances at 110 km altitude. The ionospheric potential equation is solved by using the field-aligned currents from the magnetosphere as a source for the horizontal ionospheric currents. The ionospheric potential is then mapped to the inner shell of the magnetosphere, where it is used as a boundary condition for the MHD domain.

For the events studied in this paper, the simulation was run with a maximum resolution of 0.25 R_E, and the data were stored every 2.5 minutes. This study has utilized interpolated data to 1 R_E and 1 min resolution.

4. Statistical analysis

More than 40 interplanetary shock events recorded between years 1995 and 2006 were analyzed. A requirement for an event to be selected was that one of the GOES satellites was located in the dayside magnetosphere. Shock front normals were computed and disturbance speeds inside the Earth's magnetosphere were evaluated separately for the dayside and nightside magnetosphere. Shock front normals were calculated primarily using the RH method. In case of missing plasma data we used the four-spacecraft timing method. Disturbance speeds in the Earth's magnetosphere were calculated from timing of satellite observations projected to the direction of the propagation of the original FFS in the solar wind, using pairs of satellites both located within the magnetosphere. For the calculations, we have identified the times of the first signatures of the incoming disturbances.

While the shock fronts in the solar wind lasted for several tens of seconds, the duration of the disturbance fronts in the Earth's magnetosphere was about 3–5 minutes. Uncertainties of the shocks speeds are about 10 km/s. Disturbance speeds in the Earth's magnetosphere have higher errors ($\sim$ 15 %) and depend mainly on the time resolution of the observations.

Comparison of the original shock speeds in the solar wind with those in the magnetosphere revealed that the speeds inside the magnetosphere were larger and they gradually increased tailward from the subsolar magnetopause. Figure 1a shows the speeds in the dayside magnetosphere (red), across the terminator (green) and in the nightside (blue) as a function of the shock speed in the solar wind. The data show a clear ordering with the nightside speeds being higher than the dayside ones.

Figure 1b shows the correlation of the speeds in the magnetosphere with the upstream solar wind dynamic pressure. For small values of the pressure (below 2.5 nPa), the values are highly scattered but lower pressures seem to lead to higher propagation speeds. For higher pressures (above 2.5 nPa), the opposite behavior is found: Higher pressure events are associated with larger propagation speeds. It will be shown in the case study of November 9, 2002, that the disturbance speeds in the magnetosphere were higher for the second case with higher dynamic pressure (and/or higher shock speed in the solar wind).

5. November 9, 2002: A case study

The event on November, 9, 2002 comprises two fast forward shocks in sequence within one hour. The shocks were recorded by Wind at 1724 UT and 1827 UT.

Far upstream solar wind, observations were provided from ACE and Wind. More limited observations were available from Genesis and SOHO, without magnetic field, and with lower time resolution of the plasma parameters. Geotail registered the shocks in the solar wind upstream of the quasi-perpendicular Earth's bow shock, where one would not expect to see any foreshock effects. Within the magnetosphere, data were provided by GOES-8 and GOES-10 in the dayside magnetosphere, while Cluster and Polar recorded the activity in the nightside magnetosphere (for a detailed study of these events see *Andreeova and Prech* [2007]). Tables 1 and 2 gather magnetospheric spacecraft locations and the observation times.

Figure 2 shows the locations of the spacecraft during the two shock events at 1724 UT and 1827 UT on November 9, 2002. The components of the shock normal vector were found to be $(-0.99, 0.15, -0.05)_{RH}$ and $(-0.98, -0.03, -0.20)_{RH}$ in the GSE coordinates using the Wind data and the Rankine-Hugoniot method. The shock fronts are illustrated in Figure 2 by the thick lines.

Figure 4 shows the solar wind plasma and interplanetary field observations from the Wind and Geotail spacecraft. The interplanetary magnetic field was Parker-spiral-like and B_z was dominant and positive both upstream and downstream of these events. The interplanetary shock θ_{Bn} angle was $\sim 43°$ for the first event and 70° for the second event, the compression ratios were 1.69 and 2.01.

In the magnetosphere, the disturbances were recorded as increases in the total magnetic field value. Figure 5 shows, for event timing purposes, the total magnetic field observed at GOES-10, GOES-8, Polar and Cluster-1. The density measurements were available only from Polar and Cluster-1. The event onsets at Geotail position (1747:50 UT and 1846:08 UT) are marked with vertical lines.

The GOES-8 and GOES-10 spacecraft recorded a clear magnetic field compression; plasma data are not available from these satellites. At Polar, the disturbance was mainly seen as a density compression, the magnetic field showed only a weak disturbance. Similarly, at Cluster-1 density compression was the dominating feature, while fluctuations in velocity, and ion flow deflection in the tailward direction were also recorded (not shown). Disturbance speeds were computed from the timings of the disturbance onsets at the various satellite positions; the results are summarized in Table 3. Uncertainties of the shocks speeds are about 10 km/s, while uncertainties of the disturbance speeds are about 50 km/s.

6. November 9, 2002: GUMICS-4 global MHD simulation results

6.1. Comparison with observations

The GUMICS-4 global MHD simulation was run using the solar wind observations during the November 9, 2002 shock events as an

Table 1. November 9, 2002 interplanetary shock event: Satellite locations in GSE coordinates at 1724 and 1827 UT.

Satellite	Event 1			Event 2		
	X [R_E]	Y [R_E]	Z [R_E]	X [R_E]	Y [R_E]	Z [R_E]
GOES-8	6.06	1.25	2.32	5.41	2.80	2.56
GOES-10	4.62	-4.72	0.06	5.57	-3.48	0.73
Polar	-5.90	6.00	1.70	-5.55	5.20	2.20
Cluster-1	-8.60	13.80	4.43	-8.62	14.34	3.93

Table 2. November 9, 2002 interplanetary shock event: Event onset times (UT) at different spacecraft locations (left) from observations and (right) from the GUMICS-4 global MHD simulation.

Satellite	Event 1		Event 2	
	Observed	GUMICS-4	Observed	GUMICS-4
GOES-8	1750:34	1753:00	1849:09	1850:30
GOES-10	1750:36	1753:00	1849:12	1850:00
Polar	1752:50	1756:00	1850:40	1853:30
Cluster-1	1753:20	1755:30	1852:10	1853:00

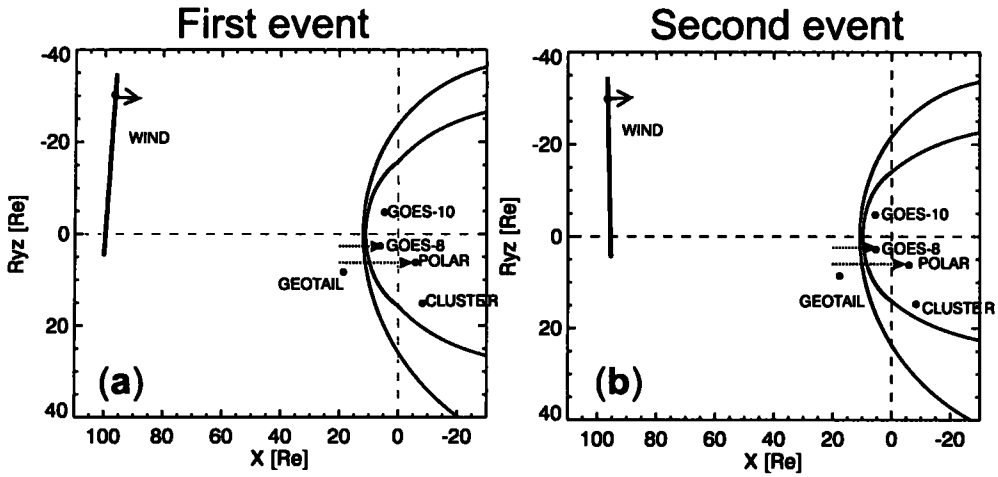

Figure 2. November 9, 2002 interplanetary shock event: (a) Positions of satellites for the event observed by Wind at 1724 UT. The thick line represents the interplanetary fast forward shock front. (b) Positions of given satellites for the second event observed by Wind at 1827 UT. The *Jeřáb et al.* [2005] and *Petrinec and Russell* [1996] models were used to determine the bow shock and magnetopause positions before the shock passages. R_{YZ} denotes the distance from the X axis, distinguishing the dawn/dusk sides (sign of Y), $R_{YZ} = sign(Y)\sqrt{Y^2 + Z^2}$. Dotted lines denote locations where the GUMICS-4 global simulation results are shown in Figure 3.

input. This allows us to examine the processes inside the magnetosphere and to trace the disturbance propagation within the simulation to much higher detail than it is possible observationally. While in the solar wind the shock fronts lasted for about 10 seconds, disturbance fronts in the dayside magnetosphere showed slower compression that lasted for about 5 minutes. In the simulation, the disturbance fronts lasted about 6 minutes.

The solar wind shock speeds from the data were computed to be about 380 km/s for the first case and about 425 km/s for the second one. The GUMICS-4 shock speeds were determined to be about 360 and 420 km/s. These values are in good agreement within the timing errors. The observations and simulation results showed consistent timings for the disturbance propagation at the various satellite positions. The satellite positions and the event onset times for both observations and simulation results are summarized in Tables 1 and 2. In the simulation, the disturbance onsets occurred with time delay of about 140 seconds for the first event and about 60 seconds for the second event with respect to the observed values.

The simulation results show that the magnetic field and plasma were both compressed in the dayside, at GOES-8 and GOES-10 locations. At the position of the Polar spacecraft, the simulation showed mainly a plasma density compression consistent with the observations. At the position of Cluster-1, in addition to the density compression, also a weak magnetic field compression was produced by the simulation. The propagation speeds deduced from the simulation results at the satellite locations are summarized in Table 3. While for the most part the results agree quite well, it is noticeable that the speeds in the simulation are somewhat lower than those observed in the magnetosphere. However, as timing uncertainties (in the magnetosphere) for the simulation are about 85 km/s, the differences are mostly within error bars. The simulation also confirmed our statistical result that the disturbance speeds are higher in the magnetosphere than in the solar wind, and that the nightside speeds are higher than those in the dayside.

The good agreement between the observed and simulation propagation speeds allows us to study effects of the shock/magnetopause interaction and propagation of the disturbances inside the magnetosphere and draw conclusions of the magnetospheric processes that the shock interaction causes.

We calculated gradients of plasma density and magnetic field from the simulation. Using these gradients (negative and positive for the plasma density and positive for the magnetic field) we detected positions of the magnetopause and bow shock in the dayside magnetosphere. As the FFS propagates almost perpendicular to the Sun-Earth line, the first contact point of the FFS with the bow shock and magnetopause is close to the nose of the magnetopause: The first FFS reached the magnetopause at 1750 UT, while the second FFS arrived at 1850 UT. The first contact point was also evaluated using observations and the *Petrinec and Russell* [1996] model to be at [11.4, -1.2, 0.6] R_E (in GSE coordinates) at 1749:29 UT for Event 1 and at [9.4, 0.3, -1.9] R_E at 1848:29 UT for Event 2. Figure 6 shows the positions of the bow shock and the magnetopause from the simulation and the inferred thickness of the magnetosheath as a function of time with the above derived contact points shown with solid dots. Magnetopause position was verified by the *Petrinec and Russell* [1996] model (dashed line) using the solar wind dynamic pressure and B_Z component of the magnetic field.

The bow shock reacts mainly to changes in the interplanetary magnetic field and dynamic pressure. On the other hand, the magnetopause interacts directly with the FFS, which during both events caused the magnetopause to move earthward with a speed of about 30 km/s. The magnetosphere was more compressed during Event 2, which is mainly caused by the higher dynamic pressure of the solar wind.

6.2. Disturbance propagation along Sun-Earth line

In order to illustrate the disturbance propagation within the magnetosphere, we traced its propagation in the simulation by placing "artificial satellites" along several straight lines parallel to the Sun-Earth line (see Figure 2). This gives a time series of the magnetic field and plasma parameters along lines that intersect with the satellite locations, and thus at the satellite positions simulation output can be directly compared with the observations. The artificial satellites were positioned within 1 R_E intervals along lines that intersect with GOES-8, GOES-10, Polar, and Cluster (for the Y and Z coordinates of the lines see Table 1).

Figure 3a shows results from the simulation along the line $Y = 5.5R_E, Z = 2.0R_E$ intersecting the GOES-8 position. The colored lines from dark red to green, blue, and dark purple show the time series at locations of increasing X-coordinate between 4 and 12 R_E. The Geotail observations from 18 R_E in the solar wind and the GOES-8 observations at 6 R_E are plotted with black dashed and dotted lines. The times of the estimated first contact with the magnetopause (1749 and 1848 UT) are marked with vertical lines. The relative disturbance onset times clearly show the propagation from the magnetopause toward the inner magnetosphere. At the beginning of Event 1, GOES-8 was located near 6 R_E, but during time it moved to 5.5 R_E. Prior to the events, the observations and the

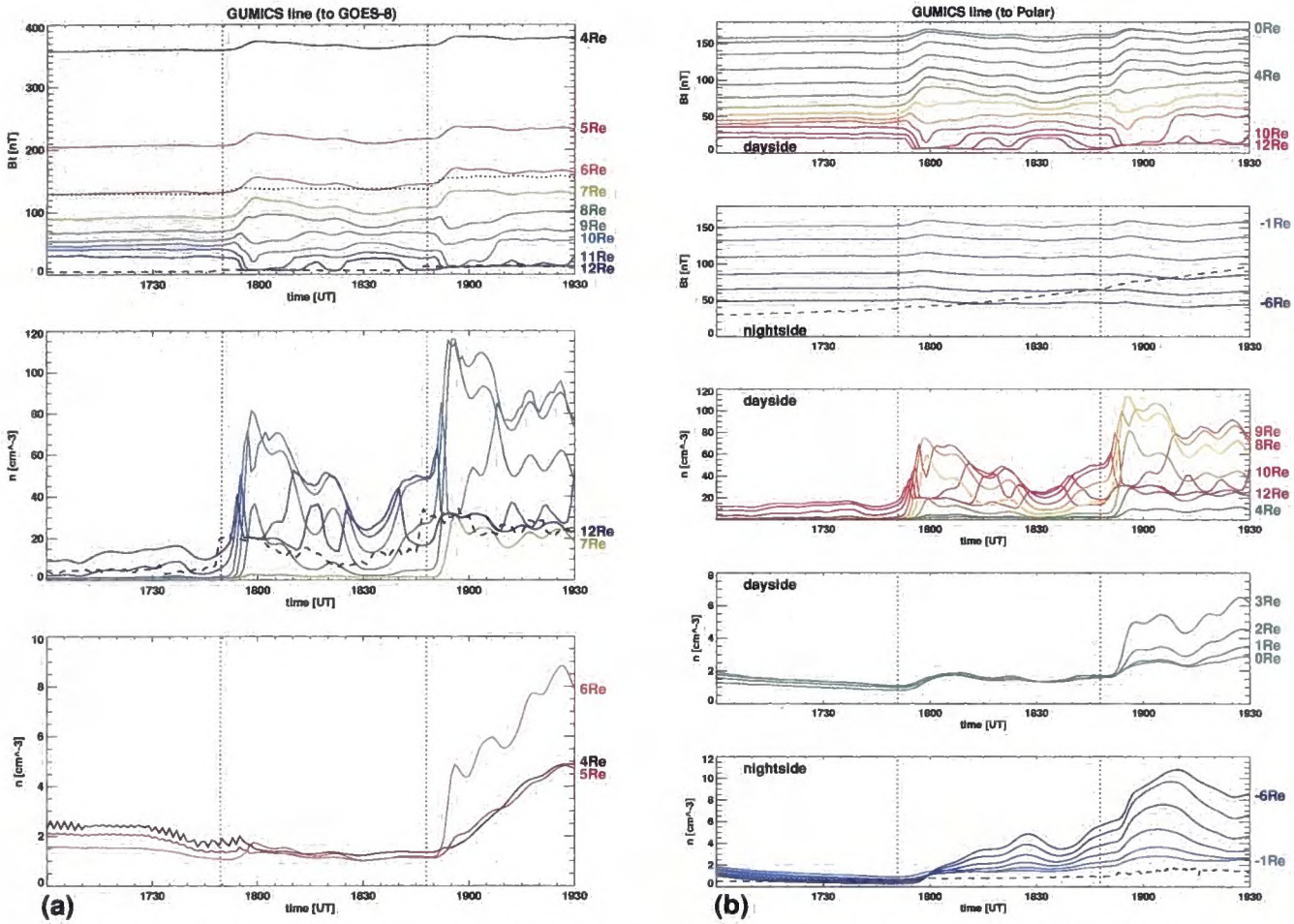

Figure 3. November 9, 2002 interplanetary shock event simulation: (a) Artificial satellite data from GUMICS simulation at 4–12 R_E, from magnetopause toward GOES-8 at $Y = 5.5R_E$ and $Z = 2.0R_E$. GUMICS data are shown with color solid lines, Geotail data by the dashed black line, and GOES-8 data by the black dotted line. Vertical red dashed lines mark the first observation of the disturbance passage at 12 R_E. The top panel shows the total magnetic field values, while the two bottom panels display the plasma density. For the density plot, we separated the magnetosheath (blue and green) and magnetosphere (red) to different panels with different scales. (b) Similar to (a), along the line toward Polar. The total magnetic field and density panels were divided into two and three parts showing the dayside (from red to green colors) and nightside (from light blue to dark magenta colors) values separately.

simulation agree very well. After the shock passages, the simulation showed higher magnetic field magnitudes than those observed by GOES-8.

Figure 3b shows data in a similar format, along the line parallel to the Sun-Earth line and intersecting with the Polar location. According to the simulation, Polar was located deep inside the nightside magnetosphere close to the plasma sheet near the plasma sheet boundary. Polar recorded only a weak magnetic field variation but quite significant density variation, which is consistent with the simulation results. The dayside field variations from X =12 to 0 R_E (top panel) show the field compression, but the nightside values from $X = -1$ to -6 R_E show only a weak magnetic disturbance (second panel). The density plots show that the density compression was significant both in the dayside (third and fourth panels) and in the nightside (bottom panel).

6.3. Disturbance propagation in a plane perpendicular to Sun-Earth line

The GUMICS-4 simulation allows us to trace the entire process of the changing magnetosphere as a response to the shock/disturbance passage. Figures 7–10 show the time evolution of magnitudes of magnetic field and plasma density 2D gradients during Event 1 (1752 and 1757 UT) and Event 2 (1849 and 1854 UT). The black and white lines mark the positions of the dayside bow shock and the magnetopause. The positions of GOES-8 (black and white cross) and Polar (black and white asterisk) are also pointed in the plots. The different panels show cuts in the YZ-plane at $X = \pm 5R_E$ and in the equatorial plane at $Z = 0$ (Figures 7 and 8) and at $Z = 2R_E$ (Figures 9 and 10).

The magnetic field differences in Figures 7 and 8 illustrate the strong compression of the magnetosphere during both events. According to the simulation, the bow shock moves from near 20 to near 13 R_E during the first event, and from near 15 to near 12 R_E during the second event. The magnetopause compression was not symmetric with respect to the Sun-Earth line; during both events the compression was stronger at low latitudes than in the polar regions.

Figures 9 and 10, illustrating the changes in density, show that the Polar satellite was immersed in the enhanced plasma flow during both events, thus completing the picture obtained from the string of artificial satellites. During the first event, Polar observed a slower increase of density, which can be interpreted as Polar being at the edge of the plasma flow. During the disturbance passages the plasma flow crossed over the satellite and was seen as an intensification of the flow speeds at that location. During Event 2, the plasma flow was stronger and closer to the Earth, which was caused by an already more compressed magnetosphere after the first shock – magnetopause interaction.

The normals of the interplanetary shocks were not parallel to the Sun-Earth line, which introduces an asymmetry to the disturbance

propagation across the magnetosphere, as demonstrated in Figure 11. The figure displays the disturbance propagation in the equatorial plane using time derivatives of the magnetic field. The compression of the magnetic field is somewhat stronger in the dayside magnetosphere adjacent to the interplanetary shock front. The disturbance wavefront is slightly faster on the opposite side of the magnetosphere (both dayside and nightside), where the wavefront normal is closer to the original shock propagation direction. The simulation also shows that the disturbance front is bifurcated around the Earth and in the tail, see Figure 11.

7. Discussion

The interplanetary shock fronts analyzed in this paper lasted about 30 s in the solar wind. However, in the Earth's magnetosphere the disturbance fronts lasted about 3—5 min, which is in good agreement with results by *Guo et al.* [2005]. Furthermore, we obtained consistent time delays during the propagation through the magnetosphere from the global MHD simulation GUMICS-4. In the dayside magnetosphere, we estimated time delay to be about 4 minutes, which is comparable to results shown by *Villante et al.* [2004].

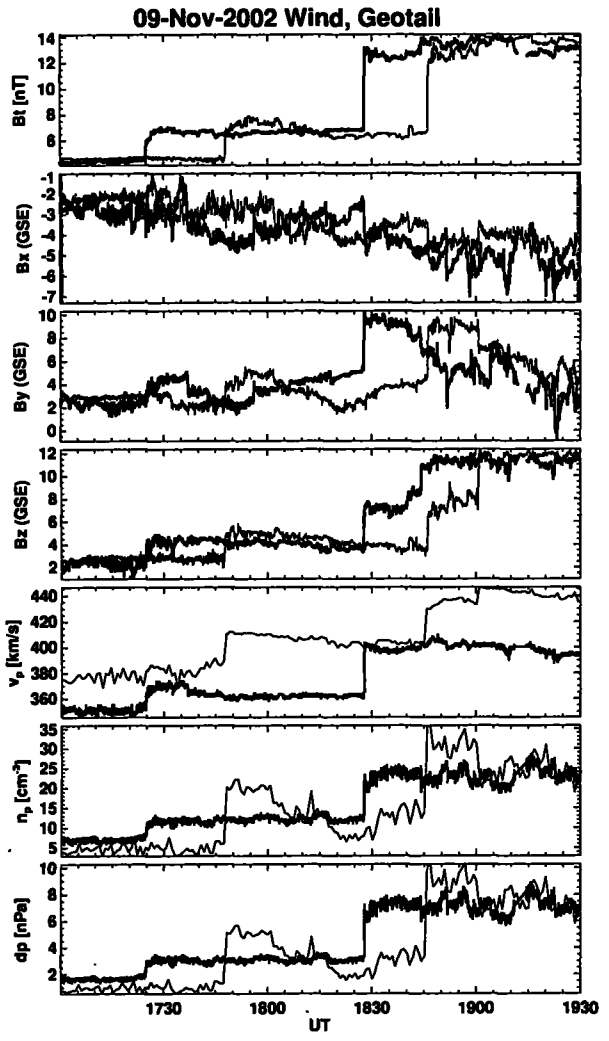

Figure 4. November 9, 2002 interplanetary shock event: Solar wind and IMF observations from Wind (thick line) and Geotail (thin line). Panels from top to bottom show the interplanetary total magnetic field Bt, components of magnetic field B_X, B_Y, and B_Z, solar wind velocity V_p, proton density n_p, and dynamic pressure dp. Wind instruments: MFI and 3DP, and Geotail instruments: MGF and CPI.

We calculated the disturbance speeds inside the magnetosphere for 42 events. The results show rather high scatter caused partly by the time resolution of the available data, partly by the spread of observation points across different magnetospheric regions, and differences in the magnetospheric state and time history. Despite this scatter, the results clearly demonstrate that the propagation speeds inside the magnetosphere are significantly higher than the shock speeds in the solar wind. Our results, 450–1500 km/s, agree with

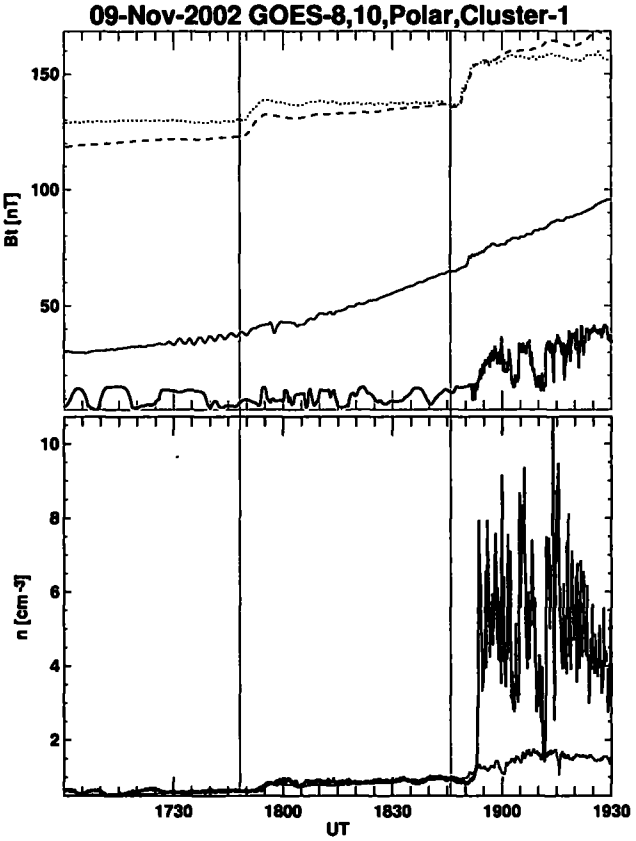

Figure 5. November 9, 2002 interplanetary shock event: Disturbance propagation in the magnetosphere. Panels from top to bottom show the total magnetic field at GOES-10 (dashed line), GOES-8 (dotted line), Polar (thin line), and Cluster-1 (thick line) and density from Polar and Cluster-1. The vertical lines mark the event onsets in solar wind at Geotail position (1747:50 UT and 1846:08 UT).

Table 3. November 9, 2002 interplanetary shock event: Propagation speeds in the solar wind and in the magnetosphere: v_{sw} is the solar wind speed, v_{sh} is the shock speed in the solar wind, v_{ms} is the disturbance speed in the magnetosphere, where D denotes dayside values, N nightside value and D-N means transterminator ("central") values. Speeds determined from observations are shown in the left columns, while those determined from the GUMICS-4 global MHD simulation are shown in the right columns for the two events separately.

Disturbance	Event 1		Event 2	
	Data	GUMICS-4	Data	GUMICS-4
v_{sw}	324	-	348	-
$v_{sh}(SW)$	380	360	425	420
Uncertainty	± 10	± 20	± 10	± 20
$v_{ms}(D)$	550	390	671	425
$v_{ms}(D-N)$	588	500	745	570
$v_{ms}(N)$	588	410	776	780
Uncertainty	± 50	± 85	± 50	± 85

estimates by *Wilken et al.* [1982] and *Nopper et al.* [1982] (about 600–1500 km/s). In the case study (November 9, 2002), we obtained speeds of about 600–700 km/s. These results were compared with the global MHD simulation GUMICS-4 that gave slightly smaller values, but confirmed the trend of the speeds to increase as the disturbance propagates tailward.

The main part of the paper concentrates on the analysis and simulation of a double fast forward shock event on November 9, 2002. The shocks were associated with solar wind dynamic pressure changes from 1.14 nPa to 5.19 nPa during the first shock and from 3.25 nPa to 9.25 nPa during the second shock, as estimated from Geotail measurements. Consequently, the subsolar magnetopause was located at about $R_o \sim 11.7R_E$ before the first shock, while during the second event the magnetopause was more compressed with the subsolar point initially at $R_o \sim 9.7R_E$. We have estimated the speed of the magnetopause earthward motion from the simulation to be about 30 km/s during both events.

Figure 11 demonstrates that the disturbance front does not stay planar in the magnetosphere. Similarly, recent global MHD simulations [*Ridley et al.*, 2006] have also shown a significant deformation of the interplanetary shock front in the magnetosphere. Furthermore, *Koval et al.* [2005, 2006] have shown the IP shock deceleration in the magnetosheath near the magnetopause, using both observations and numerical simulations.

8. Conclusions

We have studied the propagation of more than 40 fast forward shocks in the Earth's magnetosphere. We have assumed planar shocks and no change during their propagation in the solar wind. We calculated shock normals using different methods and the associated disturbance speeds in the Earth's magnetosphere using timing obtained from multispacecraft observations. We obtained speed values in the range 450–1500 km/s. The disturbance speeds in the magnetosphere were higher than the original shock speeds in the solar wind, and the propagation speeds gradually increase tailward from the nose of the magnetopause. Furthermore, comparison of the observed propagation speeds with the upstream solar wind dynamic pressure shows that the propagation speeds are higher for higher dynamic pressures (smaller initial size of the magnetosphere).

The observations were compared with the GUMICS-4 global MHD simulation results of a double fast forward shock event on November 9, 2002. Using the simulation we can follow the 3D propagation of the shock front in the different regions of the magnetosphere. The simulation results were analyzed to trace the disturbance propagation both in the direction parallel to the Sun-Earth line as well as through a perpendicular cross-section of the magnetosphere. The cross-sectional plots show that the changes were largest within the high-latitude magnetosheath and within the plasma sheet and the front of the disturbance is significantly deformed both in the dayside and nightside magnetosphere. The simulation results in our case study are consistent with our statistical results: The disturbance speeds in the Earth's magnetosphere were higher for the second shock during which the dynamic pressure was higher.

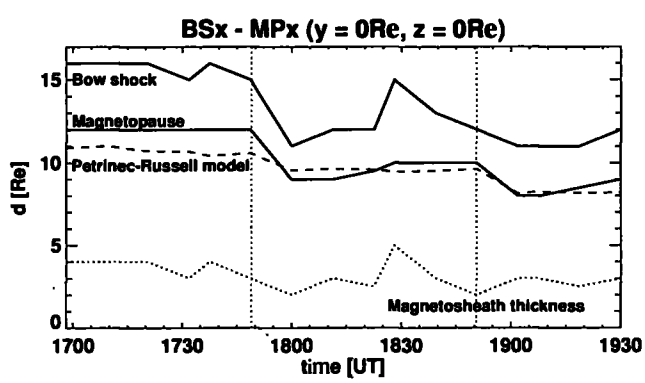

Figure 6. Simulation of November 9, 2002 interplanetary shock event: Magnetopause and bow shock distance from the Earth in R_E. The dotted line shows the magnetosheath thickness along the Sun-Earth line. The dashed line shows the magnetopause position derived from the Petrinec and Russell model of the magnetopause.

9. Acknowledgement

This work was supported by the Research Plan MSM 0021620860, partly by the Charles University Grant Agency under Contract 147307, and by the Czech Grant Agency under Contract 205/06/0875. The work of Tiera Laitinen was supported by the Academy of Finland. We thank J.C. Kasper (MIT) for providing the data and support to his interplanetary shock database, and the CDAWeb service and the corresponding PIs for the satellite data.

References

Andreeova, K., and L. Prech (2007), Propagation of interplanetary shocks into the Earth's magnetosphere, *Adv. Space Res.*, *40*, 1871–1880, doi:10.1016/j.asr.2007.04.079.

Balogh, A., M. W. Dunlop, S. W. H. Cowley, D. J. Southwood, J. G. Thomlinson, K. H. Glassmeier, G. Musmann, H. Luhr, S. Buchert, M. H. Acuna, D. H. Fairfield, J. A. Slavin, W. Riedler, K. Schwingenschuh, and M. G. Kivelson (1997), The Cluster Magnetic Field Investigation, *Space Sci. Rev.*, *79*, 65–91.

Berdichevsky, D. B., A. Szabo, R. P. Lepping, A. F. Vinas, and F. Mariani (2000), Interplanetary fast shocks and associated drivers observed through the 23rd solar minimum by Wind over its first 2.5 years, *J. Geophys. Res.*, *105*, 27,289–27,314.

Burlaga, L. F. (1971), Hydromagnetic waves and discontinuities in the solar wind, *Space Sci. Rev.*, *12*, 600–657.

Grib, S. A. (1982), Interaction of non-perpendicular/parallel solar wind shock waves with the Earth's magnetosphere, *Space Sci. Rev.*, *32*, 43–48.

Grib, S. A., B. E. Briunelli, M. Dryer, and W.-W. Shen (1979), Interaction of interplanetary shock waves with the bow shock-magnetopause system, *J. Geophys. Res.*, *84*, 5907–5921.

Guo, X.-C., Y.-Q. Hu, and C. Wang (2005), Earth's magnetosphere impinged by interplanetary shocks of different orientations, *Chin. Phys. Lett.*, *22*, 3221–3224.

Harvey, P., F. S. Mozer, D. Pankow, J. Wygant, N. C. Maynard, H. Singer, W. Sullivan, P. B. Anderson, R. Pfaff, T. Aggson, A. Pedersen, C.-G. Fälthammar, and P. Tanskannen (1995), The Electric Field Instrument on the Polar Satellite, *Space Sci. Rev.*, *71*, 583–596.

Janhunen, P. (1996), GUMICS-3 A Global Ionosphere-Magnetosphere Coupling Simulation with High Ionospheric Resolution, in *Environment Modeling for Space-Based Applications, ESA Special Publication*, vol. 392, edited by T.-D. Guyenne and A. Hilgers, pp. 233–+.

Jeřáb, M., Z. Němeček, J. Šafránková, K. Jelínek, and J. Měrka (2005), A study of bow shock locations, *Planet. Space Sci.*, *53*, 85–94.

Kokubun, S., T. Yamamoto, M. H. Acuna, K. Hayashi, K. Shiokawa, and H. Kawano (1994), The Geotail Magnetic Field Experiment, *J. Geomag. Geoelectr.*, *46*, 7–21.

Koval, A., J. Šafránková, Z. Němeček, L. Přech, A. A. Samsonov, and J. D. Richardson (2005), Deformation of interplanetary shock fronts in the magnetosheath, *Geophys. Res. Let.*, *32*, L15101, doi:10.1029/2005GL023009.

Koval, A., J. Šafránková, Z. Němeček, A. A. Samsonov, L. Přech, J. D. Richardson, and M. Hayosh (2006), Interplanetary shock in the magnetosheath: Comparison of experimental data with MHD modeling, *Geophys. Res. Let.*, *33*, L11102, doi:10.1029/2006GL025707.

Le, G., and C. T. Russell (1998), Initial polar magnetic field experiment observations of the low-altitude polar magnetosphere: Monitoring the ring current with polar orbiting spacecraft, *J. Geophys. Res.*, *103*, 17,345–17,350.

Le, G., C. T. Russell, and J. G. Luhmann (1998), POLAR magnetic observations of the low-altitude magnetosphere during the January 1997 coronal mass ejection/magnetic cloud event, *Geophys. Res. Let.*, *25*, 2533–2536.

Lepping, R. P., M. H. Acūna, L. F. Burlaga, W. M. Farrell, J. A. Slavin, K. H. Schatten, F. Mariani, N. F. Ness, F. M. Neubauer, Y. C. Whang, J. B. Byrnes, R. S. Kennon, P. V. Panetta, J. Scheifele, and E. M. Worley (1995), The Wind Magnetic Field Investigation, *Space Sci. Rev.*, *71*, 207–229.

Lin, R. P., K. A. Anderson, S. Ashford, C. Carlson, D. Curtis, R. Ergun, D. Larson, J. McFadden, M. McCarthy, G. K. Parks, H. Rème, J. M. Bosqued, J. Coutelier, F. Cotin, C. D'Uston, K.-P. Wenzel, T. R. Sanderson, J. Henrion, J. C. Ronnet, and G. Paschmann (1995), A Three-Dimensional Plasma and Energetic Particle Investigation for the Wind Spacecraft, *Space Sci. Rev.*, *71*, 125–153.

McComas, D. J., S. J. Bame, P. Barker, W. C. Feldman, J. L. Phillips, P. Riley, and J. W. Griffee (1998), Solar Wind Electron Proton Alpha Monitor (SWEPAM) for the Advanced Composition Explorer, *Space Sci. Rev.*, *86*, 563–612.

Mukai, T., S. Machida, Y. Saito, M. Hirahara, T. Terasawa, N. Kaya, T. Obara, M. Ejiri, and N. A. (1994), The low energy particle (LEP) experiment onboard the Geotail satellite, *J. Geomagn. Geoelectr.*, *46*, 669–692.

Nopper, R. W., Jr., W. J. Hughes, C. G. Maclennan, and R. L. McPherron (1982), Impulse-excited pulsations during the July 29, 1977, event, *J. Geophys. Res.*, *87*, 5911–5916.

Ogilvie, K. W., D. J. Chornay, R. J. Fritzenreiter, F. Hunsaker, J. Keller, J. Lobell, G. Miller, J. D. Scudder, E. C. Sittler, Jr., R. B. Torbert, D. Bodet, G. Needell, A. J. Lazarus, J. T. Steinberg, J. H. Tappan, A. Mavretic, and E. Gergin (1995), SWE, A Comprehensive Plasma Instrument for the Wind Spacecraft, *Space Sci. Rev*, *71*, 55–77.

Petrinec, S. M., and C. T. Russell (1996), Near-Earth magnetopause shape and size as determined from the magnetopase flaring angle, *J. Geophys. Res.*, *101*, 137–152.

Prech, L., J. Safrankova, and Z. Nemecek (2008), Response of magnetospheric boundaries to the interplanetary shock: Themis contribution, *Geophys. Res. Lett.*, *35*, L17S02, doi:10.1029/2008GL033593.

Reme, H., J. M. Bosqued, J. A. Sauvaud, A. Cros, J. Dandouras, C. Aoustin, J. Bouyssou, T. Camus, J. Cuvilo, C. Martz, J. L. Medale, H. Perrier, D. Romefort, J. Rouzaud, C. D'Uston, E. Mobius, K. Crocker, M. Granoff, L. M. Kistler, M. Popecki, D. Hovestadt, B. Klecker, G. Paschmann, M. Scholer, C. W. Carlson, D. W. Curtis, R. P. Lin, J. P. McFadden, V. Formisano, E. Amata, M. B. Bavassano-Cattaneo, P. Baldetti, G. Belluci, R. Bruno, G. Chionchio, A. di Lellis, E. G. Shelley, A. G. Ghielmetti, W. Lennartsson, A. Korth, H. Rosenbauer, R. Lundin, S. Olsen, G. K. Parks, M. McCarthy, and H. Balsiger (1997), The Cluster Ion Spectrometry (cis) Experiment, *Space Sci. Rev.*, *79*, 303–350.

Ridley, A. J., D. L. De Zeeuw, W. B. Manchester, and K. C. Hansen (2006), The magnetospheric and ionospheric response to a very strong interplanetary shock and coronal mass ejection, *Adv. Space Res.*, *38*, 263–272.

Russell, C. T., R. C. Snare, J. D. Means, D. Pierce, D. Dearborn, M. Larson, G. Barr, and G. Le (1995), The GGS/POLAR magnetic fields investigation, *Space Sci. Rev.*, *71*, 563–582.

Šafránková, J., Z. Němeček, L. Přech, A. A. Samsonov, A. Koval, and K. Andréeová (2007), Modification of interplanetary shocks near the bow shock and through the magnetosheath, *J. Geophys. Res.*, *112*, A08212, doi:10.1029/2007JA012503.

Samsonov, A. A., Z. Němeček, and Šafránková (2006), Numerical MHD modeling of propagation of interplanetary shock through the magnetosheath, *J. Geophys. Res.*, *111*, A08210, doi:10.1029/2005JA011537.

Samsonov, A. A., D. G. Sibeck, and J. Imber (2007), MHD simulation for the interaction of an interplanetary shock with the Earth's magnetosphere, *J. Geophys. Res.*, *112*, A12220, doi:10.1029/2007JA012627.

Singer, H. J., L. Matheson, R. Grubb, A. Newman, and S. D. Bouwer (1996), Monitoring space weather with the GEOS magnetometers, *SPIE conference proceedings, GEOS-8 and Beyond*, *2812*, 299–308.

Smith, C. W., J. L'Heureux, N. F. Ness, M. H. Acuña, L. F. Burlaga, and J. Scheifele (1998), The ACE Magnetic Fields Experiment, *Space Sci. Rev.*, *86*, 613–632.

Spreiter, J. R., and S. S. Stahara (1994), Gasdynamic and magnetohydrodynamic modeling of the magnetosheath: A tutorial, *Adv. Space Res.*, *14*, 5–19.

Szabo, A. (1994), An improved solution to the 'Rankine-Hugoniot' problem, *J. Geophys. Res.*, *99*, 14,737.

Szabo, A., R. P. Lepping, J. Merka, C. W. Smith, and R. M. Skoug (2001), The evolution of interplanetary shocks driven by magnetic clouds, in *Solar encounter Proceedings of the First Solar Orbiter Workshop*, edited by B. Battrick, H. Sawaya-Lacoste, E. Marsch, V. Martinez Pillet, B. Fleck, and R. Marsden, ESA SP-493, pp. 383–387.

Tamao, T. (1964), The structure of three-dimensional hydromagnetic waves in a uniform cold plasma, *J. Geomagn. Geoelectr.*, *18*, 89–114.

Villante, U., S. Lepidi, P. Francia, and T. Bruno (2004), Some aspects of the interaction of interplanetary shocks with the Earth's magnetosphere: an estimate of the propagation time through the magnetosheath, *J. Atm. Solar-Terr Phys.*, *66*, 337–341.

Wilken, B., C. K. Goertz, D. N. Baker, P. R. Higbie, and T. A. Fritz (1982), The SSC on July 29, 1977 and its propagation within the magnetosphere, *J. Geophys. Res.*, *87*, 5901–5910.

Zhuang, H. C., C. T. Russell, E. J. Smith, and J. T. Gosling (1981), Three-dimensional interaction of interplanetary shock waves with the bow shock and magnetopause - A comparison of theory with ISEE observations, *J. Geophys. Res.*, *86*, 5590–5600.

K. Andreeova, L. Prech, Charles University Prague, V Holesovickach 2, CZ-18000 Prague 8, Czech Republic. email: andreeova@seznam.cz

T. I. Pulkkinen, Finnish Meteorological Institute, POBox 503, FIN-00101 Helsinki, 358919294654, Finland. e-mail tuija.pulkkinen@fmi.fi

T. Laitinen, Swedish Institute for Space Physics, Box 537, SE-75121 Uppsala, +46-18-4715944, Sweden. e-mail tiera.laitinen@irfu.se

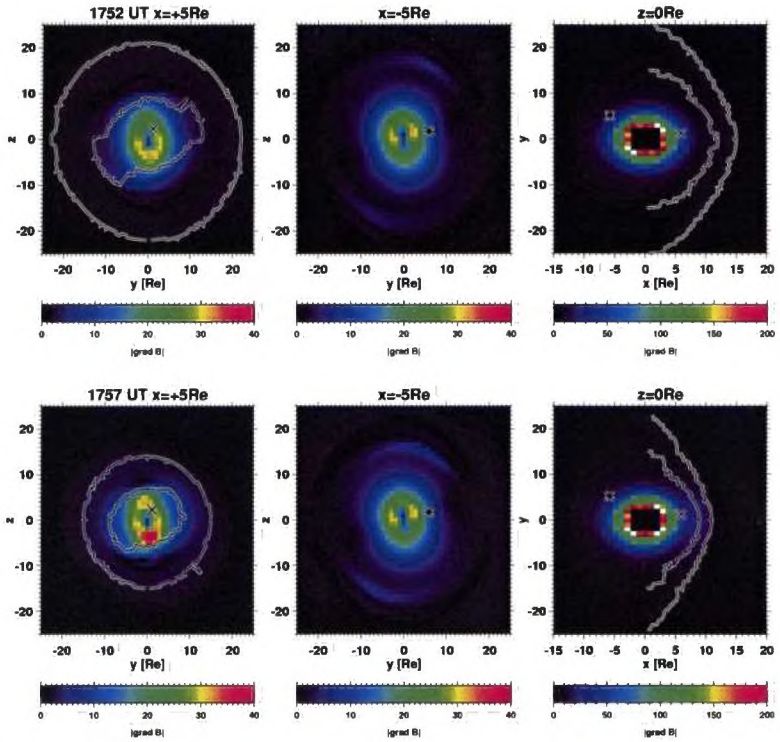

Figure 7. November 9, 2002 interplanetary shock Event 1 simulation: A cross-section of the magnetosphere in the YZ-plane at $X = 5R_E$ (left), $X = -5R_E$ (middle), and in the equatorial plane (right) at $Z = 0R_E$ at 1752 UT (top row) and 1757 UT (bottom row). The color coding shows magnitudes of the magnetic field gradient in nT/R_E in the given plane. The black and white lines in the left and right panels show the positions of the bow shock and the magnetopause. The position of GOES-8 and Polar are shown with the black and white cross and asterisk, respectively.

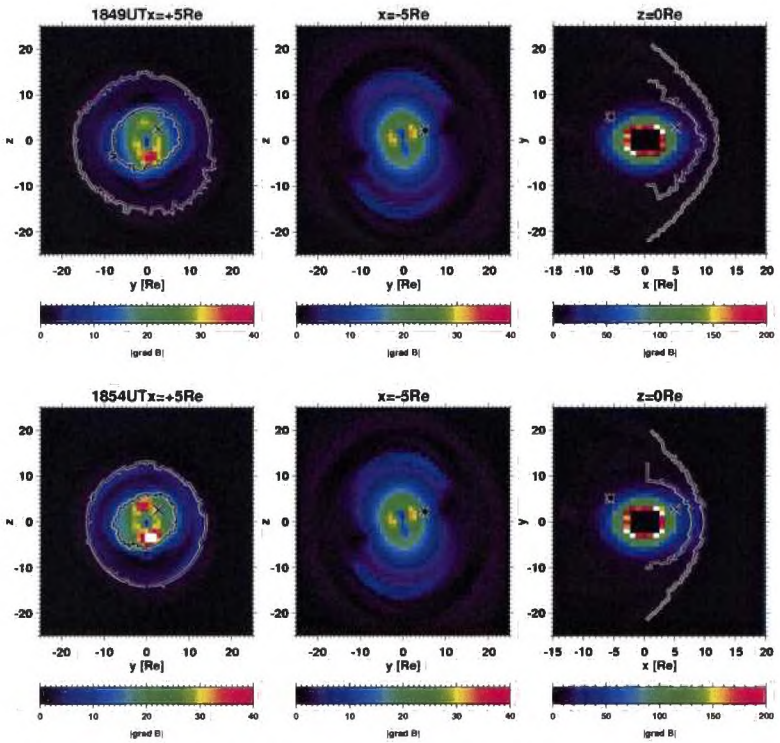

Figure 8. November 9, 2002 interplanetary shock Event 2 simulation: magnitudes of the magnetic field gradient in nT/R_E in a format similar to Figure 7 at 1849 UT (top row) and 1854 UT (bottom row).

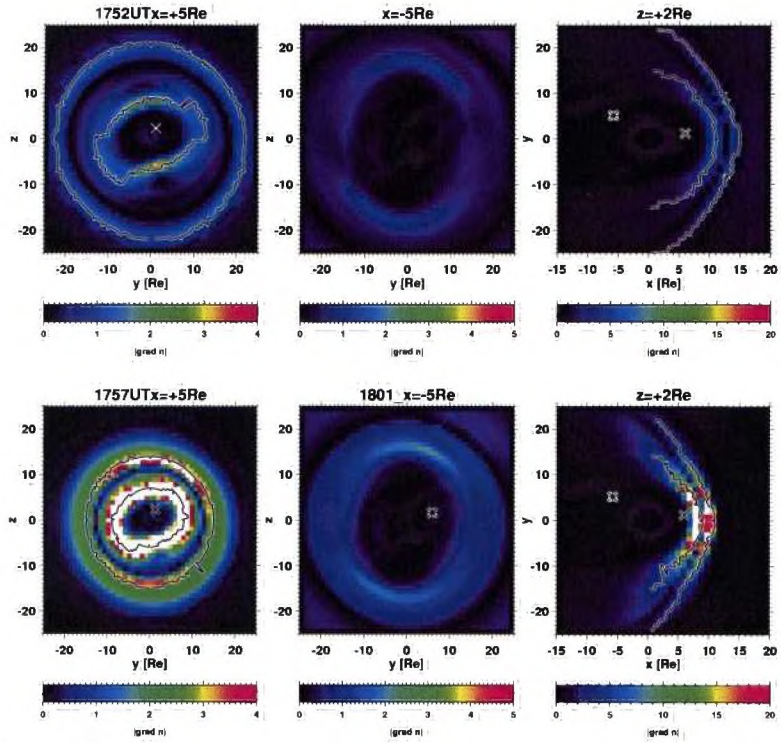

Figure 9. November 9, 2002 interplanetary shock Event 1 simulation: A cross-section of the magnetosphere in the YZ-plane at $X = 5R_E$ (left), $X = -5R_E$ (middle), and in the equatorial plane (right) at $Z = +2R_E$ at 1752 UT (top row) and 1757 UT (bottom row). The color coding shows magnitudes of the plasma density gradient in cm^{-3}/R_E in the given plane. The black and white lines in the left and right panels show the positions of the bow shock and the magnetopause. The position of GOES-8 and Polar are shown with the black and white cross and asterisk, respectively.

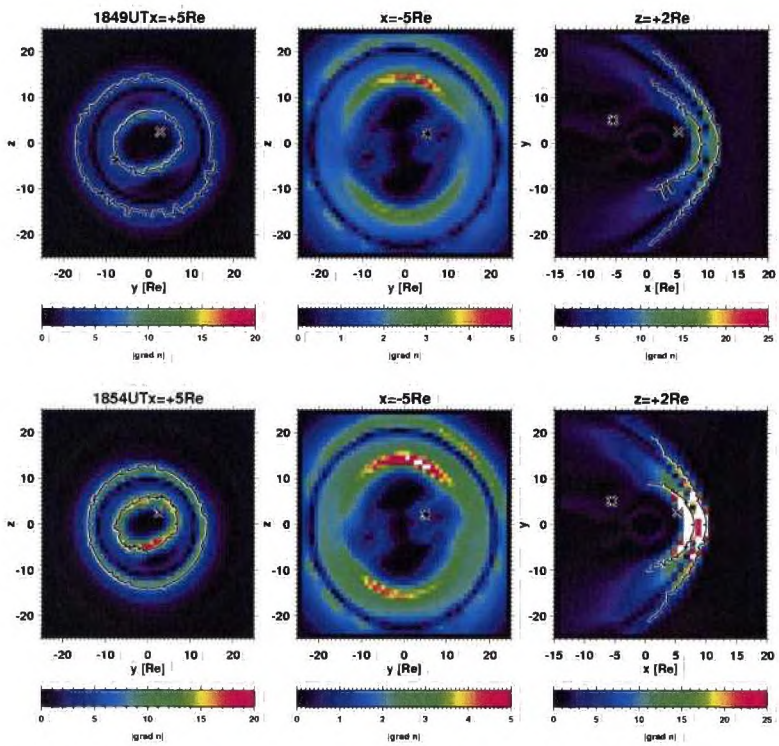

Figure 10. November 9, 2002 interplanetary shock Event 2 simulation: magnitudes of the plasma density gradient in cm^{-3}/R_E in a format similar to Figure 9 at 1849 UT (top row)and 1854 UT(bottom row).

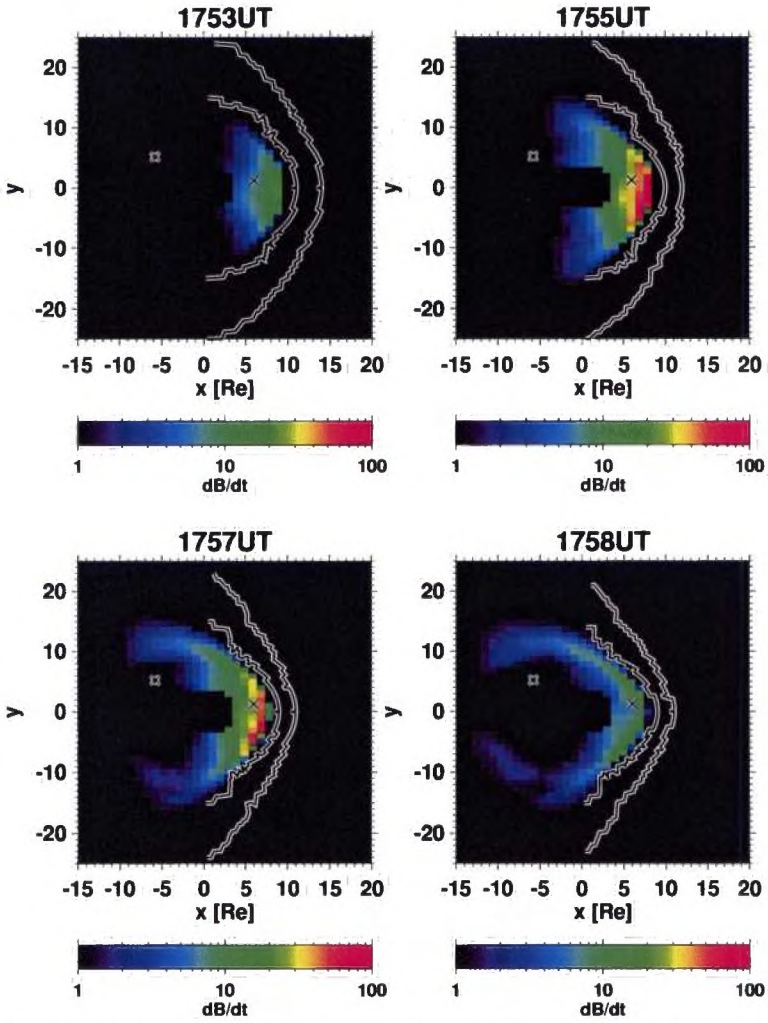

Figure 11. November 9, 2002 interplanetary shock Event 1: the disturbance propagation in the equatorial plane using time derivatives of magnetic field (nT/min) in four time snaps: 1753, 1755, 1757, and 1758 UT.